

CMS Draft Analysis Note

The content of this note is intended for CMS internal use and distribution only

2015/04/07

Head Id: 217659

Archive Id: 283571:283594

Archive Date: 2013/11/22

Archive Tag: trunk

Measurement of double differential Drell-Yan and associated jet cross sections at low and high invariant masses in proton-proton collisions at $\sqrt{s} = 7$ TeV

The CMS Collaboration

Abstract

Measurements of the differential Drell-Yan and associated jet cross section as a function of the Drell-Yan mass are presented in the di-muon channel. The data set is based on an integrated luminosity of 4.9 fb^{-1} of proton-proton collision data recorded with the CMS detector at the LHC at $\sqrt{s} = 7$ TeV. Cross sections as a function of the Drell-Yan transverse momentum are measured differentially in the Drell-Yan mass range of 30 to 1500 GeV. The cross section for Drell-Yan production in association with one or two jets with $p_T^{\text{jet}} > 30$ GeV in the range $|\eta^{\text{jet}}| < 4.5$ is measured. In addition, the jet multiplicity in Drell-Yan production as a function of the rapidity separation of the leading jet and the Drell-Yan is presented. All measurements are compared to predictions of Monte Carlo event generators based on multiparton matrix elements plus parton showers.

This box is only visible in draft mode. Please make sure the values below make sense.

PDFAuthor: S. Dooling, H. Jung
PDFTitle: Measurement of the double differential Drell-Yan cross section at low and high masses of the dimuon system at $s = 7\text{TeV}$
PDFSubject: CMS
PDFKeywords: CMS, Drell-Yan, Jets

Please also verify that the abstract does not use any user defined symbols

1 Introduction

- The production of Drell-Yan (DY) lepton pairs in hadron-hadron collisions is described as an **s-channel** γ^*/Z exchange at leading order (LO). Theoretical calculations for inclusive DY lepton pair production as a function of the DY lepton pair mass and transverse momentum p_T are available up to next-to-next-to-leading order (NNLO) in perturbative quantum chromodynamics (pQCD) [1–4]. While DY lepton pair production at large transverse momenta p_T can be described with fixed leading or next-to-leading order calculations in pQCD, the description at small transverse momenta requires resummation of soft gluons to all orders in perturbation theory [5, 6]. The p_T distribution of DY lepton pairs has been measured at LHC energies in the Z mass range [7], but the corresponding measurements as a function of the DY lepton pair mass m_{DY} are not available.
- Of special interest is the p_T spectrum of the DY lepton pair and the contribution from non-perturbative and perturbative multi-gluon resummation. In inclusive DY lepton pair production, the resummation effects are concentrated at small p_T with the maximum of the p_T distribution being around 5 GeV, not depending much on the DY lepton pair mass. If however a jet with large p_T is required in addition, the p_T spectrum of DY lepton pair is shifted towards larger transverse momenta, thus allowing to study multiple-gluon emission and resummation effects in the perturbative region and to separate them from the non-perturbative contribution at small p_T .
- Multi-jet emissions in a pseudorapidity interval between the DY lepton pair and a leading jet are a sensitive probe for multi-gluon emissions [8]. At large rapidity separation between the DY lepton pair and the jet, a fixed order approach is expected to fail, and again perturbative multi-jet resummation might play a significant role. Of additional interest is the jet multiplicity between the DY lepton pair and the leading jet, as resummation might lead to a different behavior compared to a fixed order prediction. The detailed measurements of inclusive DY lepton pair production as well as DY lepton pair production in association with jets, especially in the mass range above the Z mass (and in the range of $m_{\text{DY}} \sim 125$ GeV), is important for a later comparison with Higgs production, which can be used to determine the differences of soft gluon and multi-jet resummation in a quark or gluon induced process [9].
- In this paper we present a measurement of the differential Drell-Yan and associated jet cross section for various ranges of Drell-Yan mass m_{DY} using an integrated luminosity of 4.9 fb^{-1} in the di-muon channel of proton-proton collision data recorded with the CMS detector at the LHC at $\sqrt{s} = 7$ TeV. Differential cross sections as a function of the Drell-Yan transverse momentum are measured differentially in the Drell-Yan mass range of $30 < m_{\text{DY}} < 1500$ GeV. The cross sections for Drell-Yan production in association with at least one or two jets (in the following DY + 1 jet and DY + 2 jets, respectively) with $p_T^{\text{jet}} > 30$ GeV in the range $|\eta^{\text{jet}}| < 4.5$ are measured, where $\eta = -\ln[\tan(\theta/2)]$ and θ is the polar angle with respect to the anti-clockwise beam direction. Jets are reconstructed by the anti- k_T algorithm [10–12] with a radius parameter of 0.5. In addition the jet multiplicity in Drell-Yan production as a function of the separation in rapidity between the leading jet and the Drell-Yan is presented.

2 The CMS Detector

- The central feature of the Compact Muon Solenoid (CMS) apparatus is a superconducting solenoid of 6 m internal diameter, providing a magnetic field of 3.8 T. Within the superconducting solenoid volume are a silicon pixel and strip tracker, a lead tungstate crystal electromagnetic calorimeter (ECAL), and a brass/scintillator hadron calorimeter (HCAL). Muons are

⁴⁶ measured in gas-ionization detectors embedded in the steel return yoke outside the solenoid.
⁴⁷ Extensive forward calorimetry complements the coverage provided by the barrel and endcap
⁴⁸ detectors.

⁴⁹ CMS uses a right-handed coordinate system, with the origin at the nominal interaction point,
⁵⁰ the x axis pointing to the centre of the LHC, the y axis pointing up (perpendicular to the LHC
⁵¹ plane), and the z axis along the anticlockwise-beam direction. The polar angle θ is measured
⁵² from the positive z axis and the azimuthal angle ϕ is measured in the x - y plane.

⁵³ The particle-flow event reconstruction consists in reconstructing and identifying each single
⁵⁴ particle with an optimised combination of all subdetector information. The energy of pho-
⁵⁵ tons is directly obtained from the ECAL measurement, corrected for zero-suppression effects.
⁵⁶ The energy of electrons is determined from a combination of the track momentum at the
⁵⁷ main interaction vertex, the corresponding ECAL cluster energy, and the energy sum of all
⁵⁸ bremsstrahlung photons attached to the track. The energy of muons is obtained from the cor-
⁵⁹ responding track momentum. Muons are measured in the pseudorapidity range $|\eta| < 2.4$,
⁶⁰ with detection planes made using three technologies: drift tubes, cathode strip chambers, and
⁶¹ resistive plate chambers. Matching muons to tracks measured in the silicon tracker results in
⁶² a relative transverse momentum resolution for muons with $20 < p_T < 100$ GeV of 1.3–2.0% in
⁶³ the barrel and better than 6% in the endcaps. The p_T resolution in the barrel is better than 10%
⁶⁴ for muons with p_T up to 1 TeV [13]. The energy of charged hadrons is determined from a com-
⁶⁵ bination of the track momentum and the corresponding ECAL and HCAL energy, corrected for
⁶⁶ zero-suppression effects, and calibrated for the nonlinear response of the calorimeters. Finally
⁶⁷ the energy of neutral hadrons is obtained from the corresponding calibrated ECAL and HCAL
⁶⁸ energy.

⁶⁹ For each event, hadronic jets are clustered from these reconstructed particles with the infrared-
⁷⁰ and collinear safe anti- k_T algorithm, operated with a size parameter R of 0.5. The jet momen-
⁷¹ tum is determined as the vectorial sum of all particle momenta in this jet, and is found in the
⁷² simulation to be within 5% to 10% of the true momentum over the whole p_T spectrum and de-
⁷³ tector acceptance. An offset correction is applied to take into account the extra energy clustered
⁷⁴ in jets due to additional proton-proton interactions within the same bunch crossing. Jet energy
⁷⁵ corrections are derived from the simulation, and are confirmed with in situ measurements with
⁷⁶ the energy balance of dijet and photon+jet events [14]. Additional selection criteria are applied
⁷⁷ to each event to remove spurious jet-like features originating from isolated noise patterns in
⁷⁸ certain HCAL regions. The jet energy resolution amounts typically to 15% at 10 GeV and 8%
⁷⁹ at 100 GeV to be compared to about 40% and 12%, obtained when the calorimeters alone are
⁸⁰ used for jet clustering.

⁸¹ A more detailed description can be found in Ref. [15].

⁸² 3 Data and Monte Carlo Samples

⁸³ The measurements presented in this paper are based on pp collision data recorded in 2011 with
⁸⁴ the CMS detector at the LHC at $\sqrt{s} = 7$ TeV, corresponding to an integrated luminosity of
⁸⁵ 4.9 fb^{-1} .

⁸⁶ The datasets of interest (AODs) are listed in tab. 1. The corresponding JSON files are taken into
⁸⁷ account in order to obtain good quality data.

⁸⁸ The determination of background events from processes that result in two muons as well as
⁸⁹ the determination of systematic uncertainties is performed using MC event samples. The MC

Table 1: Primary data stream according to the trigger selection SingleMu and DoubleMu and the respective luminosities.

| dataset | integrated luminosity [fb^{-1}] |
|-------------------------|-----------------------------------------------|
| Run_2011A_May10thRR | 0.216 |
| Run_2011A_PR_v4 | 0.955 |
| Run_2011A_RR_2012-01-16 | 1.135 |
| Run_2011B_RR_2012-01-16 | 2.587 |
| total | 4.893 |

samples are produced by the MADGRAPH [16] (version 5) and PYTHIA [17] (version 6.4.33) event generators. These samples are passed through the full CMS detector simulation based on GEANT4 [18], which includes trigger simulations, full chain of the CMS event reconstruction, and pileup simulation.

94

The signal and background samples used for MC simulation are listed in Table 2. To compare the observed data with the simulation of the experiment, the simulated events are normalised to obtain the same distribution of the mean number of collisions per bunch crossing. For this reason a normalisation factor is assigned to the MC events according to the number of expected events in data

$$\omega_{\text{norm}} = \frac{\sigma \mathcal{L}}{N_{\text{processed}}}, \quad (1)$$

where σ is the cross section of each process as listed in Table 2, taken from Ref. [19], \mathcal{L} is the integrated data luminosity, and $N_{\text{processed}}$ is the number of generated MC events.

The DY signal samples are generated by MADGRAPH and are split into a sample of dileptons with invariant mass $10 < m_{\text{DY}} < 50$ GeV and another with $m_{\text{DY}} > 50$ GeV. Electroweak production of the Drell-Yan lepton pair is not included in the MADGRAPH MC predictions.

105

Different background processes contribute to the final state of two leptons and jets and can be misidentified as signal events. The precise modelling of the background processes is necessary in order not to bias the signal. The contributions from $Z \rightarrow \tau\tau$, $t\bar{t}$ and $W+\text{jets}$ production are generated by MADGRAPH. All samples are interfaced with PYTHIA6 to simulate the parton shower, hadronisation and UE. In all cases the tune Z2 is used. The background contributions from dibosons (WW , WZ , ZZ) and QCD multi-jets are produced with PYTHIA6 Z2.

4 Event Selection

The DY process in the muon channel provides a characteristic signature of two isolated muons with opposite charge. The identification and isolation of the muons was explained in section 4.3. The muons must correspond to the same primary vertex (section 4.1) to ensure they are from the same collision. The measurement is performed for a pair of muons with $p_{\text{T}}^{\text{lead}\mu} > 20$ GeV and $p_{\text{T}}^{\text{sublead}\mu} > 10$ GeV. The p_{T} criteria are well above the trigger thresholds to minimise the bias from the trigger efficiency. The muons are selected within $|\eta^\mu| < 2.1$, which corresponds to the fiducial region of the trigger acceptance to optimise the trigger efficiency.

Table 2: Signal and Background MC samples.

| Process | Generator | σ [pb] | Number of generated events |
|-----------------------------|-----------|---------------|----------------------------|
| Z+jets ($m_{ll} > 50$ GeV) | MADGRAPH | 3048 | 36,179,628 |
| Z+jets ($m_{ll} < 50$ GeV) | MADGRAPH | 9530 | 31,480,628 |
| $Z \rightarrow \tau\tau$ | MADGRAPH | 3048 | 36,179,628 |
| $t\bar{t}$ | MADGRAPH | 165 | 17,889,708 |
| W+jets | MADGRAPH | 31314 | 81,345,384 |
| QCD ($p_{T,\mu} > 15$ GeV) | PYTHIA6 | 84679 | 25,080,240 |
| WW | PYTHIA6 | 43 | 4,225,916 |
| WZ | PYTHIA6 | 18.2 | 4,265,243 |
| ZZ | PYTHIA6 | 5.9 | 4,191,045 |

120 The dimuon system is based on the two selected muons by choosing the two leading muons.
 121 The dimuon variables are defined as the vectorial sums of the two individual muon kinematic
 122 variables. The DY measurement is performed covering a wide range of the dimuon mass $30 <$
 123 $m^{\mu\mu} < 1500$ GeV.

124 The jets are selected from PF Jets with $p_T^{\text{jet}} > 30$ GeV and $|\eta^{\text{jet}}| < 4.5$.

125 In the following the combination of identification, isolation, and kinematic criteria of the muons,
 126 dimuons and jets are referred to as pre-selection. The event selection is applied on data and
 127 MC events.

128 4.1 Primray Vertex reconstruction and Pileup Reweighting

129 To reconstruct the primary vertices from the tracks of the particles, the Deterministic Annealing
 130 clustering method [20] is used. A selected vertex can be defined as a primary vertex if the z
 131 position of the vertex is within 24 cm of the nominal detector centre and the radial position
 132 within 2 cm from the beam spot. From this set of selected primary vertices the hard interaction
 133 vertex is selected as the vertex with the maximum sum of the transverse momenta of the tracks
 134 associated with this vertex.

135 To suppress the contamination from $\gamma\gamma \rightarrow \mu\mu$ events a minimum requirement on the number
 136 of degrees of freedom¹ on the primary vertex fit is set to four.

137 At high luminosities several pp interactions can happen simultaneously (pileup). In order to
 138 reproduce the number of pileup interactions observed in data, a weight factor is applied to
 139 the simulation based on the instantaneous luminosity and the total inelastic cross section, for
 140 which an uncertainty of 5% on the inelastic cross section is taken into account. The pileup
 141 reweighting procedure for the MC for the 2011 period as described in [22] is applied.

142 The normalized distribution of the number of primary vertices before and after pileup reweighting
 143 is shown in fig. 1.

144 4.2 Trigger Efficiencies

145 The trigger efficiency is defined as the fraction of events, where an identified muon can be
 146 matched to a trigger object. In order to account for the trigger inefficiency each MC event is

¹The number of degrees of freedom are defined as $n_{\text{ndof}} = 2 \sum_{i=1}^{N_{\text{tracks}}} w_i - 3$ with the track weight w_i of the i -th track. The weights are defined between $0 \leq w_i \leq 1$ and the value is assigned, taking into account the compatibility with the common vertex. This means, if the track is associated with the common vertex, the weight is set to one [21].

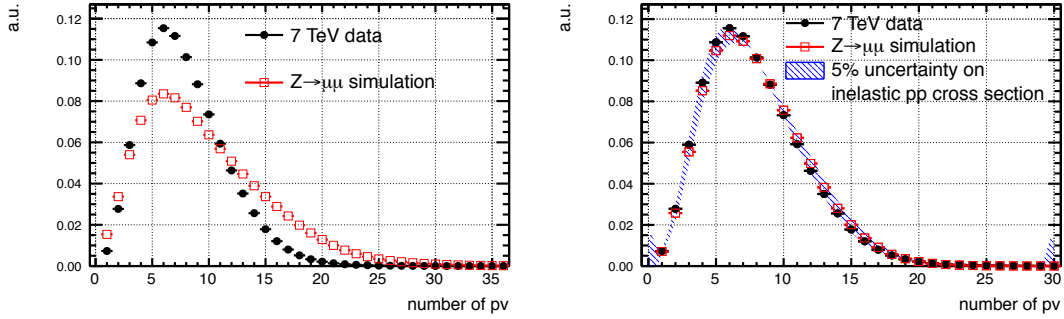


Figure 1: Number of primary vertices (pv) in data and simulation. The figure on the left shows the distribution before reweighting and the figure on the right shows the distribution after reweighting. A good agreement between data and MC is observed after the reweighting.

147 assigned a weight for the isolated muon trigger

$$\omega_{\text{trig}} = 1 - (1 - \epsilon^+(p_T, \eta)) \cdot (1 - \epsilon^-(p_T, \eta)), \quad (2)$$

148 where ϵ^+ (ϵ^-) is the p_T and η dependent single muon trigger efficiency for the two muons,
149 with positive and negative charge respectively. The double muon trigger has asymmetric p_T
150 thresholds for the leading and subleading muon. Therefore the efficiency is different for the
151 two p_T legs of the trigger. The weight for the double muon trigger is defined as

$$\omega_{\text{trig}} = \epsilon^{\text{high},+}(p_T, \eta) \cdot \epsilon^{\text{low},-}(p_T, \eta) + \epsilon^{\text{high},-}(p_T, \eta) \cdot \epsilon^{\text{low},+}(p_T, \eta) - \epsilon^{\text{high},+}(p_T, \eta) \cdot \epsilon^{\text{high},-}(p_T, \eta), \quad (3)$$

152 where ϵ^{high} is the p_T and η dependent efficiency of the higher p_T leg and ϵ^{low} the efficiency of
153 the leg with the lower p_T threshold. The run-dependent trigger selection in 2011 data-taking
154 are taken into account and the MC samples are divided according to the statistical fraction of
155 events corresponding to the luminosities, as shown in tabl. 1. In fig. 3 and 4 the efficiencies for
156 the higher and lower leg of the double muon trigger is shown as a function of the muon p_T in
157 bins of the muon η for the 2011A run.

158 4.3 Muon Identification

159 This analysis of the differential DY measurement is based on global and tracker muons. The
160 event is selected if the DY process decays into two muons, which can be reconstructed by the
161 tracker and global muon reconstruction algorithm. In order to perform a precise measurement
162 based on muon kinematics, the selection criteria are optimised to minimise the muon fake rate
163 while keeping the selection efficiency high. The basic muon identification algorithm used in
164 CMS is based on the PF Algorithm.

165 Muon candidates are reconstructed with the particle-flow (PF) algorithm [23, 24] which is
166 based on the tracker and the muon system. Muon candidates must pass the standard CMS
167 muon identification and quality control criteria, which are based on the number of hits found
168 in the tracker, the response of the muon detector and a set of matching criteria between the
169 parameters measured by the CMS tracker and those from the muon detector. Two oppositely
170 charged muons are selected if they fulfill the following preselection selection criteria.

171 The global muons should have at least one good muon hit. The tracker muons should have
172 at least two matches to muon segments in different muon stations. Furthermore the tracker

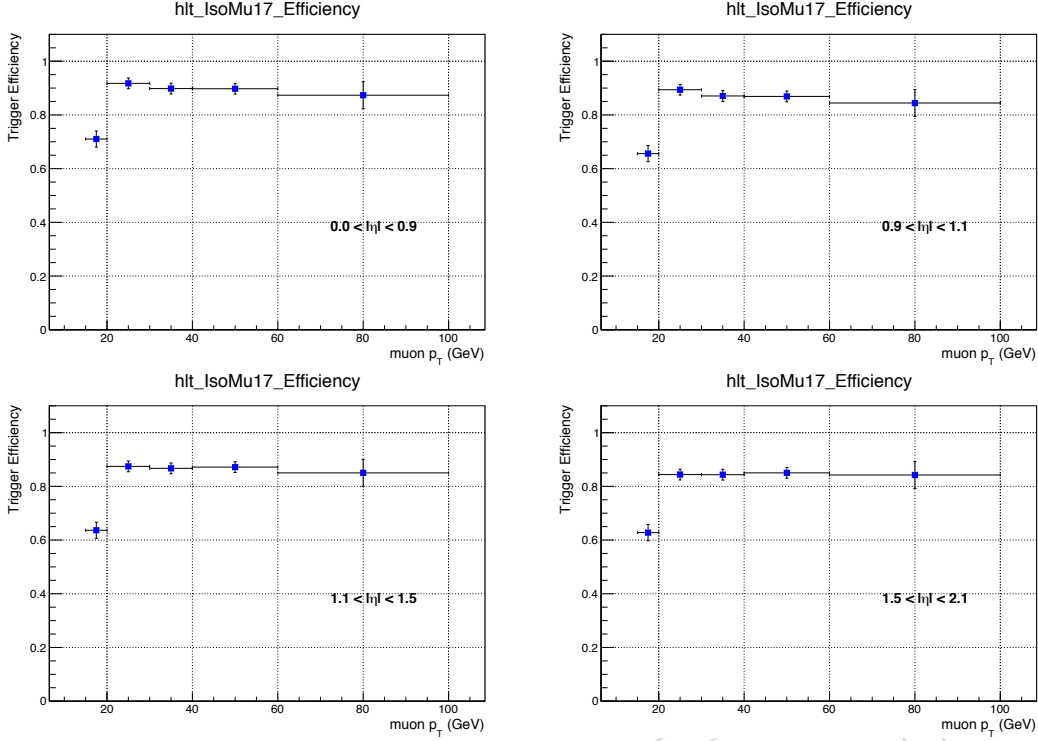


Figure 2: Trigger efficiency for the isolated single muon trigger HLT_IsoMu17 as a function of the muon p_T . The plots show different regions in η .

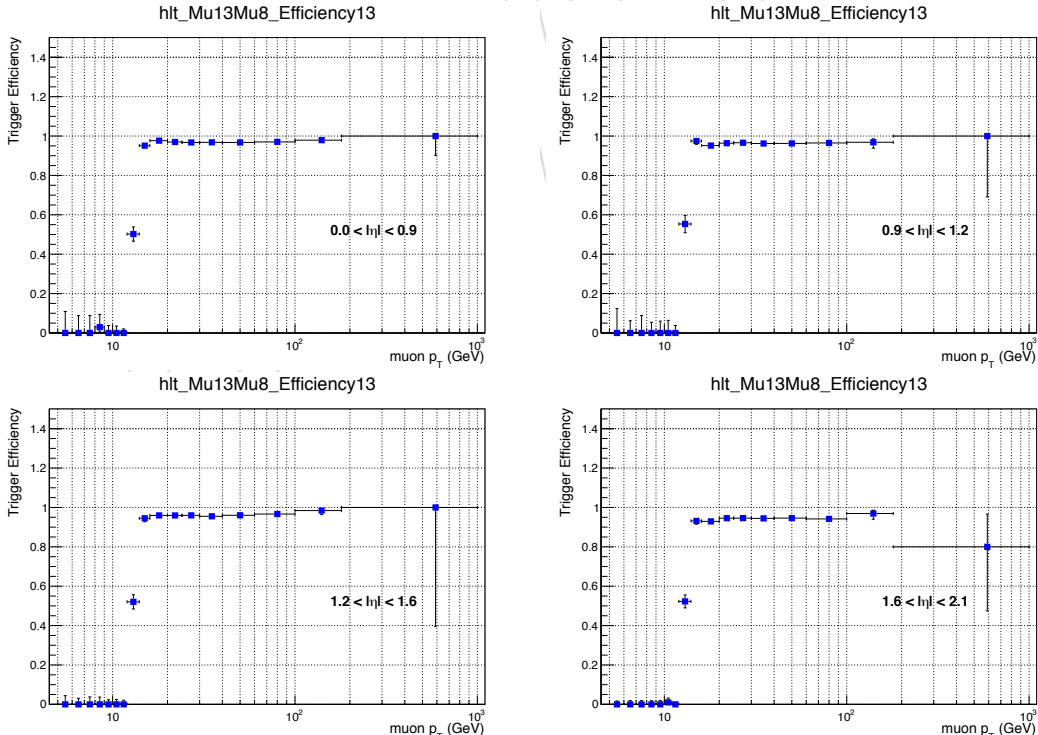


Figure 3: Trigger efficiency for the harder leg (13) of the double muon high level trigger. The scale factor is shown as a function of the muon p_T in bins of η .

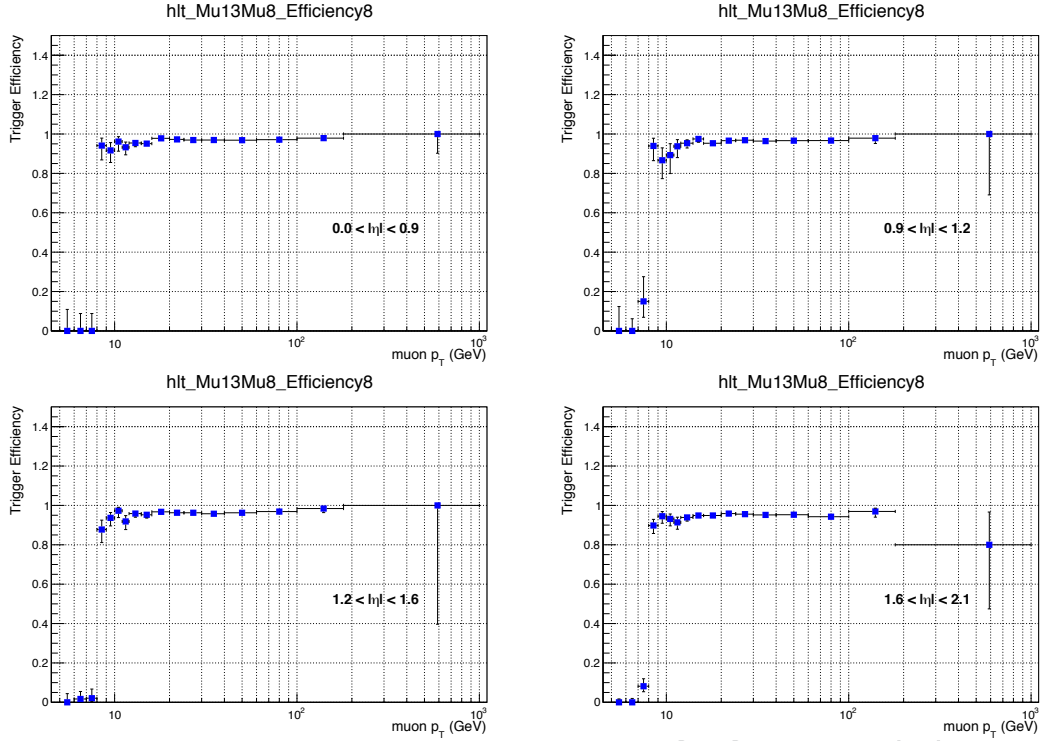


Figure 4: Trigger efficiency for the softer leg (8) of the double muon high level trigger. The scale factor is shown as a function of the muon p_T in bins of η .

173 muon is selected if it has more than 10 hits in the inner tracker and at least one pixel hit. The
 174 obtained global muon fit track should fulfill $\chi^2/\text{dof} < 10$. If the impact parameter in the
 175 transverse plane $|d_0| < 0.04\text{cm}$ w. r. t. primary vertex and the longitudinal impact parameter
 176 $|d_z| < 0.24\text{cm}$ w. r. t. primary vertex the event is selected.

177 Most criteria suppress muons from decays in flight, cosmic muons, and hadronic punch-through.
 178 The latter describes processes, when a fraction of a hadronic shower leaks into the muon system and is misidentified as a muon. Further, the requirements on the track reconstruction in
 179 the tracker and muon chambers, and on the global fit, ensure a good estimate on the muon
 180 trajectory by reducing the mismatching of tracker tracks and standalone tracks. Additionally,
 181 an accurate p_T measurement can be performed.

183 Events with muons are triggered by muon candidates within $|\eta^{\text{lead}\mu}| < 2.1$ and $|\eta^{\text{sublead}\mu}| < 2.4$
 184 with $p_T^{\text{lead}\mu} > 20 \text{ GeV}$ and $p_T^{\text{sublead}\mu} > 10 \text{ GeV}$.

185 The single and double muon high level trigger (HLT) conditions used in 2011 data taking are
 186 presented in tab. 3.

Table 3: High level trigger conditions.

| Trigger | Run Range | Luminosity [pb ⁻¹] |
|--------------|---------------|--------------------------------|
| HLT_IsoMu17 | 160404-170248 | 1170 |
| HLT_Mu13_Mu8 | 170249-180252 | 3723 |

187 In an electroweak process the final-state muons are well separated from additional activity of
 188 other particles; they are isolated. A muon emerging from a QCD process would be accom-

panied by a large number of low momentum jets (multi-jet events), thus, leaving tracks and energy deposits in the tracker and calorimeter. The isolation condition of a muon is necessary to discriminate between the different physics production processes of the muons. The muons under study are based on isolated muons. Therefore, a selection on the energy surrounding the muon in a certain cone in $\eta - \phi$ space, defined by $\Delta R = \sqrt{\Delta\eta^2 + \Delta\phi^2}$, is required. The isolation criterion is based on the PF based relative isolation variable defined as

$$\text{Iso}_\mu^{\text{PF}} = \frac{\sum (p_T^{\text{charged}} + p_T^\gamma + p_T^{\text{neutral}})}{p_T^\mu}. \quad (4)$$

The sum runs over the transverse momenta of all charged particles emerging from the hard interaction vertex. Only particles within a cone of $\Delta R < 0.4$ around the muon momentum are selected. In order to reduce the amount of energy coming from additional collisions, the sum has to be corrected for activity coming from pileup events. In the case of charged particles only particles, which correspond to the primary vertex are selected. In the case of neutral particles the track information is not available and the above requirement can not be arranged. Thus, a mean energy density ρ in a cone around the neutral particles is subtracted ($\Delta\rho$ correction). The relative $\Delta\rho$ corrected PF muon isolation is shown in Figure 5. The background contribution from QCD (multi-jet) processes dominates for high values of the isolation variable. At lower values the $Z\gamma \rightarrow \mu\mu$ process is dominant. Thus, the isolation selection for the dimuon system is required as

$$\text{Iso}_\mu^{\text{PF}} < 0.10 \quad \text{for} \quad p_T^\mu > 20 \text{ GeV}, \quad (5)$$

$$\text{Iso}_\mu^{\text{PF}} < 0.15 \quad \text{for} \quad p_T^\mu < 20 \text{ GeV}. \quad (6)$$

In this analysis the muons are selected according to the relative PF based selection criteria, presented above, and fulfil the relative combined PF isolation requirement in eq. (5) and (6). The looser criterion for muons with $p_T < 20$ GeV is needed to increase the selection efficiency on the softer muons. This is a crucial request for measurements of low invariant dimuon masses.

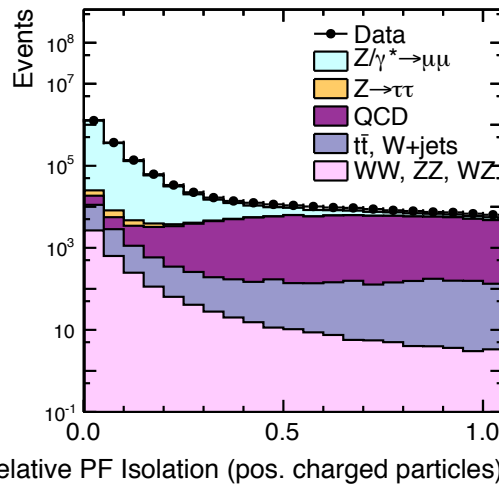


Figure 5: Relative PF isolation variable for positive charged muons.

210 The muon momentum measurement depends on the alignment of the tracker. After tracker
 211 alignment a residual misalignment remains, which affects the reconstruction of the muon mo-
 212 mentum. In order to recover the bias in data and MC simulation, the muon momentum scale
 213 has to be corrected. A detailed explanation on how the muon momentum scale correction is
 214 extracted is given in [25].

215 The muon momentum scale correction is derived as a function of the muon charge, η , and ϕ .
 216 Without the muon scale correction the average Z mass reveals a non-physical dependence on
 217 the muon η and ϕ . Including the muon scale correction improves the curvature of the muon
 218 with respect to the magnetic field and deformations in the transverse plane and it takes into
 219 account alignment effects.

220 4.4 Muon Efficiency

221 The efficiency on the muon identification selection is estimated using the tag-and-probe method.
 222 The identification efficiency is estimated from data and MC prediction using $Z \rightarrow \mu\mu$ events.
 223 The resulting values as a function of the muon p_T and are presented in Table 4. Differences
 224 between the MC and data efficiency are of the order of a few percent and within the sta-
 225 tistical uncertainties. Correction factor are defined as the ratio of data over MC efficiencies,
 226 subsequently referred to as scale factors. The last column in Table 4 shows the scale factors
 227 $\rho_{ID} = \frac{\epsilon_{data}}{\epsilon^{MC}}$. The scale factors are applied as an event weight to the MC events,

$$\omega_{ID}(p_T) = \rho_{ID}. \quad (7)$$

Table 4: Muon identification efficiency scale factors obtained from data and MC simulation in bins of muon p_T and η [26]. Statistical uncertainties are included and propagated to the scale factors.

| p_T (GeV) & η bin | MC Efficiency | Data Efficiency | Scale Factor |
|-------------------------------------|-------------------|-------------------|-------------------|
| 10.0 - 15.0 $ \eta < 1.5$ | 0.686 ± 0.004 | 0.680 ± 0.012 | 0.991 ± 0.018 |
| 10.0 - 15.0 $1.5 < \eta < 2.1$ | 0.652 ± 0.004 | 0.676 ± 0.014 | 1.036 ± 0.022 |
| 15.0 - 20.0 $ \eta < 1.5$ | 0.751 ± 0.002 | 0.748 ± 0.007 | 0.995 ± 0.010 |
| 15.0 - 20.0 $1.5 < \eta < 2.1$ | 0.718 ± 0.003 | 0.720 ± 0.010 | 1.002 ± 0.014 |
| > 20.0 $ \eta < 1.5$ | 0.930 ± 0.001 | 0.922 ± 0.001 | 0.992 ± 0.001 |
| > 20.0 $1.5 < \eta < 2.1$ | 0.895 ± 0.001 | 0.890 ± 0.001 | 0.994 ± 0.001 |

228 4.5 Jet Identification

229 The jets are reconstructed from PF objects and are defined by the anti- k_T clustering algorithm
 230 using the parameter $R = 0.5$. Jets are clustered from stable particles (decay length $c\tau > 10\text{mm}$)
 231 excluding the Drell-Yan decay product. The reconstructed jets have to be corrected to the abso-
 232 lute energy scale due to effects in the calorimeter response. The recommended MC corrections

233 applied are: L1FastJet, L2Relative and L3Absolute (GlobalTag: START42_V15B) and for data:
 234 L1FastJet, L2Relative, L3Absolute and L2L3Residual (GlobalTag: GR_R_42_V20).

235 The JEC can be factorised into several components, which imply different effects of the jet
 236 reconstruction: First the reconstructed jets, *RecoJets*, have to be matched to the GenJets. A global
 237 calibration factor is defined as the ratio of the energy of RecoJets over GenJets as a function of
 238 p_T^{jet} and η^{jet} . This calibration factor is applied to data and detector level simulation and removes
 239 the energy contribution in a jet coming from pileup events. However, differences between data
 240 and simulation give rise to additional corrections in the defined phase space. The aim of the
 241 correction in the second step (L2Relative) is to flatten the dependence of the jet response. The
 242 forward produced jets are corrected to have the same response as centrally produced jets. For
 243 this the p_T balance of dijets is used. In the third step (L3Absolute) the jet response in p_T is
 244 flattened. The absolute correction is used to scale the p_T response of the jets. The correction
 245 makes use of the p_T balance in Z+jet and γ +jet events. At the end the residual corrections
 246 (L2L3Residual) are applied to data only, which take into account remaining small differences
 247 between data and MC simulation and fix the relative energy scale [14].

248 The jet p_T resolution was studied in dijet and γ +jet events in [27] and it was observed that the
 249 measured resolution in simulation is better than in data. In order to improve the agreement of
 250 data and simulation, the simulated jets have to be smeared to describe the data. The smearing
 251 procedure is based on a scaling of the reconstructed and corrected jet p_T dependent on the p_T
 252 difference between the matched RecoJet and GenJet:

$$p_T \rightarrow p_T^{\text{gen}} + c (p_T - p_T^{\text{gen}}). \quad (8)$$

253 The factor c is the score resolution scaling factor defined as the ratio of data over MC resolution.
 254 The scaling factors are given in [28] and are estimated from dijet events. The JER smearing
 255 only works for well matched RecoJets to GenJets. This means, for each reconstructed jet j^{reco}
 256 the closest generated jet j^{gen} in $-\phi$ space is selected. The two jets are matched if the distance
 257 $\Delta R = \sqrt{\Delta\eta^2(j^{\text{reco}}, j^{\text{gen}}) + \Delta\phi^2(j^{\text{reco}}, j^{\text{gen}})}$ is smaller than a certain value. In this analysis the
 258 matching value is chosen to be $\Delta R < 0.4$.

259 In order to reduce the amount of jets coming from pileup a jet identification is included. The jet
 260 identifier uses vertex information and jet shape information to ensure the jet is a good jet [29].
 261 Additionally, certain requirements are added to reduce the fraction of fake jets coming from
 262 noise in the calorimeter. Furthermore, the identification criteria are arranged to select only
 263 hadronic jets with high efficiency. The identification criteria are defined in CMS by the *Loose*
 264 *PFJet Identification* [30]:

265 Corrected jets are selected if they satisfy the fiducial cuts of $p_T^{\text{jet}} > 30\text{GeV}$ and $|\eta^{\text{jet}}| < 4.5$. The
 266 jets should be isolated by the two muons in the final state by an isolation cone of $\Delta R > 0.5$.
 267 Furthermore the jets require the loose PF jet identification, defined by

- 268 • $|\eta^{\text{jet}}| > 2.5$: The neutral hadron energy fraction should be < 0.99 , the photon energy
 269 fraction should be < 0.99 and the number of constituents should be larger than 1.
- 270 • $|\eta^{\text{jet}}| < 2.5$: The neutral hadron energy fraction should be < 0.99 , the photon energy
 271 fraction should be < 0.99 and the number of constituents should be larger than 1.
 272 Additionally the number of charged constituents and the charged energy fraction
 273 have to be larger than 0 and the electron energy fraction < 0.99 .

274 In fig. 6 the jet multiplicity after preselection and the leading jet transverse momentum in the

275 Z Peak region (60-120GeV) is shown.

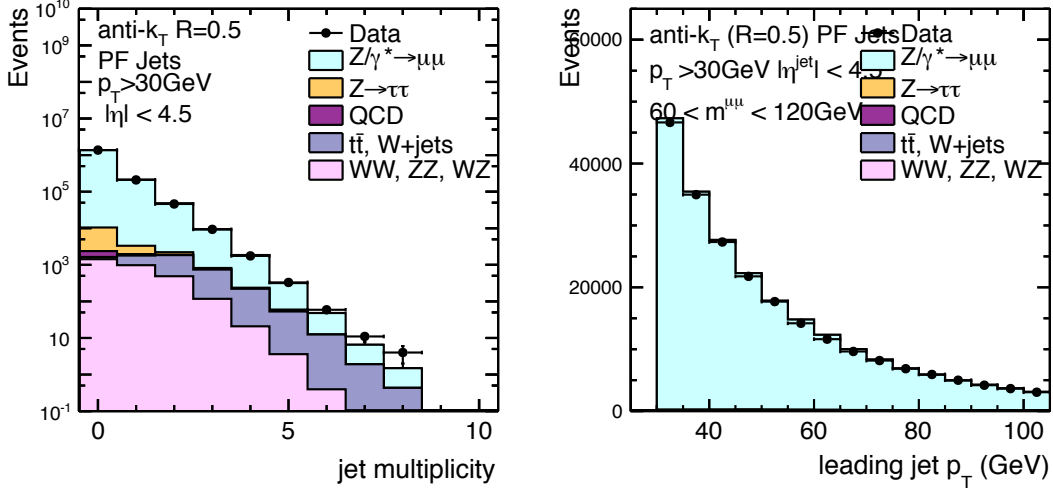


Figure 6: Jet multiplicity after preselection on the left and the leading jet transverse momentum in the Z peak region (60-120GeV) on the right. Both distributions are shown for PF jets after preselection. The experimental data are shown as circles and the MC background and signal samples are represented by filled histograms.

276 4.6 Drell-Yan Cross Section Measurement

277 The DY measurement is performed differentially in the dimuon transverse momentum $p_T^{\mu\mu}$.
 278 The $p_T^{\mu\mu}$ distribution provides a crucial test of pQCD. The different regions of the dimuon $p_T^{\mu\mu}$
 279 distribution are calculated by several theoretical calculations. In the region of $p_T^{\mu\mu} > Q$ (Q is
 280 the scale of the hard process) it follows a fixed-order calculation, but in the region of $p_T^{\mu\mu} \ll$
 281 Q the truncated perturbative expansion is not reliable and large-logs have to be resummed
 282 to all orders in pQCD. In the intermediate region nonperturbative effects contribute due to
 283 the intrinsic motion of the partons in the colliding hadrons. Thus, the sensitivity of different
 284 calculations and models depend on a physical scale Q , which can be interpreted as the invariant
 285 mass of the DY dimuon system $m^{\mu\mu}$. The measurement is performed differentially in mass
 286 $m^{\mu\mu}$, to use it as scale of the process. This is the first time in CMS that the $p_T^{\mu\mu}$ distribution is
 287 measured differentially in the dilepton invariant mass. Moreover, the inclusive DY production
 288 in the mass range of the Higgs boson ($m_{DY} \sim 126$ GeV) can be used to probe soft-gluon and
 289 multi-jet resummation from a quark and gluon induced process, by comparing the DY and
 290 Higgs. Details of how the comparisons are relevant for the future high luminosity runs at the
 291 LHC are described in [31].

292 The effect of resummation is of great interest for this analysis. The phase space for soft-gluon
 293 resummation can be enlarged when requiring additional jets in association with the DY boson
 294 production. For the first time in CMS the jets are selected in the full η region of the detector.
 295 Comparing inclusive DY production to DY and at least one jet above a certain p_T threshold, an
 296 increase of the region where resummation is important is observed. In this way it is possible
 297 to study the effect of resummation at low p_T by measuring multi-jet emissions. In this analysis
 298 three event topologies are compared:

299 1) Inclusive DY

300 Inclusive DY production with no further requirement on the jet selection

301 2) DY + 1 jet

302 Inclusive DY production with at least one jet above a p_T threshold of 30 GeV

303 3) DY + 2 jet

304 Inclusive DY production with at least two jets above a p_T threshold of 30 GeV

305 The Drell-Yan cross section measurement is performed in bins of the dimuon invariant mass
 306 covering the range of 30-1500GeV. The double differential cross section in Drell-Yan $p_T^{\mu\mu}$ is mea-
 307 sured in five bins of $m^{\mu\mu}$ and 19 bins in $p_T^{\mu\mu}$. In the case of Drell-Yan cross section in association
 308 with jets the binning in $p_T^{\mu\mu}$ is decreased to 13 bins due to statistics. At small masses (30-60GeV)
 309 resummed higher-order contributions dominate, due to emission of multiple soft gluons in the
 310 initial-state. Therefore higher-order QCD corrections as well as FSR effects are significant. This
 311 region is separated into two invariant mass bins from 30-45 and 45-60GeV. The intermediate
 312 mass region (60-120GeV) is dominated by Z boson exchange and is not divided again. In the
 313 high mass region, the distribution follows perturbative QCD corrections at fixed-order. This
 314 region is divided into two bins from 120-200 and 200-1500GeV. The double differential cross
 315 section as a function of the absolute rapidity separation between the Drell-Yan and the leading
 316 jet is measured in three bins of the dimuon invariant mass (30-60, 60-120, 120-1500GeV) and six
 317 bins in Δy . In order to account for bin-migrations the cross section is unfolded and corrected
 318 for detector effects. All cross sections are normalized to the integrated cross section in the Z
 319 peak region from 60-120GeV to reduce systematic uncertainties. In fig. 7 the dimuon transverse
 320 momentum distribution is shown for five invariant mass bins. The corresponding distributions
 321 for DY+1jet and DY+2jets events are shown in fig. 8 and 9.

322 4.7 Background Estimation

323 Different processes, which have the same signature in the final state, can be misidentified as DY
 324 dimuon pairs and are called background processes. With well-chosen selection requirements a
 325 large contamination from background processes can be reduced. However the remaining back-
 326 ground contributions have to be modelled precisely. The background events are subtracted
 327 from data events in order to be able to compare to signal MC predictions. Thus, an accurate
 328 simulation (estimated from data or MC simulation) of the background processes is needed in
 329 order not to bias the signal. The contribution from different background processes depends on
 330 the invariant mass of the dimuon, as shown in Figure 10 and in Table in tab. 2. In the Z peak
 331 region (60-120 GeV) the signal is nearly background free and the dominant contribution is Z bo-
 332 son exchange. In the low mass region (30-60 GeV) the main background contributions are due
 333 to multi-jet QCD events and the Z decaying into τ pairs. Beyond the Z mass (120-1500 GeV)
 334 the dominant source of additional dimuon production are $t\bar{t}$ and electroweak processes.

335 4.8 QCD Background Estimation from Data Events

336 Hard QCD processes in collisions produce multi-jet events in the final state. The jets are mainly
 337 produced by semi-leptonic decays of charm and bottom quarks, and are in general accompa-
 338 nied by non-isolated leptons in the final state. The isolation requirement, described in sec-
 339 tion 4.3, reduces most of the QCD background contribution. The remaining fraction of QCD
 340 events, e.g. coming from misreconstructed jets identified as isolated leptons, is estimated using
 341 a method based on data events. A technique using data events is performed to calculate the
 342 number of QCD events.

343 The muon net charge is uniformly distributed in QCD events, thus the number of opposite-sign
 344 (OS) and same-sign (SS) dimuon events are the same in the QCD sample. To estimate the back-
 345 ground contribution the data are separated according to the charge of the two muons in one

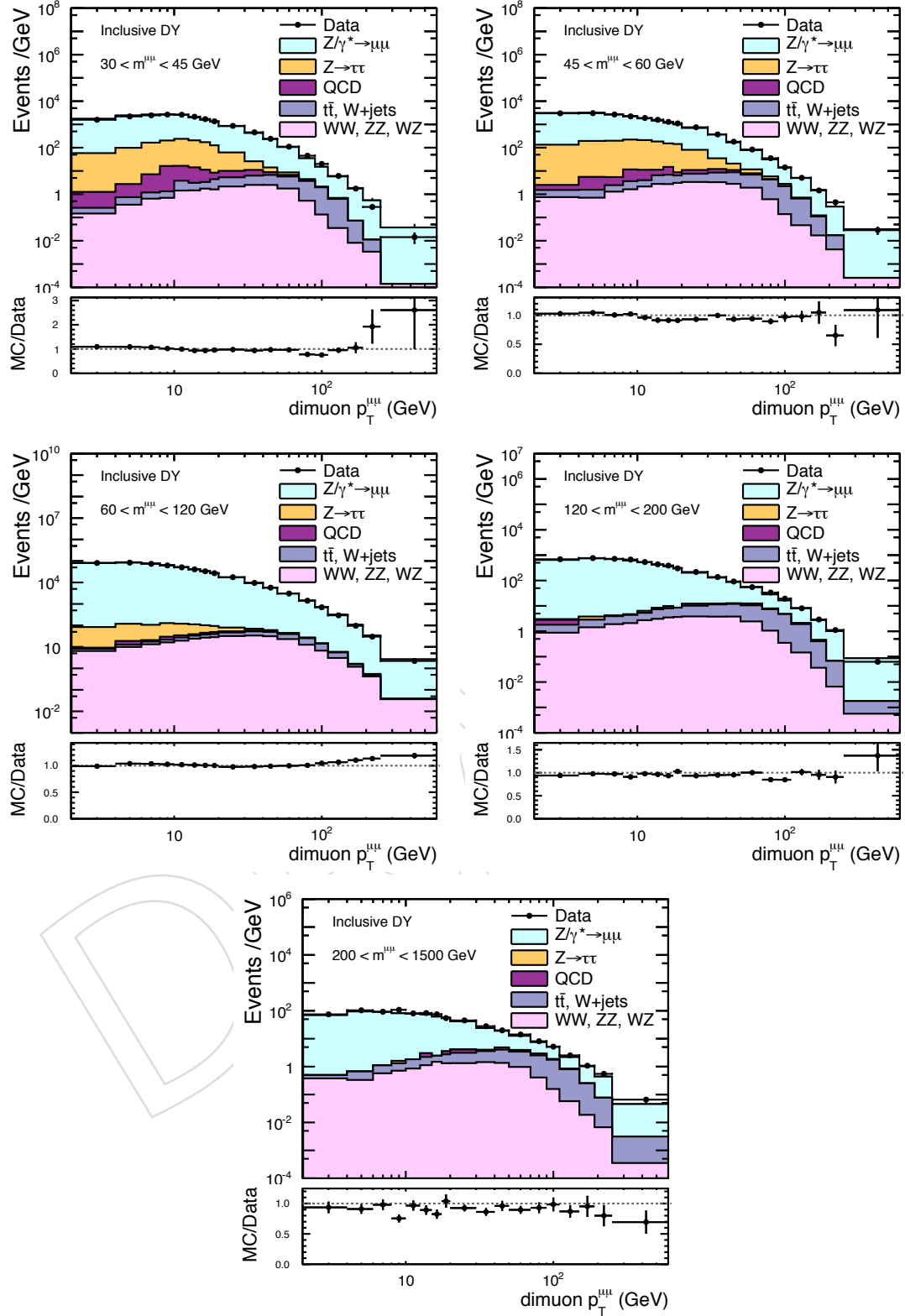


Figure 7: The Drell-Yan dimuon transverse momentum distribution in different bins per invariant mass covering a range from 30–1500 GeV. The histogram shows the entries normalized to the binwidth. The background distributions are added and the comparison from signal MC and data shows good agreement.

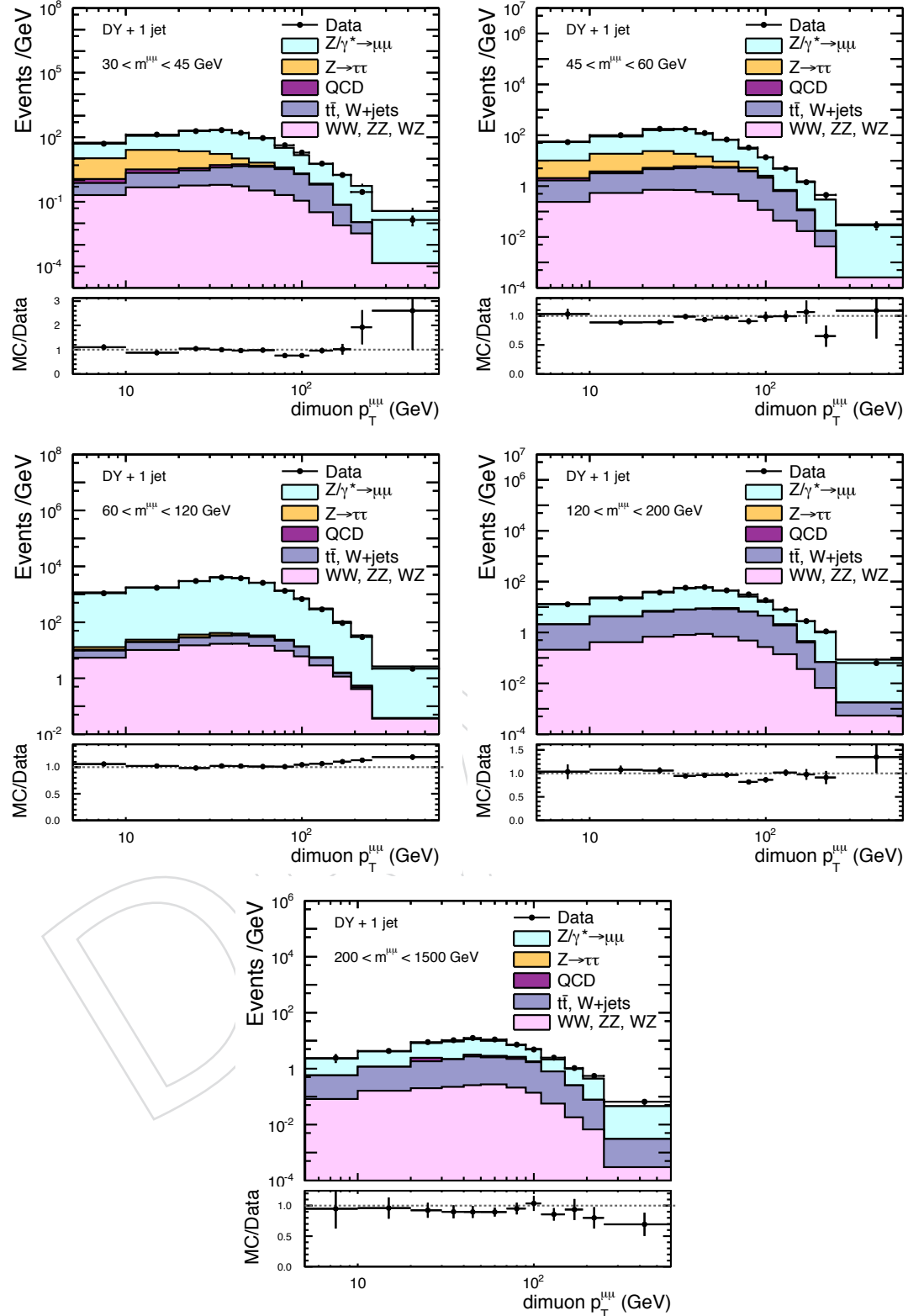


Figure 8: The Drell-Yan in association with at least one jet dimuon transverse momentum distribution in different bins per invariant mass covering a range from 30–1500 GeV. The histogram shows the entries normalized to the binwidth. The background distributions are added and the comparison from signal MC and data shows good agreement.

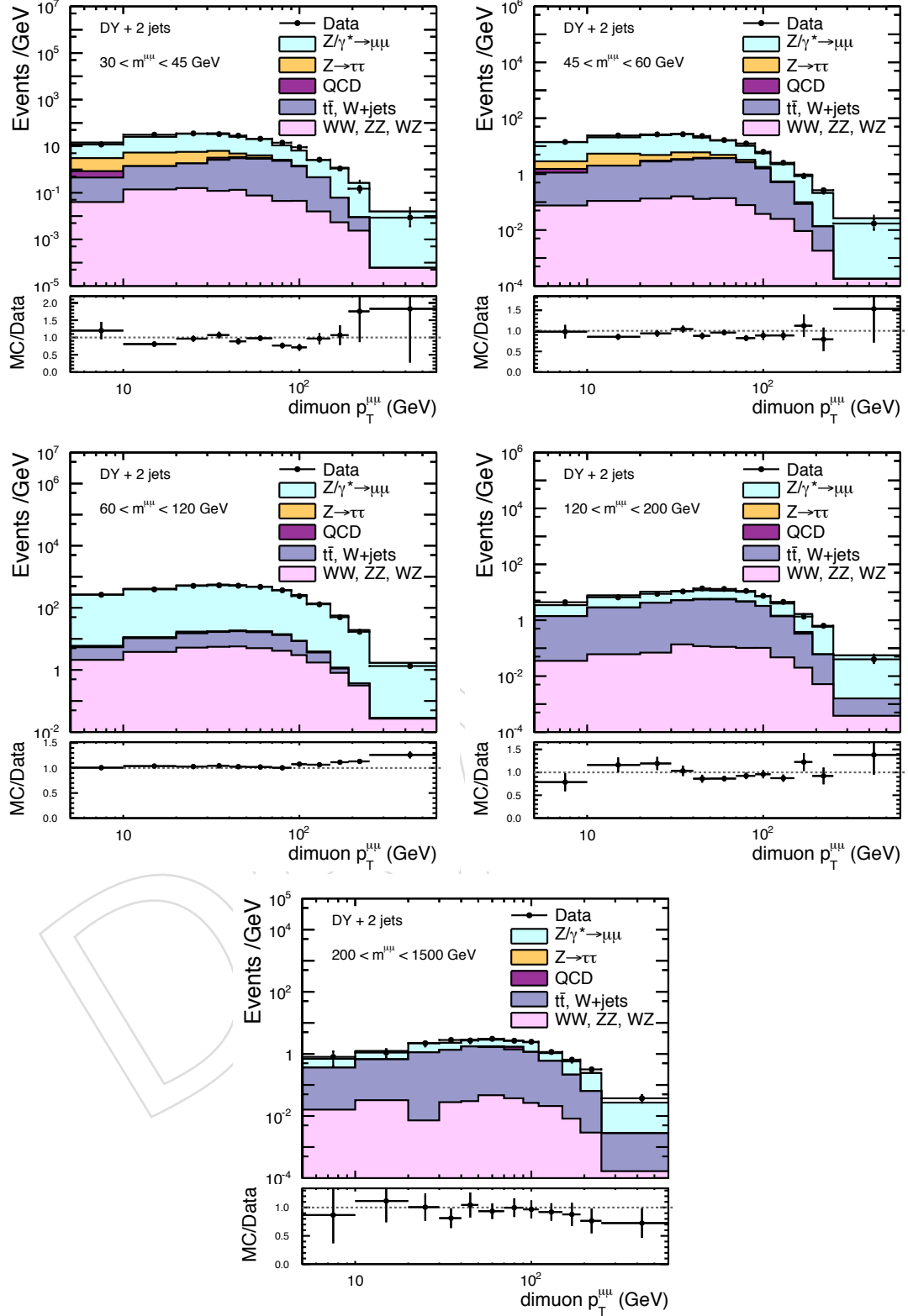


Figure 9: The Drell-Yan in association with at least one jet dimuon transverse momentum distribution in different bins per invariant mass covering a range from 30–1500 GeV. The histogram shows the entries normalized to the binwidth. The background distributions are added and the comparison from signal MC and data shows good agreement.

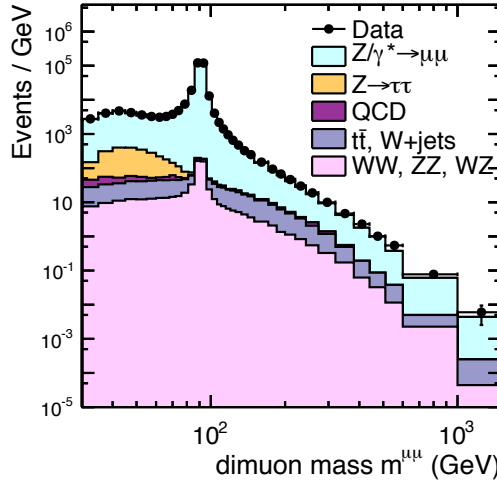


Figure 10: Drell-Yan di-muon invariant mass distribution for data and MC events and the corresponding ratio of the observed to expected yields. The histogram shows the entries normalized to the binwidth and no other corrections are applied. The background predictions are estimated by MC simulation except the QCD background for which a same-signed di-muon data sample was used.

opposite-sign ($\mu^+ \mu^-$) and one same-sign ($\mu^+ \mu^+$ or $\mu^- \mu^-$) sample. In Figure 11a and 11b the invariant mass distribution, before the isolation criterion is applied on the OS and SS dimuon data sample, are shown, respectively. It is observed that the SS dimuon sample is dominated by QCD processes. The SS sample can be used to estimate the QCD events of OS dimuons. The number of OS QCD events $N_{\text{QCD}}^{\text{OS}}$ are then estimated from the number of the SS data events $N_{\text{data}}^{\text{SS}}$, with isolated muons, by multiplying $N_{\text{data}}^{\text{SS}}$ with a correction factor to account for differences between the SS and OS sample

$$N_{\text{QCD}}^{\text{OS}} = N_{\text{data}}^{\text{SS}} (\text{Iso}_{\mu_{1(2)}} < 0.1(0.15)) \cdot R_{\text{QCD}}. \quad (9)$$

The correction R_{QCD} can not be calculated precisely in the signal-region, because the isolation requirement removes most of the QCD events, as shown in Figure 11c. Thus, R_{QCD} is obtained in a region, which is defined as the QCD dominant region with non-isolated muons, by using an anti-isolation of $\text{Iso}_{\mu_{1,2}} > 0.5$. The correction factor can be calculated by the ratio of OS over SS data events, with anti-isolation

$$R_{\text{QCD}} = \frac{N_{\text{data}}^{\text{OS}} (\text{Iso}_{\mu_{1,2}} > 0.5)}{N_{\text{data}}^{\text{SS}} (\text{Iso}_{\mu_{1,2}} > 0.5)}. \quad (10)$$

The number of events in the SS and OS sample are studied for different anti-isolation requirements and the ratio R_{QCD} is calculated. The results are presented in Table 5. Furthermore, it is verified that the shape of the SS and OS sample, after anti-isolation selection on the two muons, is similar in data and MC simulation, as shown in Figure 12. The number of OS events is approximately twice the number of SS events, therefore a correction factor of ~ 2 is applied to the number of SS data events. A cross-check with a MC QCD-enriched sample estimated by PYTHIA6 is performed. The value of the factor R_{QCD} is presented in Table 5 and is in agreement with data. An uncertainty on the ratio is obtained by

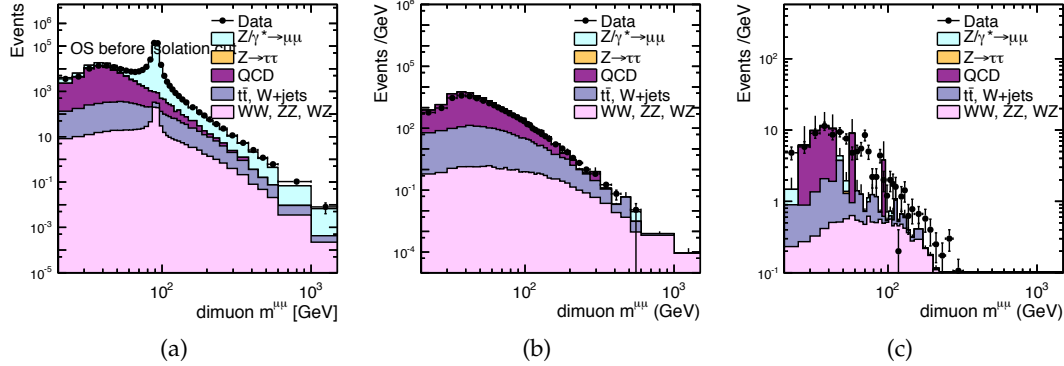


Figure 11: Invariant mass distribution for the opposite and same signed data samples. The left and middle plot show the contribution before the isolation cut. The right plot shows the remaining events in the same signed data sample after Isolation cut on the di-muon system.

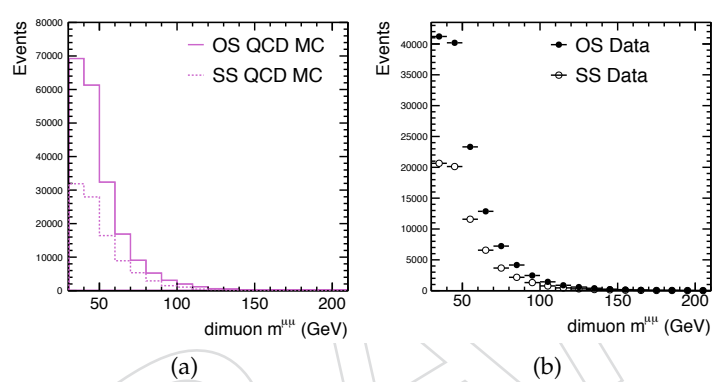


Figure 12: Distribution of the di-muon invariant mass in the OS and SS di-muon samples with inverse isolation cut.

taking the maximal difference between the nominal value, with $R_{\text{QCD}}(\text{Iso}_{\mu_{1,2}} > 0.5)$, and the ratios obtained by varying the isolation requirement between 0.2 and 0.4. The correction factor is estimated to be 1.98 ± 0.14 .

Table 5: Ratio of number of events in same-sign and opposite-sign dimuon samples with anti-isolation requirement in data and MC events.

| R_{QCD} | $\text{Iso} > 0.2$ | $\text{Iso} > 0.3$ | $\text{Iso} > 0.4$ | $\text{Iso} > 0.5$ |
|------------------|--------------------|--------------------|--------------------|--------------------|
| Data | 2.12 | 2.07 | 2.02 | 1.98 |
| MC | 2.02 | 1.99 | 1.95 | 2.04 |

369 4.9 Top pair Production

³⁷⁰ The top quark can decay into a bottom quark by radiation of a W boson, which can decay into
³⁷¹ a lepton and neutrino. The neutrino is not observed in the detector and can only be identified
³⁷² via missing transverse energy (E_{miss}^T). The E_{miss}^T variable is defined as the energy imbalance in
³⁷³ the transverse plane of the detector. This imbalance can occur due to particles, which do not
³⁷⁴ leave energy in the calorimeter and pass the detector unobserved. The missing energy in top

375 quark decays corresponds mainly to undetected neutrinos. The missing transverse energy is
 376 shown in Figure 13. The $t\bar{t}$ process is dominant in the region of $E_{\text{miss}}^T > 80 \text{ GeV}$.
 377 The top quark pair production is estimated from a simulated sample generated by MAD-
 378 GRAPH. The normalisation of the background contribution is taken from the CMS measure-
 379 ment of top quark pair production cross section [32] and a systematic uncertainty of 8% is
 380 assigned to the normalisation. Additionally the $t\bar{t}$ background process is controlled in the re-
 381 gion with, $E_{\text{miss}}^T > 80 \text{ GeV}$, where the $t\bar{t}$ contribution is dominant. A correction factor to take
 382 into account differences between data and MC events is derived by comparing the yields in
 383 the $t\bar{t}$ dominant region with $E_{\text{miss}}^T > 80 \text{ GeV}$, and is found to be 0.95 [33], which means the MC
 384 simulation is describing the data well.
 385 A study of the top quark pair kinematics modelling the region of $E_{\text{miss}}^T > 80 \text{ GeV}$ is provided
 386 in the following subsection. To reduce background contamination of $t\bar{t}$, a E_{miss}^T requirement of
 387 $E_{\text{miss}}^T < 80 \text{ GeV}$ is applied.

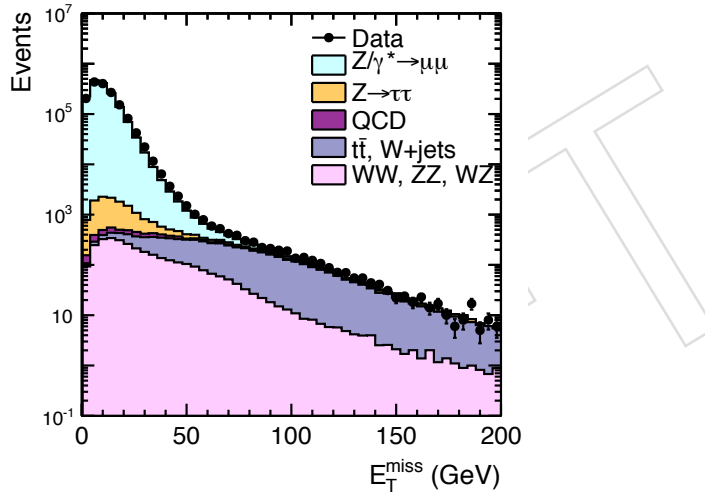


Figure 13: Distribution of missing transverse energy before applying the MET cut. The $t\bar{t}$ back-
 ground is controlled in the side-band region, $E_{\text{miss}}^T > 80 \text{ GeV}$, where the top pair events domi-
 nate the sample.

388 4.10 Diboson and W+jets Production

389 Contributions from diboson and single W production are estimated using a simulated sam-
 390 ple. The yields of diboson production are scaled to the cross sections predicted by theory at
 391 NLO [34, 35]. The contribution from single W production is normalised to the inclusive cross
 392 section as measured with CMS [36].

393 4.11 $Z \rightarrow \tau\tau$ Background

394 Another background process comes from Z decays into τ leptons, which subsequently decay
 395 into muons. The shape of $Z \rightarrow \tau\tau$ background process is estimated by MADGRAPH and nor-
 396 malised to the Z measured with CMS [36].

397 5 Cross Section Definition

The differential is measured as a function of the variable $X = p_T^{\mu\mu}, |\Delta y(\mu\mu, j_1)|$ by counting
 the number of events in the defined region of phase space using a limited binning in $X_i, i =$

$1, \dots, N_{\text{bins}}$. To obtain the value in bin i the corrected number of signal events has to be divided by the total luminosity of $\mathcal{L} = 4.9 \text{ fb}^{-1}$ and the binwidth ΔX_i . The differential cross section in bin i is then obtained by the formula

$$\frac{d\sigma}{dX_i} = \frac{N_i^{\text{sig,unfolded}}}{\Delta X_i \cdot \mathcal{L}}, \quad (11)$$

where $N_i^{\text{sig,unfolded}}$ corresponds to the number of signal events after unfolding in bin i

$$N_i^{\text{sig,unfolded}} = \sum_{j=1}^{N_{\text{bins}}} C_{ij}^{-1} \times (N_j^{\text{obs}} - N_j^{\text{bkg}}). \quad (12)$$

The number of signal events is obtained by subtracting the number of background events, N_i^{bkg} , which are estimated from data and MC simulation, from the number of observed events, N_i^{obs} . The matrix multiplication in eq. (12) represents the unfolding method to correct for bin migrations and detector resolution and efficiency.

The calculation, as presented in eq. (11), is performed in five bins of the dimuon invariant mass $m^{\mu\mu}$. The final results are presented as normalised distributions, by normalising the differential by the total integrated in the Z invariant mass range ($60 < m^{\mu\mu} < 120 \text{ GeV}$)

$$\sigma_Z = \sum_{j=1}^{N_{\text{bins}}} \frac{d\sigma}{dX_j} \cdot \Delta X_j, \quad (13)$$

with respect to the three topologies, inclusive DY, DY + 1, and DY + 2. The dependence on the luminosity cancels by taking the ratio. The normalised cross sections are

$$\left(\frac{1}{\sigma_Z} \right) \frac{d\sigma}{dp_T^{\mu\mu}} \quad \text{and} \quad \left(\frac{1}{\sigma_Z} \right) \frac{d\sigma}{d|\Delta y(\mu\mu, j_1)|}. \quad (14)$$

398 6 Monte Carlo Corrections

There exist several corrections to simulation in order to improve the agreement with data. The corrections are applied as an event weight ω_{MC} to the MC event and are combined in a product of individual weights, taking into account different effects. In addition to the absolute normalisation ω_{norm} (eq. (1)), the MC corrections take into account the effect of pileup, trigger efficiencies (eq. (2) and (3)), and efficiency correction factors (eq. (7)) due to muon identification. The total correction can thus be defined as the product

$$\omega_{\text{MC}} = \omega_{\text{norm}} \cdot \omega_{\text{PU}} \cdot \omega_{\text{trigger}} \cdot \omega_{\text{ID}}. \quad (15)$$

399 6.1 QED Final-State Radiation

400 The final-state leptons of the DY process are able to emit photons, which is referred to as QED
 401 FSR. The radiated photons are emitted nearly collinear to the final-state muon and can affect
 402 the invariant mass of the dimuon when the emitted photons have sizeable energy. The MC
 403 truth final-state muons can thus be defined with respect to the QED FSR. The final-state muons
 404 before QED FSR refer to born muons, while muons after QED FSR are defined as bare muons.
 405 The effect of the QED FSR on the dimuon invariant mass is shown in Figure 14 by comparing
 406 $m^{\mu\mu}$ before and after QED FSR.

407 It is observed that the effect is most significant just below the Z resonance. The other invariant
 408 mass regions are not significantly affected. In this analysis the final-state muons refer to muons
 409 after QED FSR, which are bare muons.

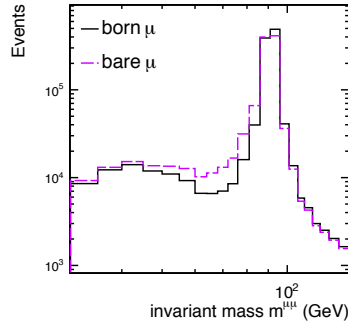


Figure 14: the number of events as a function of the dimuon invariant mass for bare and born muons is presented.

410 7 Migration study due to detector resolution and pileup jets

411 In the cases of the DY+1jet and DY+2jets production events are selected based on the jet p_T
 412 threshold of 30GeV. To study the effect of migrations the hadron level and detector level events
 413 have to be matched by matching the dimuon pair and the jets in $\eta - \phi$ space with and $\Delta R^{\mu\mu} <$
 414 0.3 and $\Delta R^{\text{jets}} < 0.4$. Sufficient variables to study the bin migrations are the purity and the
 415 stability of a bin i . The purity is defined as

$$P_i = \frac{N_{\text{matched}}(E_{\text{det}} \in i \wedge E_{\text{had}} \in i)}{N_{\text{matched}}(E_{\text{det}} \in i)} \quad (16)$$

416 referring to the number of reconstructed events which belong to bin i also on generator level.
 417 The variables E_{had} and E_{det} level correspond to the observables under study (e.g. $p_T^{\mu\mu}$ or
 418 $|\Delta y(\text{DY}, j_1)|$ on hadron and detector level, respectively. The stability is defined as

$$S_i = \frac{N_{\text{matched}}(E_{\text{det}} \in i \wedge E_{\text{had}} \in i)}{N_{\text{matched}}(E_{\text{had}} \in i)} \quad (17)$$

419 referring to the number of generated events $E_{\text{had}} \in i$ which remain in the bin when going to
 420 detector level $E_{\text{det}} \in i$.

421 Due to migrations around the p_T threshold some fraction off events at detector level do not
 422 have a corresponding jet on generator level and vice versa. These events are represented in the
 423 background and acceptance distribution defined as

$$B_i = 1 - \frac{N_{\text{matched}}(E_{\text{det}} \in i)}{N_{\text{all}}(E_{\text{det}} \in i)}, A_i = \frac{N_{\text{matched}}(E_{\text{had}} \in i)}{N_{\text{all}}(E_{\text{had}} \in i)} \quad (18)$$

424 Jets can come from pileup interactions and appear in the phase space defined by jet $p_T > 30\text{GeV}$.
 425 Thus pileup can introduce some background into our final distribution for DY+1jet and DY+2jets.
 426 Migrations into the phase space due to the jet p_T migrations and pileup are treated in indepen-
 427 dent ways. To decouple the two effects four different event classes are compared:

- 428 • all reconstructed jets with $p_T > 30\text{GeV}$
- 429 • matched jets with $p_T^{\text{reco}} > 30\text{GeV}$ and $p_T^{\text{gen}} > 30\text{GeV}$
- 430 • matched jets with $p_T^{\text{reco}} > 30\text{GeV}$ and $p_T^{\text{gen}} < 30\text{GeV}$

- 431 • no matched jet on generator level to the reconstructed jet with $p_T > 30\text{GeV}$
- 432 In fig. 15 the jet transverse momentum, pseudorapidity and multiplicity is plotted for the four
433 cases. The ratio is taken to the inclusive class where all reconstructed jets are selected above
434 threshold.

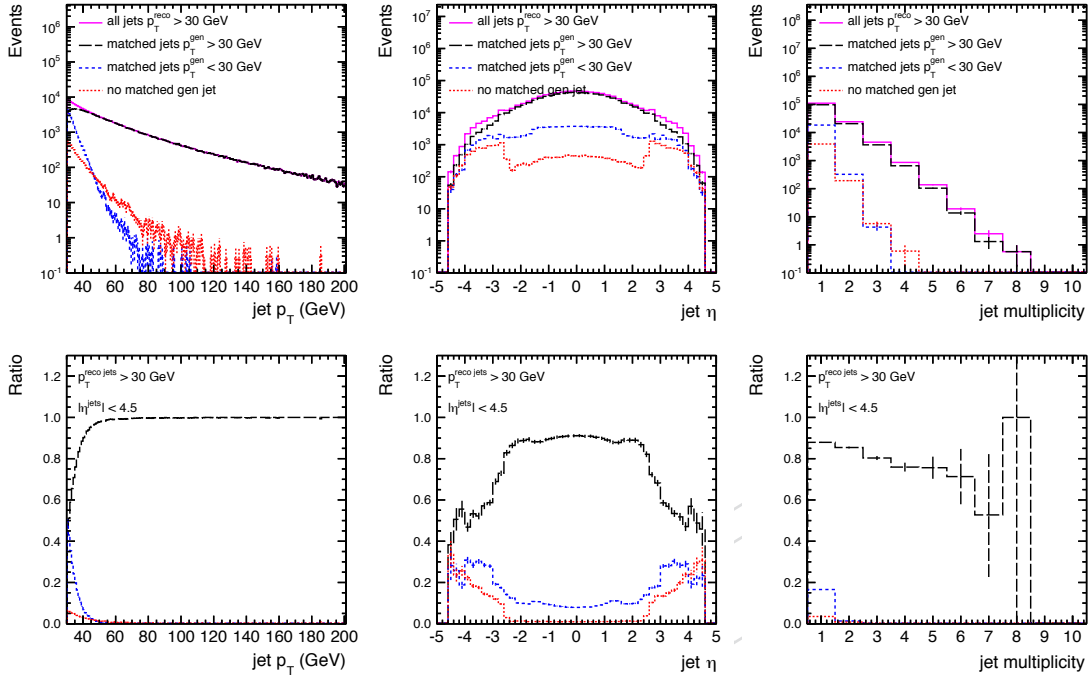


Figure 15: Jet control distributions comparing different event classes to investigate the migration effects due to the jet p_T and pileup jets. The ratio is taken to the inclusive topology.

- 435 The different event topologies are also compared for the dimuon transverse momentum dis-
436 tribution and Δy of the Drell-Yan and the leading jet in different invariant mass bins. The
437 observable affected by migration effects and pileup jets entering our final distributions is the
438 selected number of jets in the cases of DY+1jet and DY+2jets and the leading jet in $\Delta y(\mu\mu, j_1)$.
- 439 The dimuon $p_T^{\mu\mu}$ for DY+1jet and DY+2jets in the invariant mass bins of 30-45GeV, 60-120GeV
440 and 120-200GeV are shown in fig. 16 and 17, respectively.
- 441 The comparison of the different effects for the Δy distribution in the case of DY+1jet and
442 DY+2jets are shown in fig. 18 and 19, respectively.
- 443 In the first two dimuon p_T bins (0-10GeV) the contribution from pileup jets is the largest. In
444 the low invariant mass bins (30-45GeV and 45-60GeV) and at low $p_T^{\mu\mu}$ the contribution from
445 pileup jets is around 30-40%. In all the other bins in $p_T^{\mu\mu}$ and $m^{\mu\mu}$ the effect is below 20%. The
446 effect from pileup jets for the Δy distribution become important for $\Delta y > 4$. In this region the
447 contribution is $\sim 40\%$. To reduce the effect from pileup jets the cross section measurement in
448 Δy is performed in six bins up to $\Delta y = 6$.
- 449 The jets coming from pileup interactions and the effects due to jet p_T migrations into the fiducial
450 region are taken into account in the unfolding method.

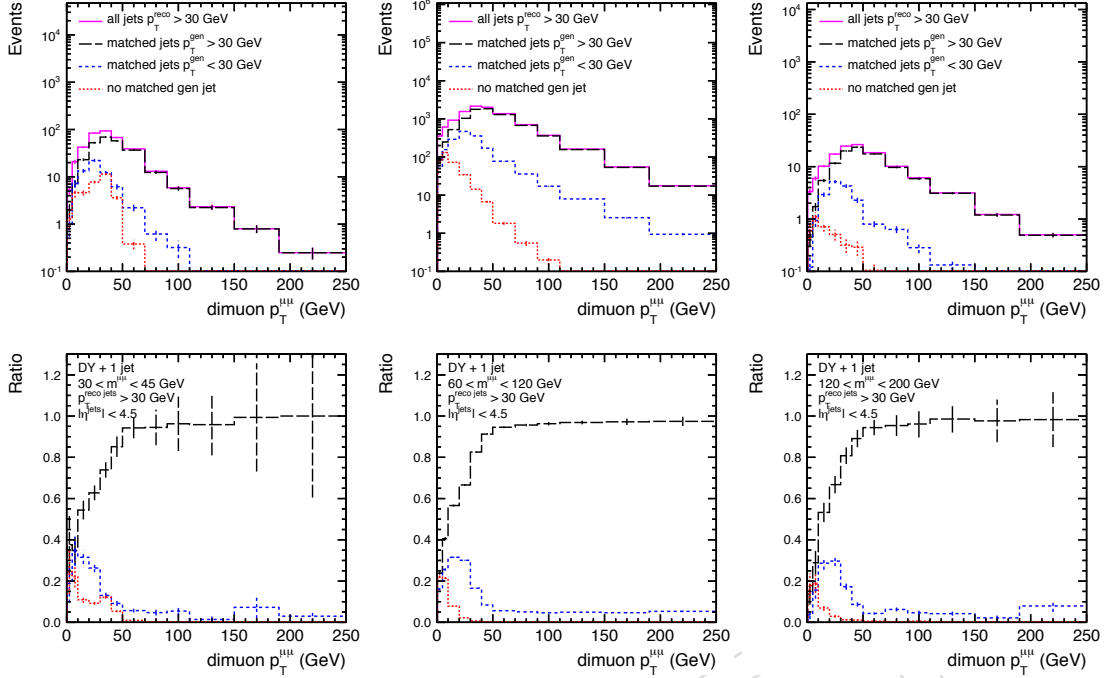


Figure 16: Dimuon transverse momentum for the DY+1jet case in three different invariant mass bins. The ratio is taken to the inclusive topology.

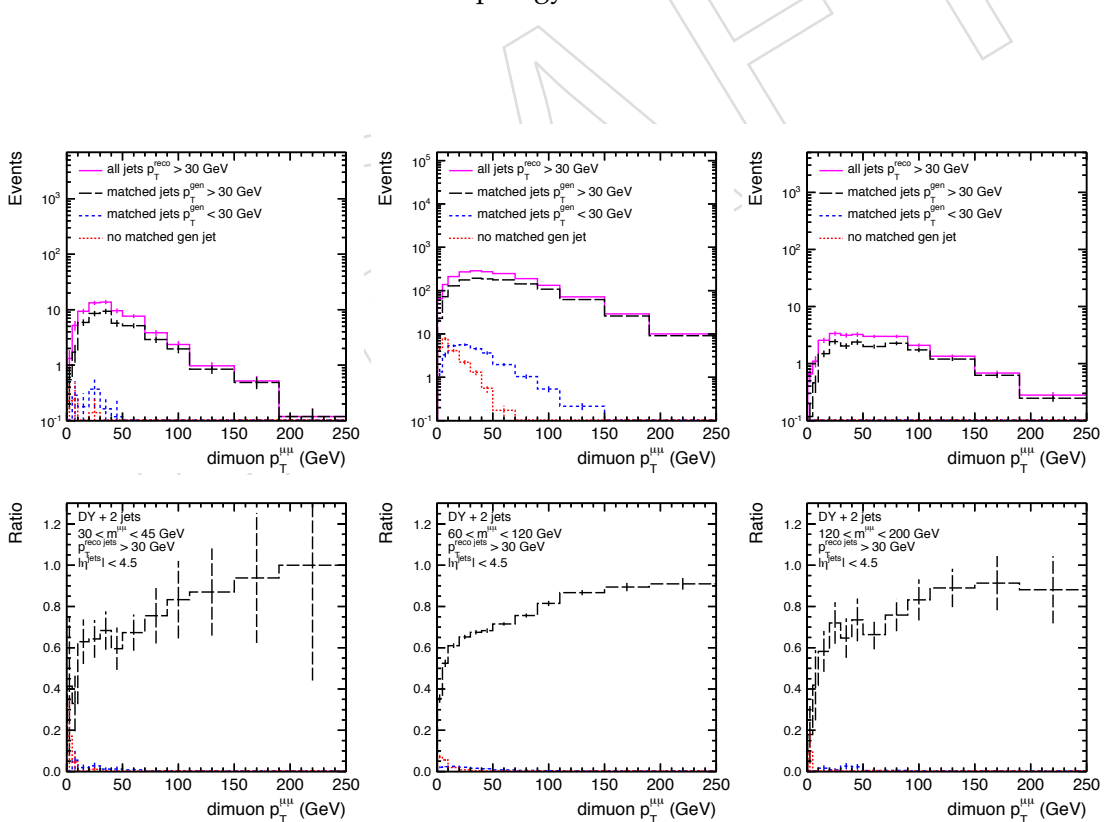


Figure 17: Dimuon transverse momentum for the DY+2jets case in three different invariant mass bins. The ratio is taken to the inclusive topology.

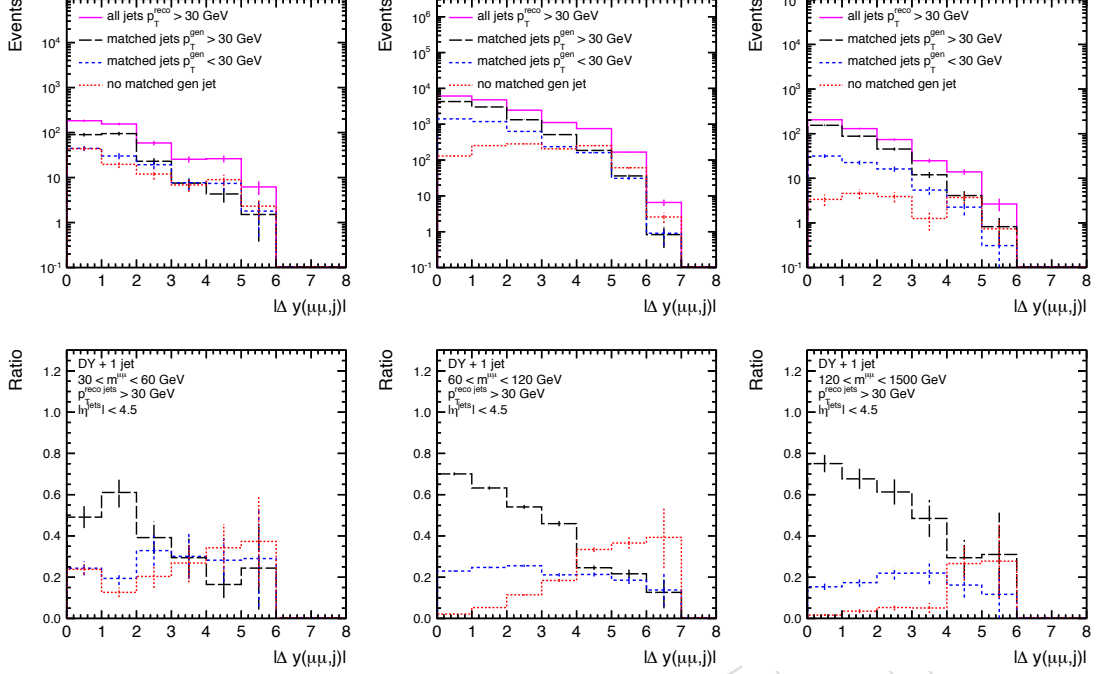


Figure 18: Absolute rapidity separation between the leading jet and the forward DY is shown for the different event topologies for the DY+1jet case in three different invariant mass bins. The ratio is taken to the inclusive topology.

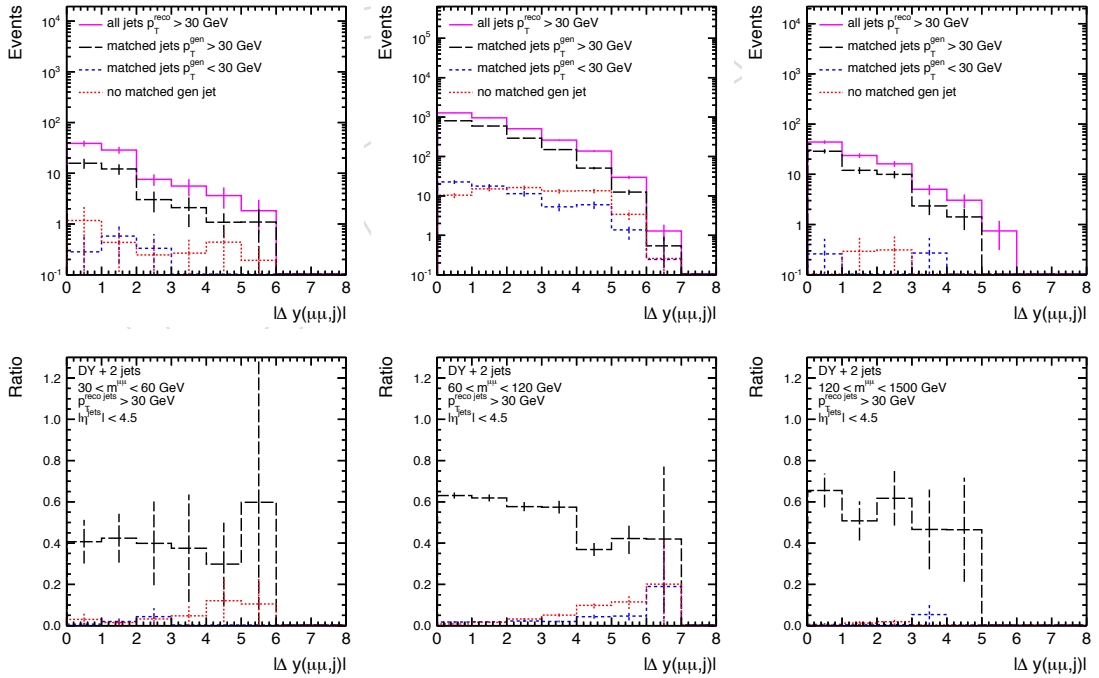


Figure 19: Absolute rapidity separation between the leading jet and the forward DY is shown for the different event topologies for the DY+2jets case in three different invariant mass bins. The ratio is taken to the inclusive topology.

451 7.1 Detector Resolution

452 The observed number of events have to be corrected for detector resolution effects. A recon-
 453 structed $p_T^{\mu\mu}$ can appear in a bin different from its truth $p_T^{\mu\mu}$ due to limits in the detector reso-
 454 lution. Thus the bin size is chosen to be larger than the resolution to cover migration effects to
 455 neighboring bins. The purity for the dimuon transverse momentum distribution for inclusive
 456 Drell-Yan production with invariant mass $60 < m^{\mu\mu} < 120 \text{ GeV}$ is shown in fig. 20. For small $p_T^{\mu\mu}$
 457 the purity is around 80% and for larger $p_T^{\mu\mu}$ the bin-purity increases to 90% due to increased bin
 458 sizes. This behavior is similar also for the other invariant mass bins, and for the DY+1jet and
 459 DY+2jet production (see appendix A). All in all the purity is $>60\%$ for the different produc-
 460 tion processes. In fig. 20 the normalized response matrix for the inclusive Drell-Yan transverse
 461 momentum is shown. The off-diagonal elements are better than 10% of the neighboring bins,
 462 which also indicates small migration effects in the transverse momentum variable. The corre-
 463 sponding response matrices for the DY+1jet and DY+2jets production in all invariant mass bins
 are shown in appendix A.

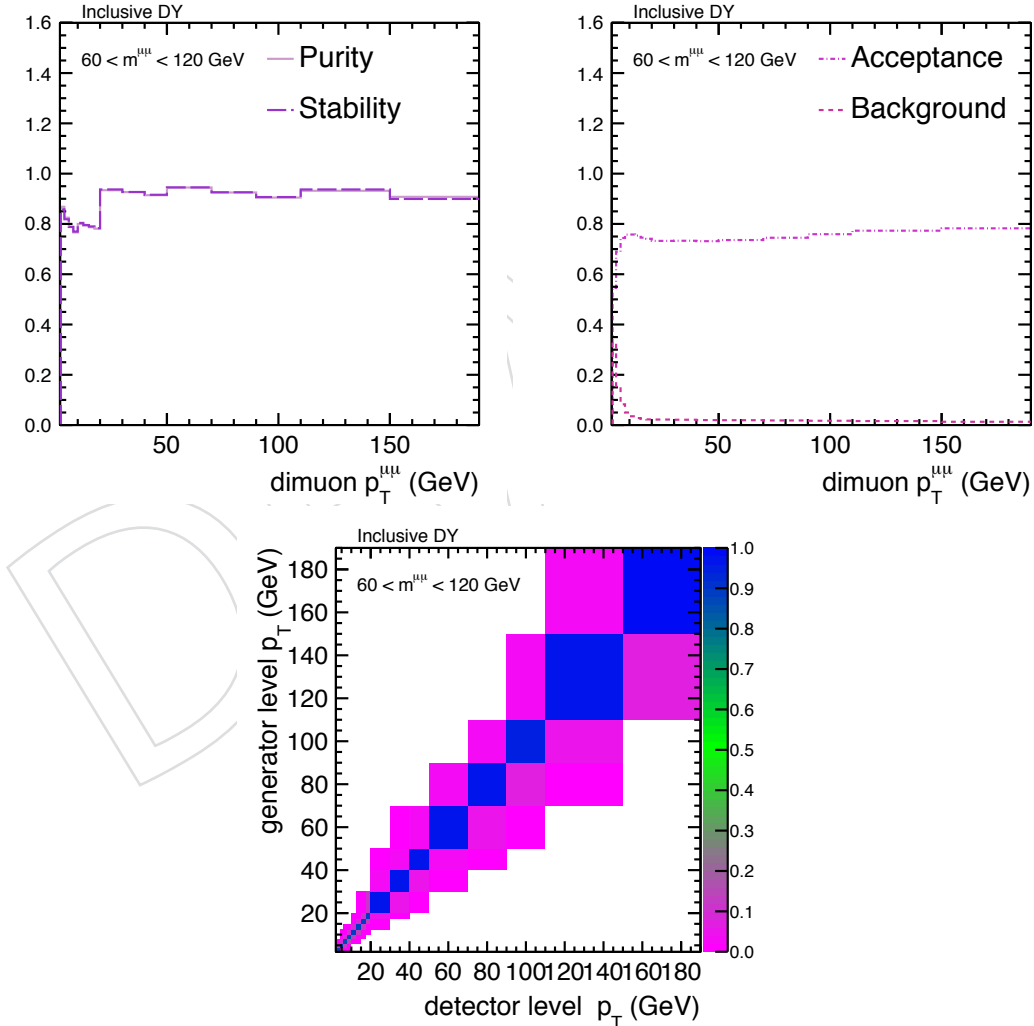


Figure 20: Purity, Stability, Acceptance and Background efficiencies for the inclusive Drell-Yan transverse momentum in the mass range of $60 < m^{\mu\mu} < 120 \text{ GeV}$ (top). The normalized response matrix of matched reconstructed and generated dimuon $p_T^{\mu\mu}$ (bottom).

465 In the case of the differential cross section in $|\Delta y(\mu\mu, j_1)|$ the purity and stability is $> 75\%$ for the
 466 different mass bins. In fig. 21 the purity of the $|\Delta y(\mu\mu, j_1)|$ distribution is shown in the case of
 467 the DY+1jet production. The normalized response matrices for matched events are presented
 468 in fig. 22. The migration effects to neighboring bins is less than 10%. A detailed study using
 469 MADGRAPH MC sample and comparing to other MC samples is discussed in the appendix C.
 470 The Bayes unfolding method [37] is used for the unfolding. Jets coming from pileup interactions
 471 as well as effects due to jet p_T migrations into the fiducial region are taken into account by
 472 the unfolding procedure. The migration effect in and out of the fiducial region is of the order
 473 of 30 % at low dimuon p_T . For $p_T > 40$ GeV the migration effects are $< 20\%$.

474 7.1.1 Model Dependence

475 To correct for detector effects and bin migrations the MADGRAPH +PYTHIA predictions are
 476 used to fill the response matrix and model the migration effects. MADGRAPH to data compari-
 477 sons provide already a good agreement on detector level and thus, MADGRAPH can be used to
 478 model the response matrix. However, the theory model does not necessarily describe the same
 479 migrations observed in data. Therefore, an uncertainty on the input model, which is used to
 480 fill the response matrix, is needed.

481 The migration effects depend on the shape of the distribution. A flat distribution reveals small
 482 migrations, while a steeply falling distribution predicts larger migrations. The theory, to be
 483 used to correct for detector effects, should already describe the data on detector level, in order
 484 to predict the shape and thus the migrations in an optimal way.

485 To estimate an uncertainty on the model, a parametrisation of the data points is employed. The
 486 parametrisation gives an estimate on how the shape of the distribution can vary within the sta-
 487 tistical uncertainty of data. The parameters are given with an uncertainty taking into account
 488 the statistical uncertainty on the data. By changing the fit parameters within their uncertainty,
 489 one can estimate to which extend the shape of the distribution can vary but still being consis-
 490 tent with data.

491 The parametrisation function is chosen in order to describe the data on detector level. In case
 492 of the dimuon $p_T^{\mu\mu}$ distribution, the low $p_T^{\mu\mu}$ region is parametrised by a Gaussian function,

$$g(p_T^{\mu\mu}) = c \cdot e^{-\frac{1}{2} \left(\frac{p_T^{\mu\mu} - m}{s} \right)^2}, \quad (19)$$

493 and the $p_T^{\mu\mu}$ tail is parametrised by an exponential function,

$$e(p_T^{\mu\mu}) = e^{p_0 + p_1 \cdot p_T^{\mu\mu}}. \quad (20)$$

494 The parameters c, m, s (which represent a constant, mean, and sigma respectively) and p_0 and
 495 p_1 are obtained by the fitting procedure.

496 In case of the $|\Delta y(\mu\mu, j_1)|$ distribution, the data is parametrised by a linear function

$$l() = p_0 \cdot \Delta y + p_1. \quad (21)$$

497 The uncertainty on the fit parameters are used to reweight the MADGRAPH +PYTHIA predic-
 498 tions, according an event weight defined as $\omega_{\text{model}} = \frac{p^\pm}{p^{\text{nominal}}}$. p^\pm indicates the parametrisa-
 499 tion with varying the fit parameters up and down their uncertainties and p^{nominal} refers to the
 500 parametrisation with nominal fit parameters. The nominal predictions from MADGRAPH and

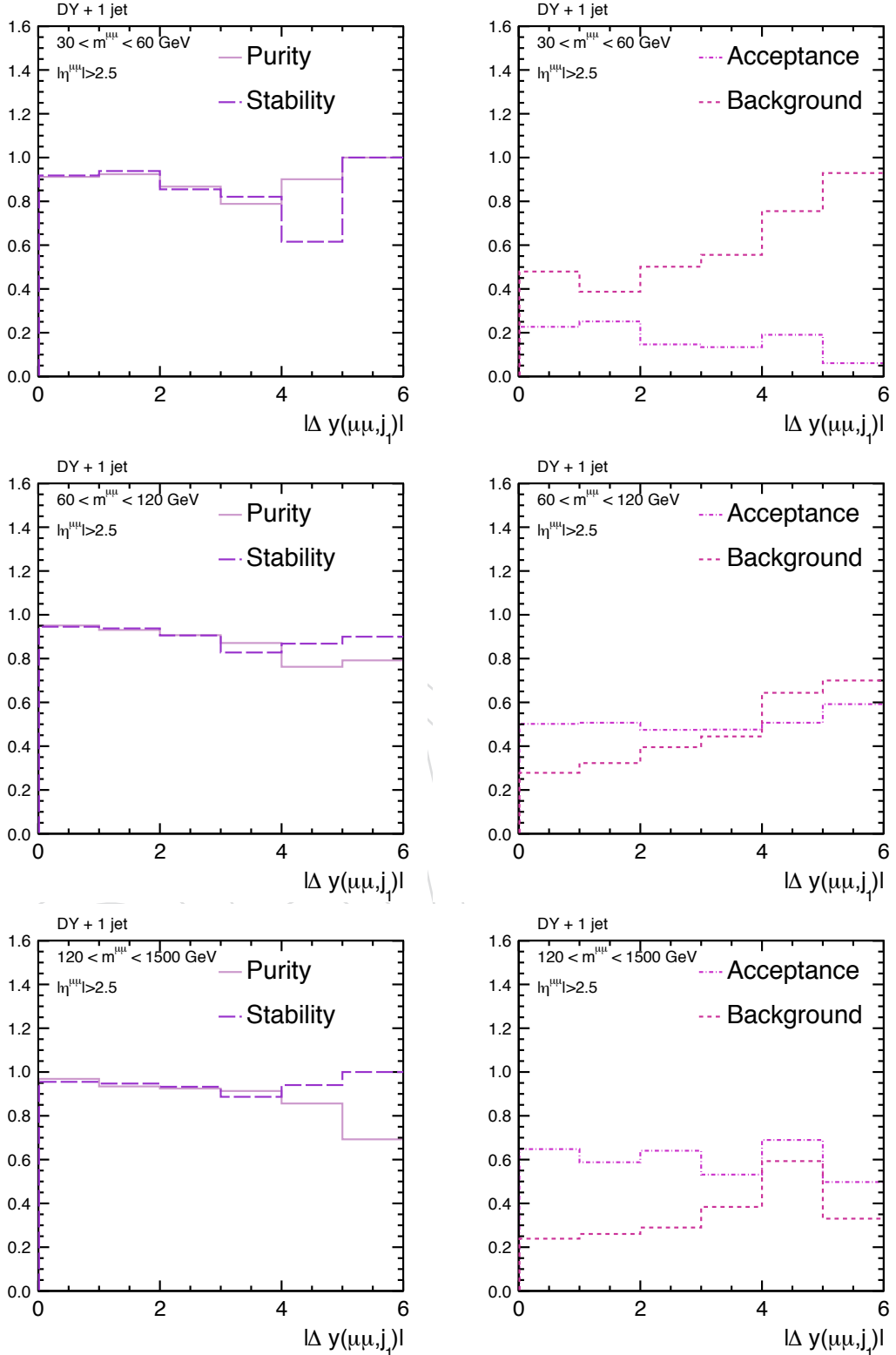


Figure 21: Purity, Stability, Acceptance and Background efficiencies for the DY+1jet production for $|\Delta y(\mu\mu, j_1)|$ in three bins of the invariant mass.

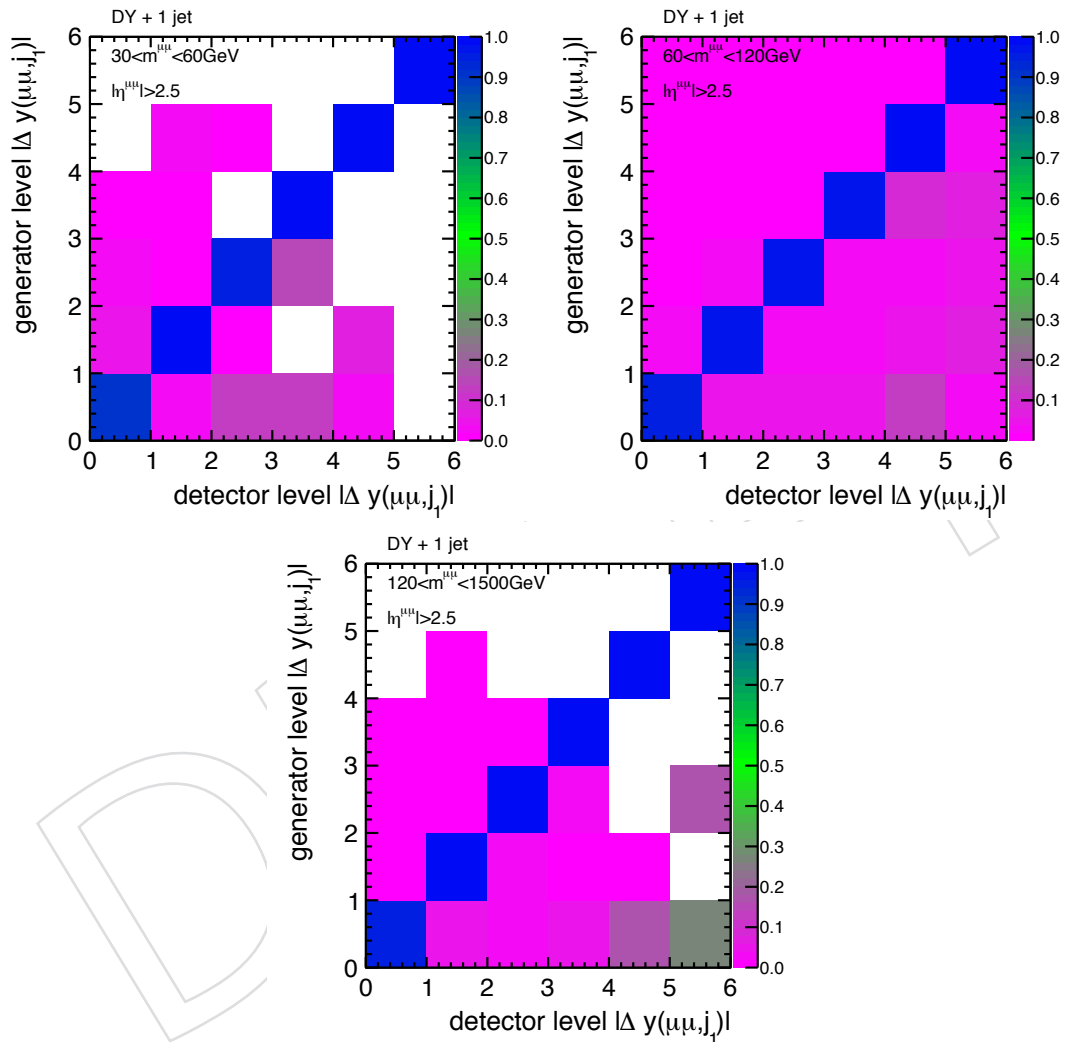


Figure 22: Normalized response matrix for the $|\Delta y(\mu\mu, j)|$ distribution for matched dimuons and jets in the case of DY+1jet production.

501 the model uncertainty obtained from the reweighted results show good agreement to data, as
 502 presented in Figures 23 and 24. The data values are compared to the MADGRAPH +PYTHIA
 503 predictions with model uncertainties. To propagate the model uncertainty on the result, the
 504 results of the unfolding are compared using a response matrix estimated by varying the MAD-
 505 GRAPH prediction up and down its model uncertainty.

506 8 Systematic Uncertainties

507 The measurement of the Drell-Yan $p_T^{\mu\mu}$ and the rapidity separation between the forward Drell-
 508 Yan and the leading jet is performed in bins of the dimuon mass in the range 30–1500 GeV.
 509 Systematic uncertainties due to luminosity, pileup and QED FSR effects cancel out or are neg-
 510 ligible when normalized to the cross section in the Z boson mass region (60–120 GeV).
 511 For all uncertainty sources the effect directly translates into an uncertainty in the cross section
 512 measurement. The systematic uncertainties are summarized in Tab. 6 and Tab. 7.

513 The main sources of systematic uncertainties affecting the Drell-Yan and Drell-Yan +jet cross
 514 section measurement are:

- 515 • Jet Energy Scale and Jet Energy Resolution

516 The jet energy correction with respect to the JES and JER are known with a lim-
 517 ited precision. Thus, the jet energy correction can influence the fraction of selected
 518 events in the fiducial region with $p_T^{\text{jet}} > 30 \text{ GeV}$ and $|\eta^{\text{jet}}| < 4.5$. The correction of the
 519 jet energy leads into a systematic uncertainty on the cross section. An uncertainty
 520 between 3 – 5% on the jet energy scale is assigned depending on the transverse mo-
 521 mentum and the pseudorapidity of the jet [27]. The score resolution scaling factor
 522 (eq. (8)), which was defined as the ratio of data over MC resolution, was estimated
 523 with a precision of 5 – 15%, depending on the jet η [28]. The total uncertainty on the
 524 JEC and JER is obtained by varying the JEC and the scaling factor within the limits
 525 of uncertainty for the MC generator predictions. This directly translates into an un-
 526 certainty on the measured cross section by using the scaled MADGRAPH predictions
 527 for the unfolding matrix. The JEC and JER uncertainty is the dominant uncertainty
 528 source in the distributions including jets.

- 529 • Model uncertainty

530 To estimate an uncertainty on the model, a parametrisation of the data points is em-
 531 ployed. The parametrisation gives an estimate on how the shape of the distribution
 532 can vary within the statistical uncertainty of data. The parameters are given with
 533 an uncertainty taking into account the statistical uncertainty on the data. By chang-
 534 ing the fit parameters within their uncertainty, one can estimate to which extend the
 535 shape of the distribution can vary but still being consistent with data. The parametri-
 536 sation function is chosen in order to describe the data on detector level. In case of the
 537 dimuon $p_T^{\mu\mu}$ distribution, the low $p_T^{\mu\mu}$ region is parametrised by a Gaussian function
 538 and the $p_T^{\mu\mu}$ tail is parametrised by an exponential function. In case of the $|\Delta y(\mu\mu, j)|$
 539 distribution, the data is parametrised by a linear function. The uncertainty on the
 540 fit parameters are used to reweight the MADGRAPH +PYTHIA predictions, accord-
 541 ing an event weight defined as $\omega_{\text{model}} = \frac{p^\pm}{p^{\text{nominal}}} \cdot p^\pm$ indicates the parametrisation
 542 with varying the fit parameters up and down their uncertainties and p^{nominal} refers
 543 to the parametrisation with nominal fit parameters. The nominal predictions from
 544 MADGRAPH and the model uncertainty obtained from the reweighted results show
 545 good agreement to data. To propagate the model uncertainty on the cross section

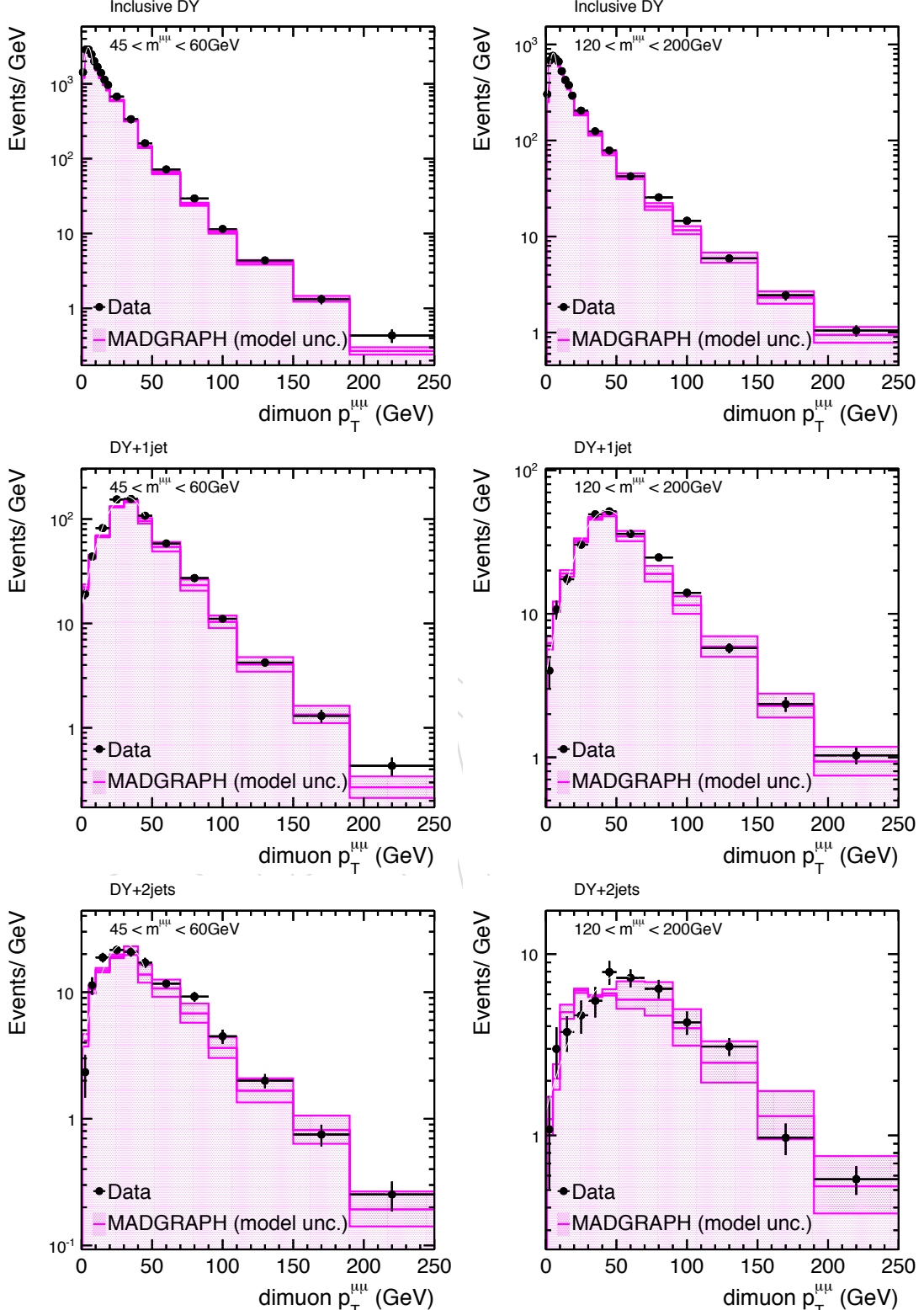


Figure 23: The $p_T^{\mu\mu}$ distribution for low and high invariant masses in the inclusive DY, DY + 1 jet, and DY + 2 jet topology. Data is compared to MADGRAPH + PYTHIA6 predictions plus a model uncertainty derived from the uncertainties on the data parametrisation.

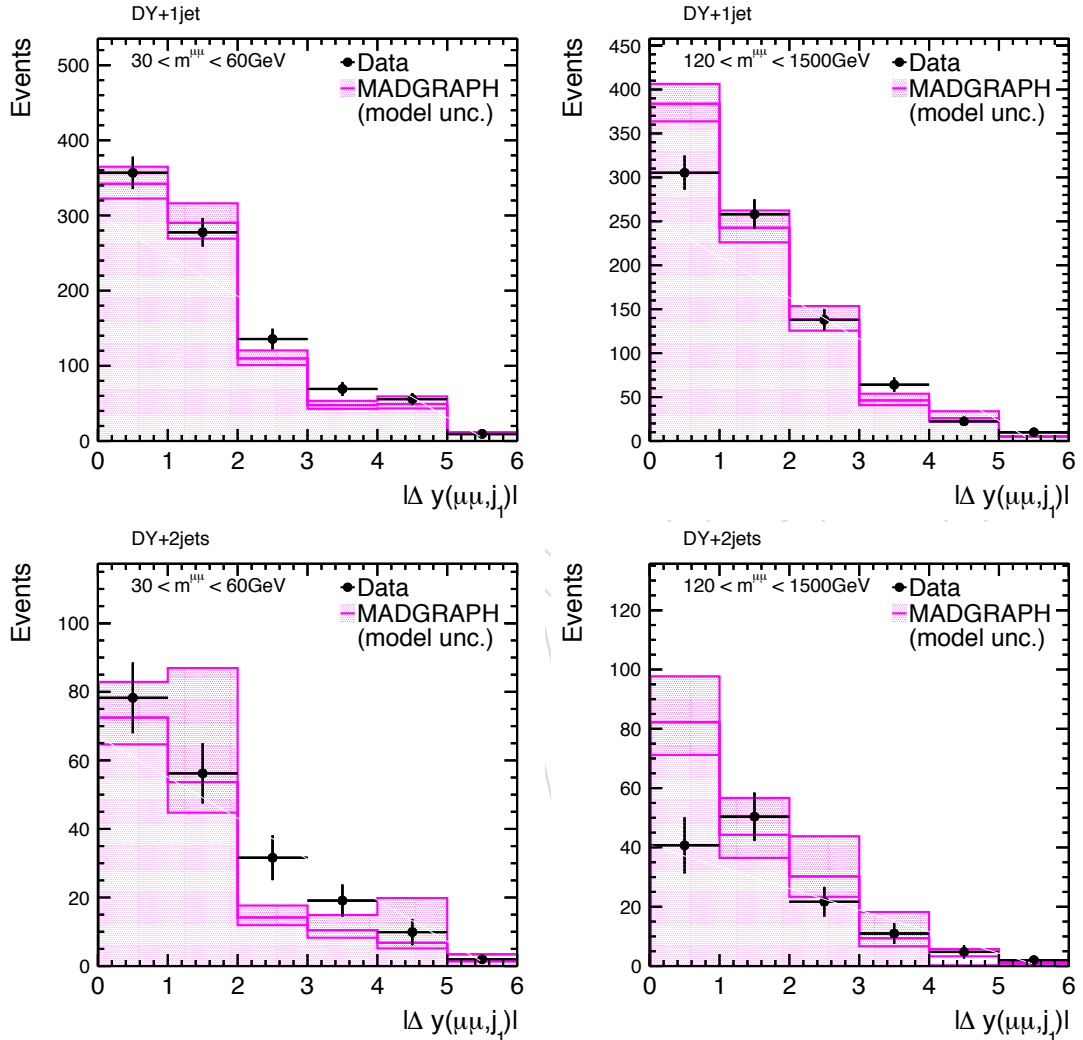


Figure 24: The $|\Delta y(\mu\mu, j_1)|$ distribution for low and high invariant masses in the DY + 1 jet and DY + 2 jet topology. Data is compared to MADGRAPH + PYTHIA6 predictions plus a model uncertainty derived from the uncertainties on the data parametrisation.

546 result, the results of the unfolding are compared using a response matrix estimated
 547 by varying the MADGRAPH prediction up and down its model uncertainty.

- 548 • Pileup reweighting procedure

549 The pileup distribution in data is estimated from the luminosity information and
 550 the inelastic proton proton cross section. The inelastic proton proton cross section
 551 is estimated with a precision of 5% by CMS [38]. The uncertainty on the inclusive
 552 cross section influences the pileup modelling in the data distribution and is taken
 553 into account in the analysis. The uncertainty is obtained by varying the inelastic
 554 cross section by $\pm 5\%$ around the nominal value.

- 555 • Efficiency correction

556 The muon isolation and identification efficiency as well as the trigger efficiency are
 557 estimated using the tag-and-probe method. The statistical and systematic uncer-
 558 tainties on the correction factors are propagated to the cross section. The uncertainty
 559 on the correction factor is estimated to be 2% [33] for muons with $p_T < 100$ GeV.
 560 The uncertainty for muons with $p_T > 100$ GeV, is estimated by the extrapolation
 561 of correction factors from low to high muon p_T in using the total correction factor
 562 calculated at low p_T , adding a systematic uncertainty of the order of 3% for the ex-
 563 trapulation to high p_T [39]. The efficiency correction factors are changed within their
 564 uncertainty to estimate an uncertainty on the cross section.

- 565 • Background estimation

566 The final results show the background-subtracted data yields. Therefore, the uncer-
 567 tainty due to the estimation of the background process is assigned. This uncertainty
 568 includes the statistical uncertainty in the number of events in the background pro-
 569 cesses as well as an uncertainty to take into account the shape and normalisation of
 570 the background contribution.

571 The uncertainty due to the limited number of simulated events is assigned by vary-
 572 ing the number of background events by $\pm \sqrt{N_i}$, where N_i is the number of MC
 573 events in bin i .

574 The uncertainty on the normalisation and background estimation depends on the
 575 background process. An uncertainty on the QCD background estimation is assigned
 576 to the ratio calculation of opposite-sign over same-sign data events by varying the
 577 anti-isolation requirement. The uncertainty on the ratio is estimated to be 8%. The
 578 $t\bar{t}$ background normalisation is taken from CMS measurement and an uncertainty of
 579 8% is assigned [32]. Additionally, an uncertainty on the $t\bar{t}$ correction factor, to take
 580 into account differences between data and simulation, is assigned to be 10% [33]. The
 581 yields of diboson production are scaled to NLO theory predictions [34, 35] and an
 582 uncertainty of 30% is assigned on the normalisation. The single W background is es-
 583 timated by and normalised to the inclusive cross section as measured by CMS [36].
 584 The uncertainty is driven by limited MC statistics of the selected $W +$ jets events.
 585 The uncertainty in $Z \rightarrow \tau\tau$ normalisation, estimated from the CMS measurement, is
 586 4% [36].

587 The total systematic uncertainty due to the estimation of different background pro-
 588 cesses and limitations in statistics is obtained by varying the number of background
 589 events within the systematic uncertainty of the shape and normalisation, and by
 590 $\pm \sqrt{N_i}$ in the event bin i .

Table 6: Summary of typical systematic uncertainties of the Drell-Yan di-muon transverse momentum in different bins of the di-muon mass. The total systematic uncertainties are given by the quadratic sum of each individual sources. The first values are for inclusive Drell-Yan production, the second ones for DY + 1 jet and the third ones for DY + 2 jet production.

| $m^{\mu\mu}$ bin (GeV) | JEC & JER (%) | | | Model (%) | | | PU (%) | | | Eff. (%) | | | Bkg Est. (%) | | |
|------------------------|---------------|---|----|-----------|-----|-----|--------|-----|-----|----------|-----|-----|--------------|-----|-----|
| 30 - 45 | - | 6 | 8 | 0.1 | 1 | 2 | 0.5 | 1 | 2 | 0.5 | 1 | 1 | 0.5 | 1 | 3 |
| 45 - 60 | - | 6 | 6 | 0.1 | 1 | 2 | 0.3 | 1 | 1 | 1 | 1 | 2 | 0.5 | 1 | 2 |
| 60 - 120 | - | 6 | 4 | 0.1 | 0.1 | 0.5 | 0.1 | 0.1 | 0.1 | 0.1 | 0.1 | 0.5 | 0.1 | 0.1 | 0.1 |
| 120 - 200 | - | 7 | 9 | 0.5 | 1 | 3 | 0.5 | 1 | 1 | 0.5 | 2 | 4 | 0.5 | 2 | 6 |
| 200 - 1500 | - | 7 | 13 | 2 | 2 | 7 | 1 | 1 | 4 | 2 | 4 | 8 | 2 | 3 | 8 |

Table 7: Summary of typical systematic uncertainties of $|\Delta y(\mu\mu, j_1)|$ distribution in DY + 1 jet (DY + 2 jets) events in different bins of the di-muon mass. The total systematic uncertainties are given by the quadratic sum of each individual sources.

| $m^{\mu\mu}$ bin (GeV) | JEC & JER (%) | | | Model (%) | | PU (%) | | Eff. (%) | | Bkg Est. (%) | |
|------------------------|---------------|----|--|-----------|-----|--------|---|----------|-----|--------------|-----|
| 30 - 60 | 20 | 12 | | 4 | 10 | 2 | 2 | 1 | 1 | 1 | 1 |
| 60 - 120 | 5 | 2 | | 0.5 | 0.5 | 1 | 1 | 0.1 | 0.1 | 0.1 | 0.5 |
| 120 - 1500 | 5 | 7 | | 1 | 5 | 1 | 1 | 2 | 2 | 1 | 2 |

9 Theory Uncertainty

The choice of the factorisation and renormalisation scale influences the theory prediction. The theory uncertainties are determined with the MC generator POWHEG. The uncertainties on the scale choices are obtained by reweighting the events in the POWHEG MiNLO production of Z + 1 jet [40] at NLO. The weight corresponds to different choices of scales. The central value of the factorisation and renormalisation scales are varied by a factor of two above and below. Small uncertainties due to the renormalisation and factorisation scale variation are observed at low $p_T^{\mu\mu}$. The uncertainties increase with increasing $p_T^{\mu\mu}$ and are largest for inclusive DY production around 25%. In the cases of DY + 1 and DY + 2 production the uncertainty decreases and is around 10% at high $p_T^{\mu\mu}$. In the $|\Delta y(\mu\mu, j)|$ distribution the scale variation of μ_R and μ_F have a small effect of 10% on the differential cross section at small rapidity differences. Changing μ_R and μ_F a maximal uncertainty of $\sim 30\%$ is observed at large rapidity differences.

The impact of the PDF uncertainty on the measurement is estimated in the Z invariant mass range by POWHEG MiNLO production of Z + 2 jet [40] at NLO. As central PDF set the HERAPDF1.5LO and the PYTHIA tune CUETP6S1 [41] was used. The uncertainty on the predicted di-muon p_T cross section is small at low p_T and increases up to 5% for high di-muon p_T . In case of the absolute rapidity separation the uncertainty is between 1 - 5%, with increasing uncertainty at the high rapidity separation.

10 Drell-Yan Cross Section measurement

The cross sections for inclusive Drell-Yan production, as well as for DY + 1 jet and DY + 2 jet production are given below, unfolded to stable particle level for Drell-Yan production in the phase space defined by $p_T^{\text{lead}\mu} > 20 \text{ GeV}$, $p_T^{\text{sublead}\mu} > 10 \text{ GeV}$ and $|\eta^\mu| < 2.1$. Jets are reconstructed with the anti- k_T algorithm using $R = 0.5$ with $|\eta| < 4.5$ and $p_T > 30 \text{ GeV}$. The cross

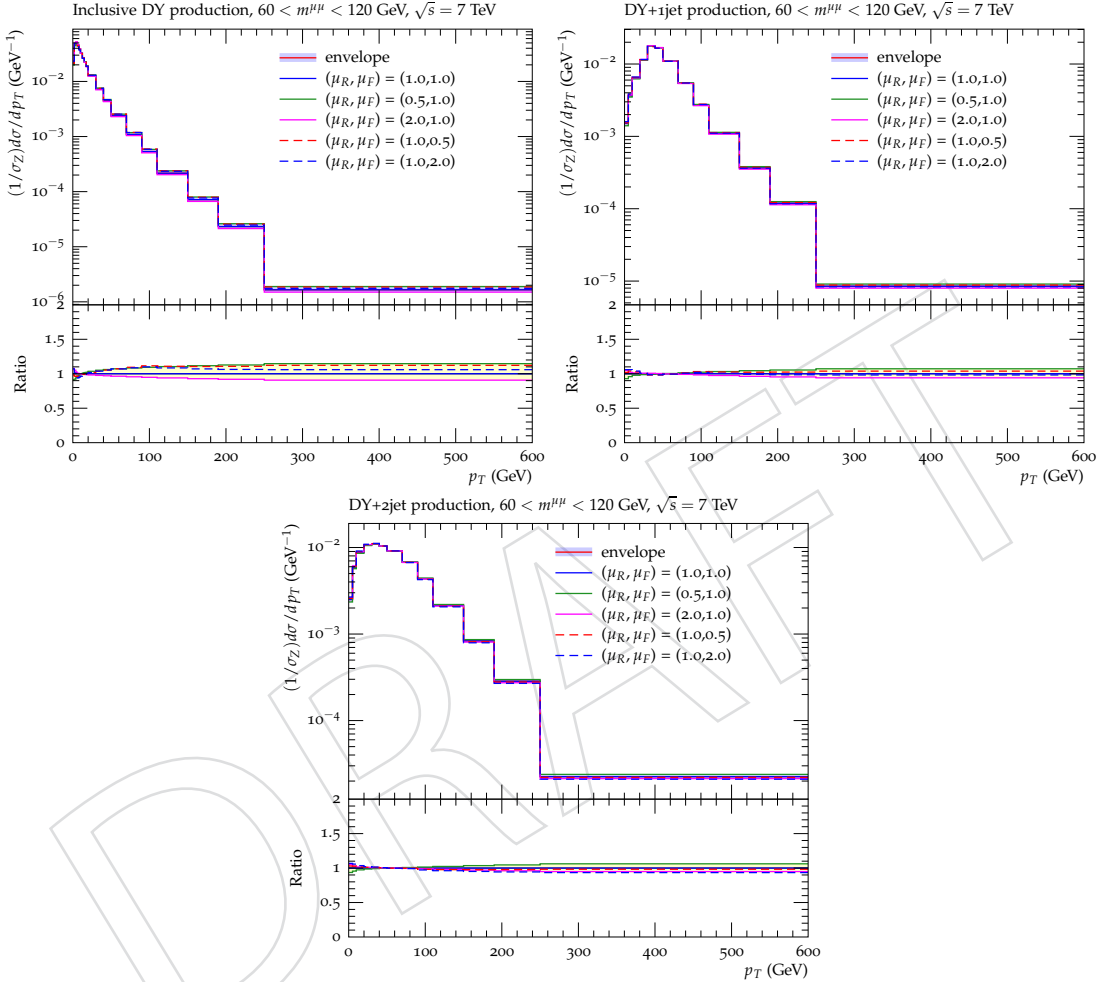


Figure 25: The renormalisation and factorization scale variation by a factor of two above and below the central value. The envelope of all predictions is shown as a band. The dimuon $p_T^{\mu\mu}$ distribution is shown for the inclusive DY, DY + 1 jet and DY + 2 jets production in the Z invariant mass range.

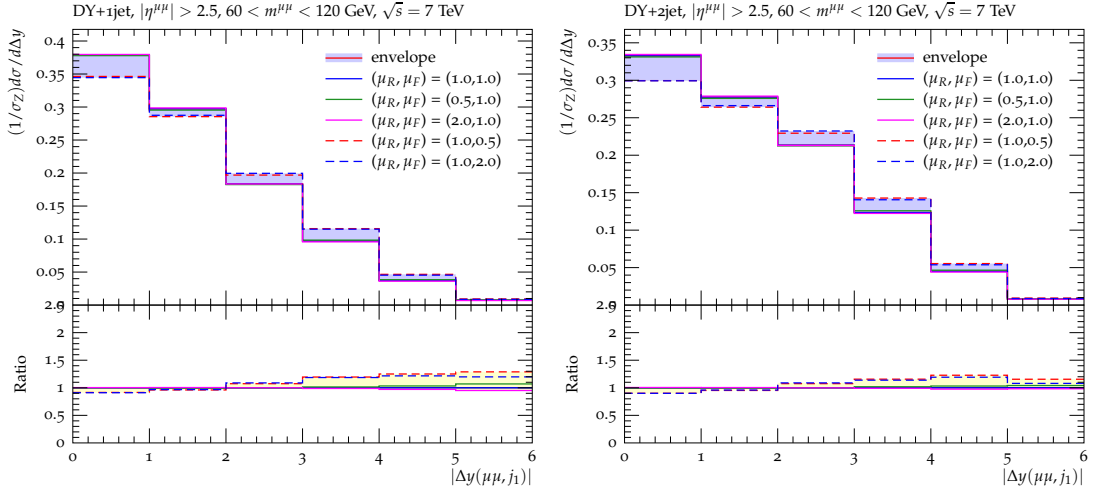


Figure 26: The renormalisation and factorization scale variation by a factor of two above and below the central value. The envelope of all predictions is shown as a band. The $|\Delta y(\mu\mu, j_1)|$ distribution is shown for the DY + 1 jet and DY + 2 jets production in the Z invariant mass range.

sections presented are normalized to the cross section in the Z peak region (60–120 GeV). In all distributions the data points are shown at the center of the bin and no bin-center correction is applied.

10.1 Inclusive Drell-Yan differential Cross Section measurement as a function of the dimuon transverse momentum

The normalised cross section as a function of the di-muon p_T is presented in Fig. (29), (30) and (31) for inclusive DY, DY + 1 jet, and DY + 2 jets production respectively. The data are compared to theory predictions estimated by various MC generators corresponding to different calculations at fixed-order implemented with parton shower and hadronisation. The p_T distribution is shown in five invariant mass ranges: 30 – 45, 45 – 60, 60 – 120, 120 – 200, and 200 – 1500 GeV.

The systematic uncertainties increase from the inclusive sample to DY + jets due to the JEC uncertainty.

The di-muon $p_T^{\mu\mu}$ distribution for inclusive DY lepton pair production is rising from small $p_T^{\mu\mu}$ towards a maximum at around 5 GeV and then falling towards large $p_T^{\mu\mu}$. The rising behavior at small $p_T^{\mu\mu}$ is described by soft gluon resummation, and is treated in the simulation by initial state parton showers. The distribution is well described by the higher order predictions from MADGRAPH + PYTHIA 6 and POWHEG + PYTHIA 6. A similar behavior is observed for the DY + 1 jet and DY + 2 jets distributions, however, the maximum is shifted to larger values. The maximum is around 30 GeV, which is the p_T threshold for the jets. The differences between the various theory predictions can be investigated in more detail, by enlarging the phase space at small di-muon p_T , by requiring additional jets in the event. In the case of the DY + 1 jet topology, the region of low di-muon p_T is sensitive to multiple parton emissions. In the simulation of PYTHIA without initial state parton shower a sharp drop of the cross section below 30 GeV is observed (not shown here). However, in order to describe the rise at low p_T , higher order calculations are needed in terms of multi parton emissions calculated at fixed order. The comparison to data is improved when comparing to POWHEG, which generated Z+2 partons at

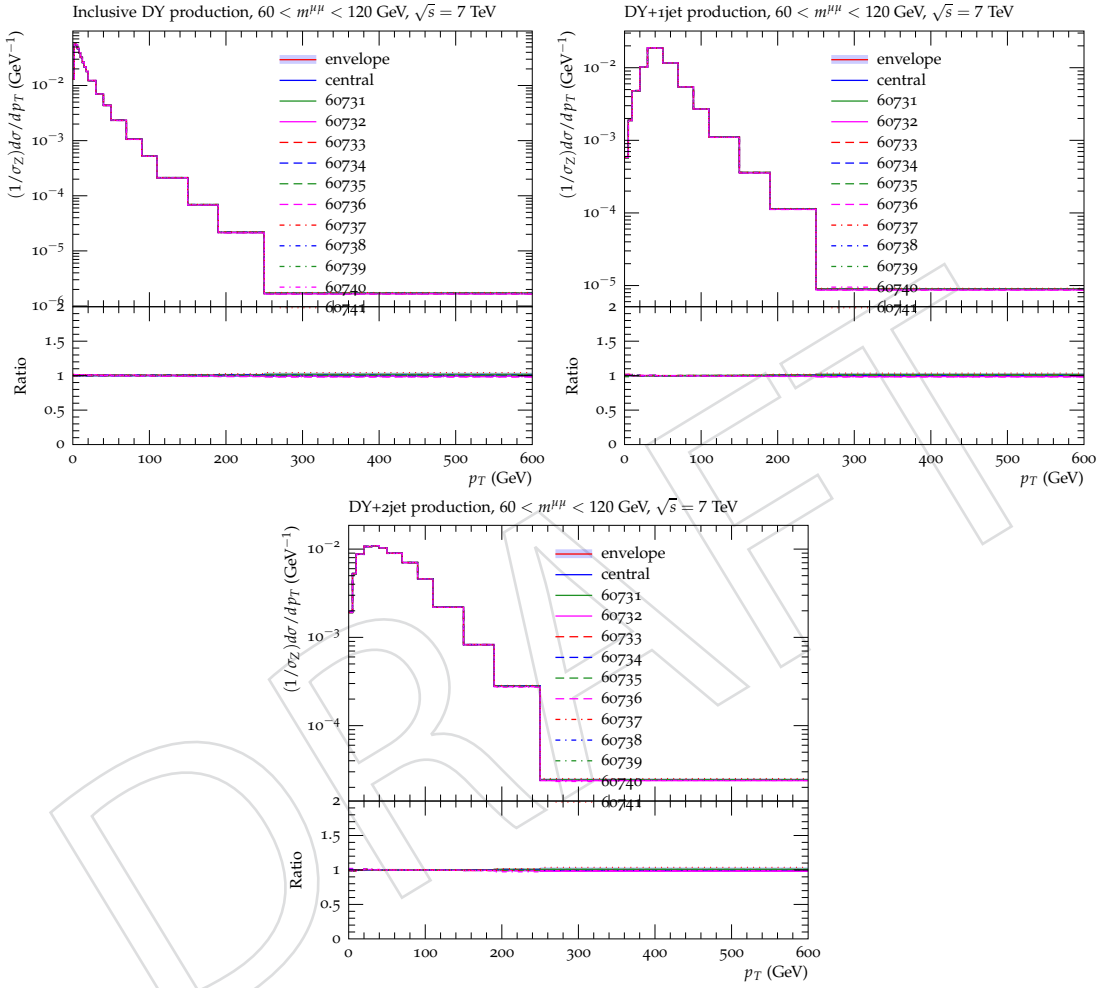


Figure 27: The impact of the PDF uncertainty is shown with the central value. The envelope of all predictions is shown as a band. The dimuon $p_T^{\mu\mu}$ distribution is shown for the inclusive DY, DY + 1 jet and DY + 2 jets production in the Z invariant mass range.

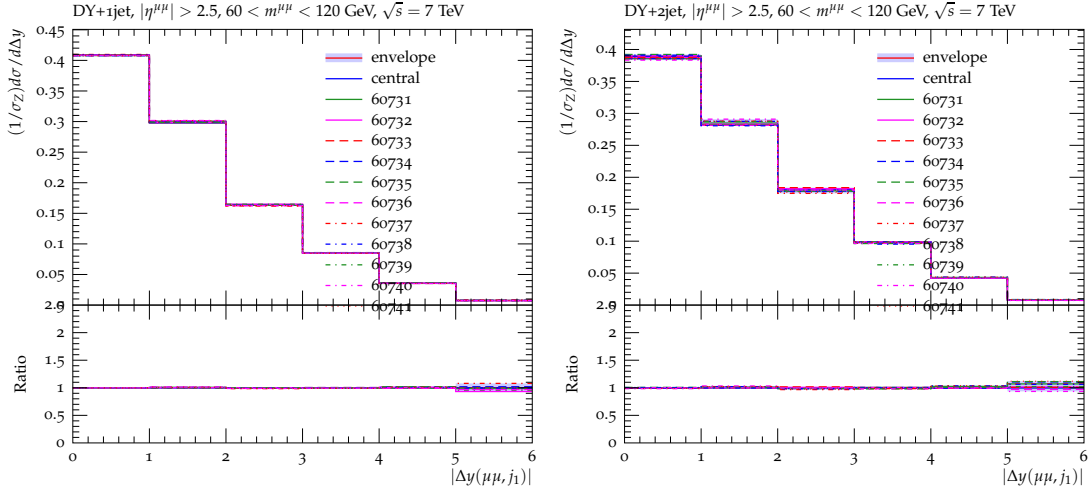


Figure 28: The impact of the PDF uncertainty is shown with the central value. The envelope of all predictions is shown as a band. The $|\Delta y(\mu\mu, j)|$ distribution is shown for the DY + 1 jet and DY + 2 jets production in the Z invariant mass range.

NLO. The agreement to data is best for MADGRAPH, which generates at most four additional partons in the perturbative calculation at LO. Therefore, the region at low di-moun p_T in DY+jet topologies is described by soft-gluon emissions, simulated by the parton shower algorithm, as well as multi-parton emissions, calculated from the hard parton cross section. Similar results are observed for DY + 2 jets production. The region at small p_T shows more low p_T Drell-Yan pairs compared to DY + 1 jet. This can be explained by the fact that the two jets balance each other in the transverse plane and the Drell-Yan pair is balanced by softer parton emissions.

10.2 Drell-Yan Cross Section measurement as a function of the rapidity difference between the Drell-Yan pair and the leading jet

The differential cross section $\frac{d^2\sigma}{dm d|\Delta y(\mu\mu, j)|}$ is presented for the production of DY + 1 jet and DY + 2 jets. The cross section is measured in the three mass bins 30–60 GeV, 60–120 GeV and 120–1500 GeV. The Drell-Yan pair is required to fulfill $|\eta| > 2.5$. All cross sections are normalized to the Z boson mass region (60–120 GeV).

The normalized cross section is presented in Fig. (32) for the production of DY + 1 jet and in Fig. (33) for DY + 2 jets.

The measured cross section is compared to different MC predictions. In the Z invariant mass region predictions from CASCADE are included. In the low invariant mass region the MC predictions are not able to reproduce the measured cross section as a function of $|\Delta y(\mu\mu, j)|$. The MC calculations predict a too low cross section. The predictions of MADGRAPH + PYTHIA 6 are within the statistical and systematic uncertainties of data. The predictions of POWHEG (Z + 2jets) at NLO underestimate the data at low masses, but PYTHIA 6 is even further off.

In the Z resonance region POWHEG + PYTHIA 6 reveals similar results than obtained from MADGRAPH + PYTHIA 6. Moreover, the LO and first order calculations of PYTHIA 6 fail to describe the large $|\Delta y(\mu\mu, j)|$ region. In the bin of $1 < |\Delta y(\mu\mu, j)| < 2$, the cross section value is nicely described by all MC predictions. CASCADE shows a good agreement to data for $|\Delta y(\mu\mu, j)| < 3$. At large rapidity differences CASCADE underestimated the data around 10 – 30%. In the high invariant mass region for DY + 1 jet production, the MC over data ratio shows a trend towards smaller $|\Delta y(\mu\mu, j)|$. All MC predictions overestimate the cross section at low $|\Delta y(\mu\mu, j)|$ and

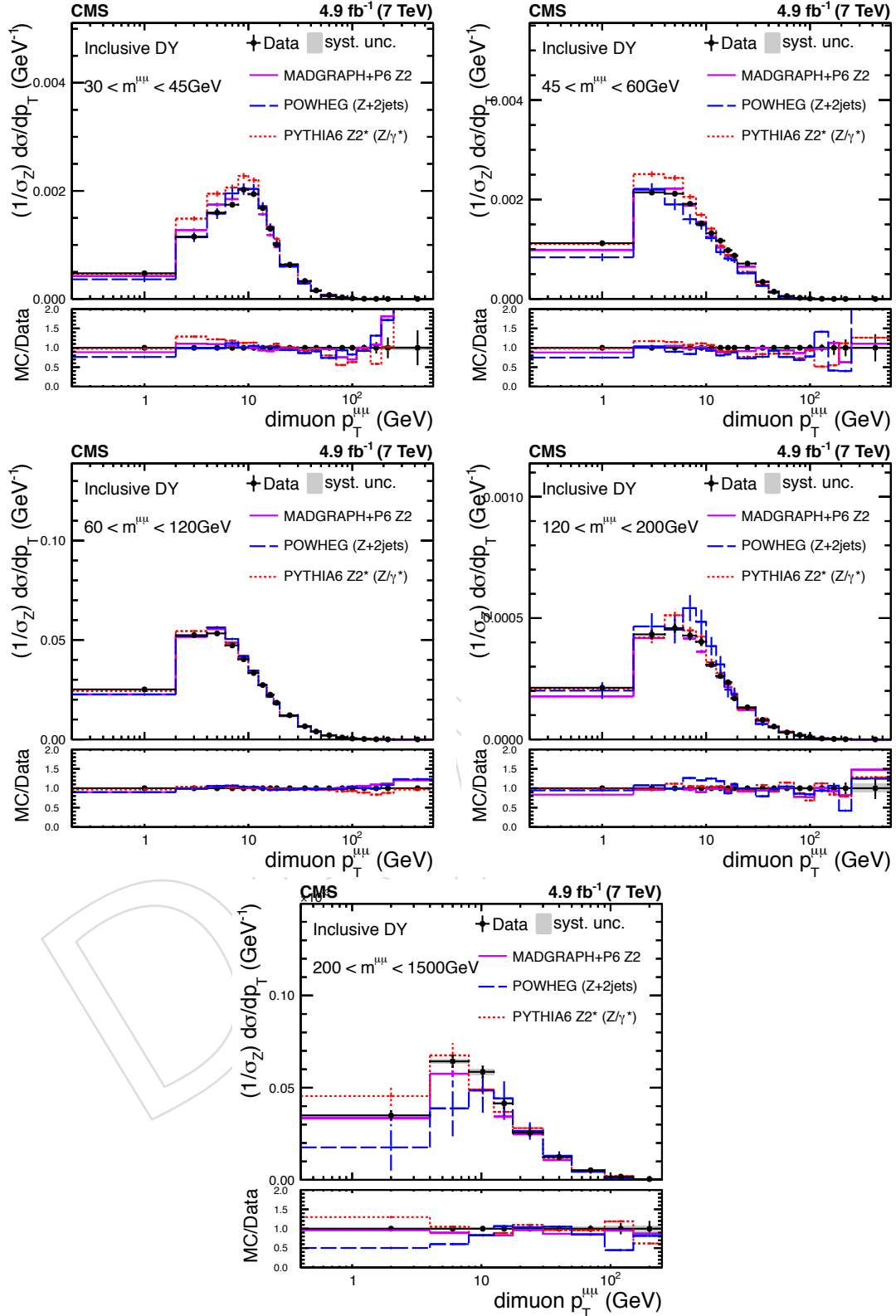


Figure 29: Drell-Yan dimuon transverse momentum distribution normalized to the Z resonance region in five different invariant mass regions covering the range from 30-1500 GeV. The vertical error bars on data indicate the statistical uncertainties and the error band represent the correlated systematic uncertainties.

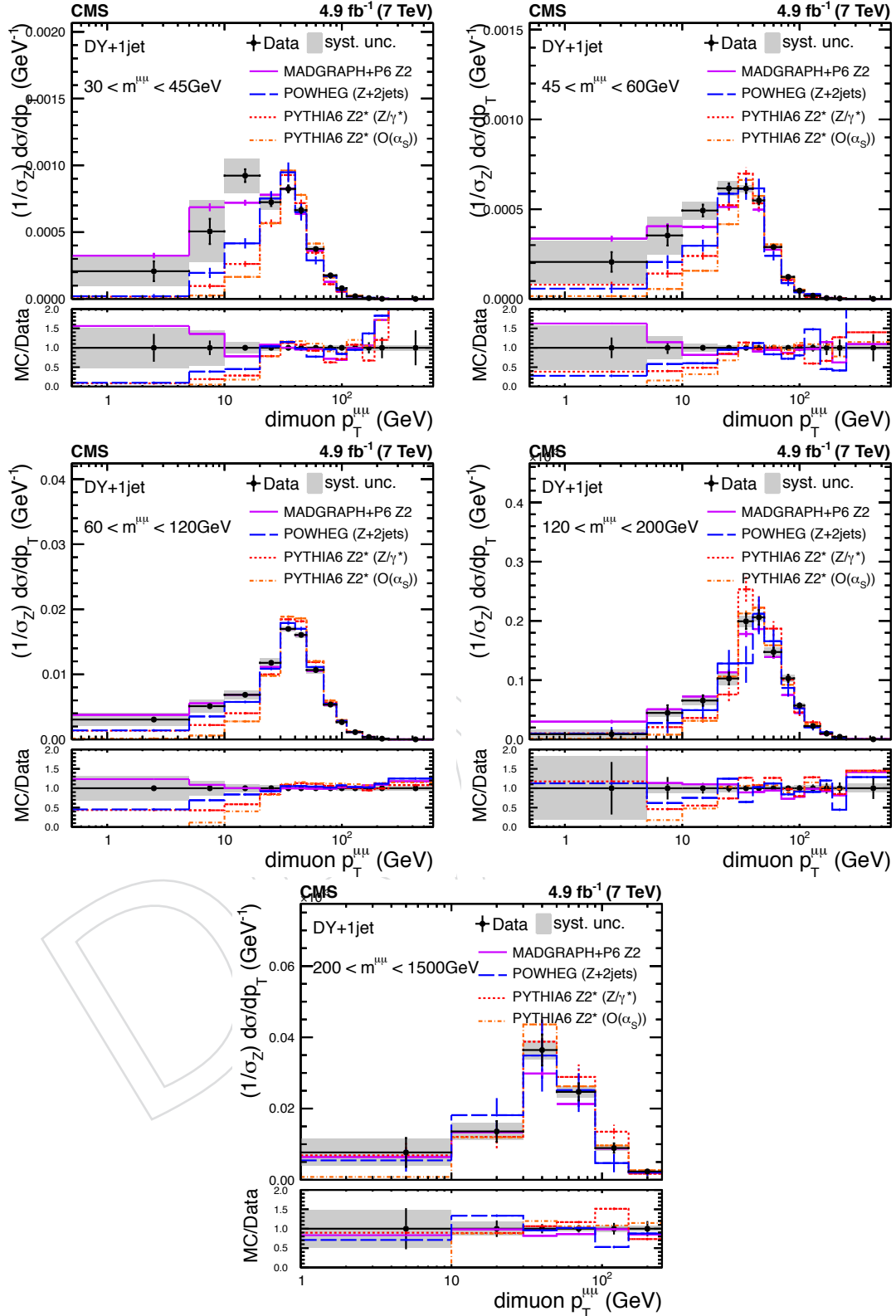


Figure 30: Drell-Yan + 1 jet dimuon transverse momentum distribution normalized to the Z resonance region in five different invariant mass regions covering the range from 30-1500 GeV. The vertical error bars on data indicate the statistical uncertainties and the error band represent the correlated systematic uncertainties.

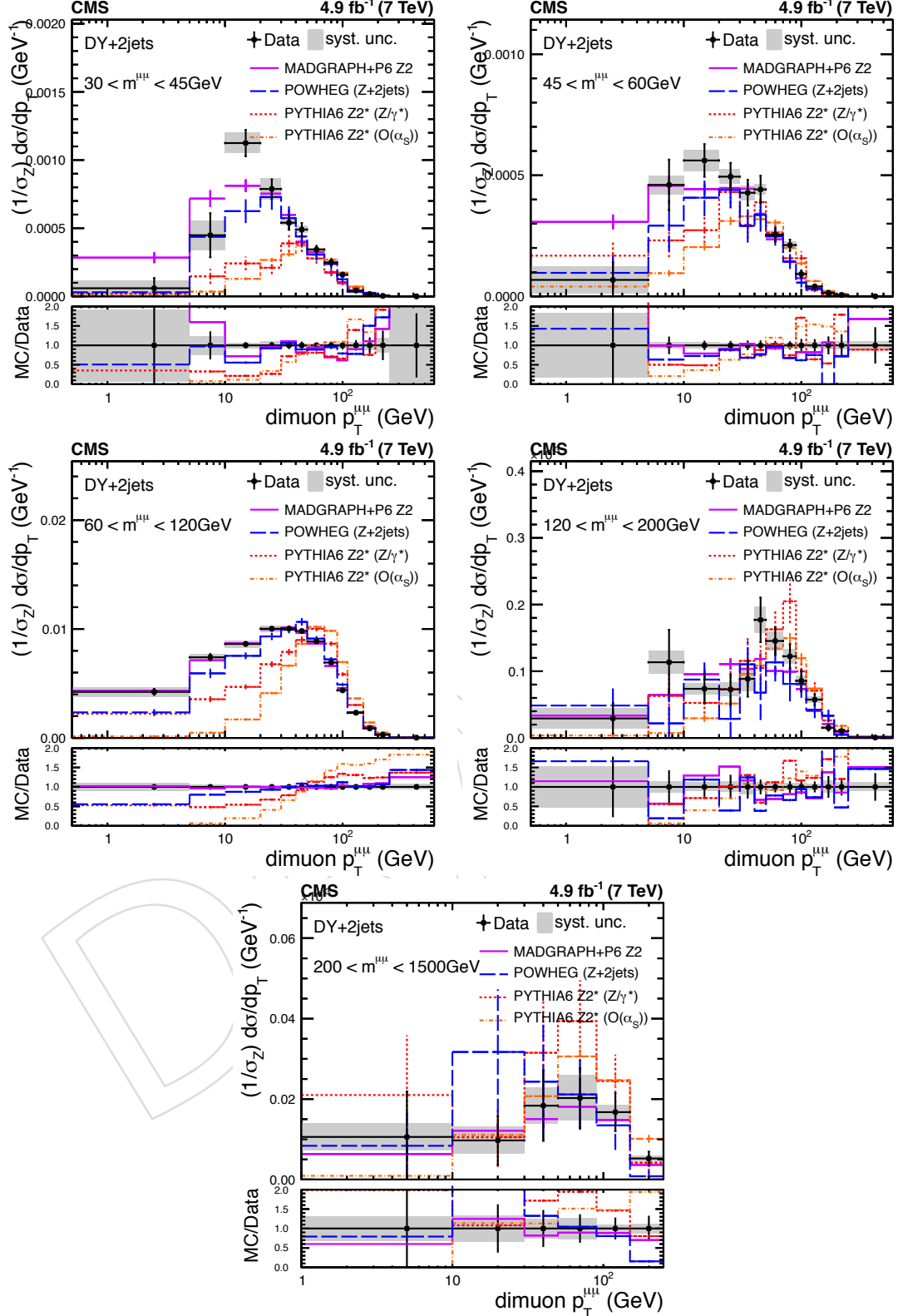


Figure 31: Drell-Yan + 2 jets dimuon transverse momentum distribution normalized to the Z resonance region in five different invariant mass regions covering the range from 30-1500GeV. The vertical error bars on data indicate the statistical uncertainties and the error band represent the correlated systematic uncertainties.

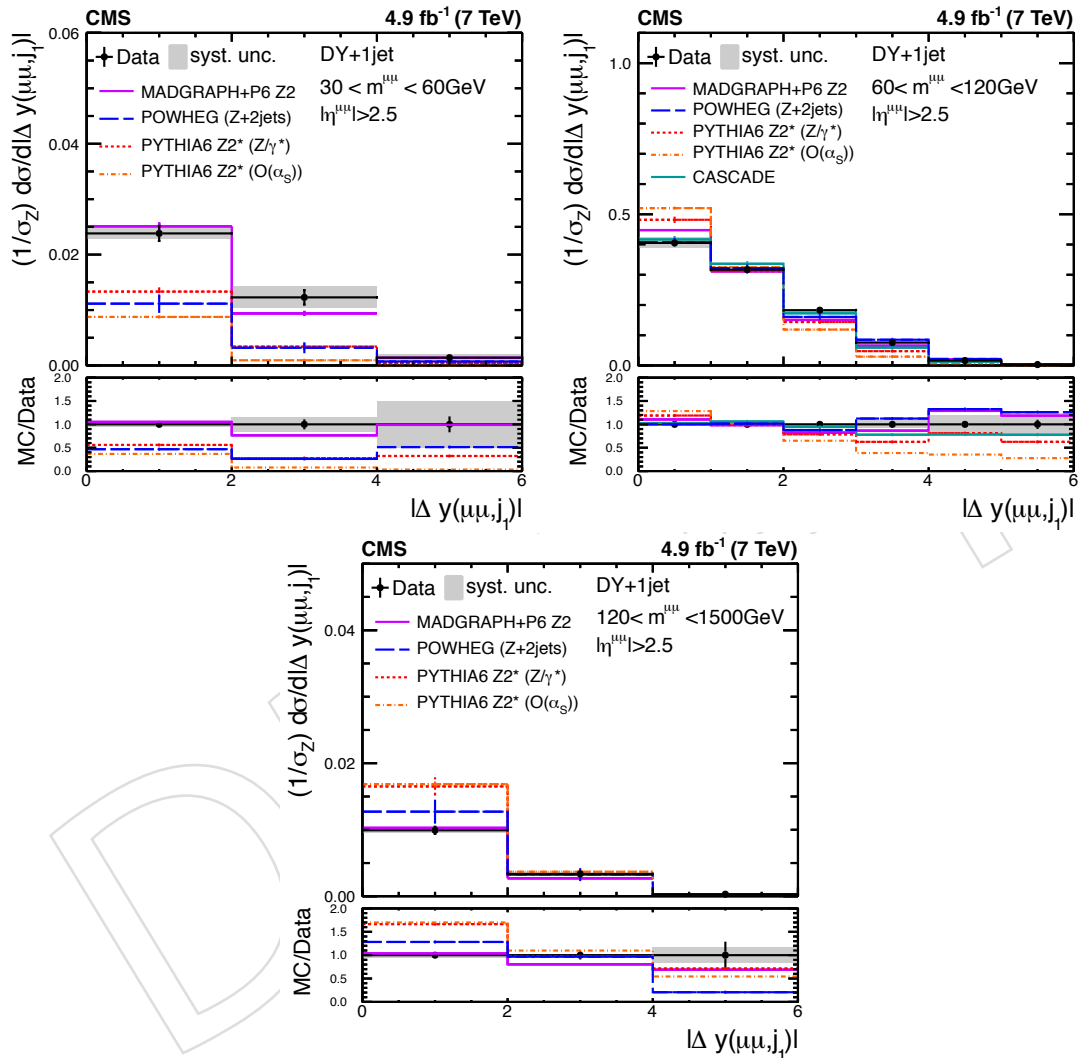


Figure 32: Drell-Yan dimuon rapidity difference between the Drell-Yan and the leading jet normalized to the Z resonance region.

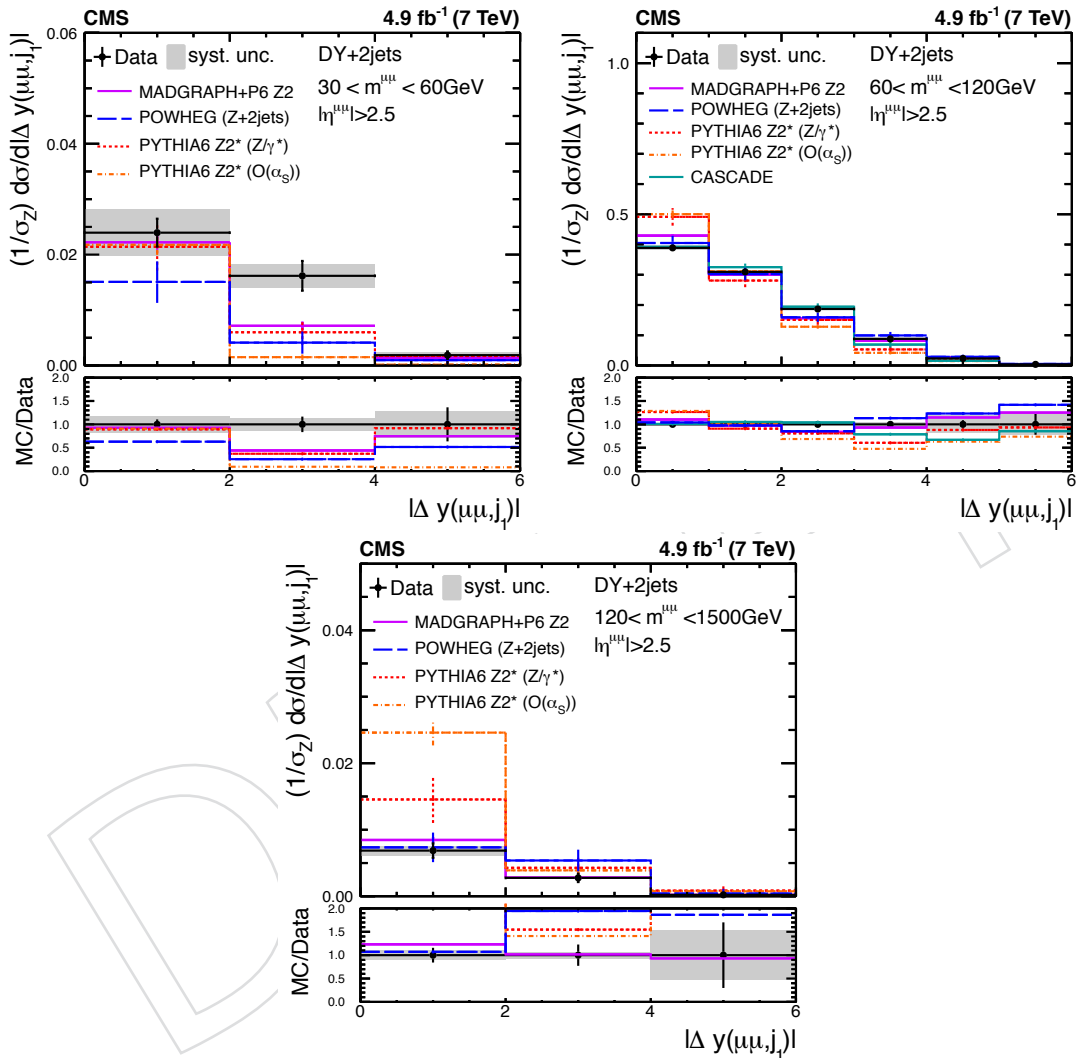


Figure 33: Drell-Yan dimuon rapidity difference between the Drell-Yan and the leading jet normalized to the Z resonance region.

underestimate the data at large $|\Delta y(\mu\mu, j)|$. In the case of DY + 2 jets production only MADGRAPH is able to reproduce the data. The other MC simulations predict too high values for $120 < m_{\mu\mu} < 1500$ GeV.

10.3 Jet multiplicity in Drell-Yan + jet events

The average jet multiplicity of jets with $p_T > 30$ GeV between the leading jet and the forward Drell-Yan production as a function of the rapidity separation $|\Delta y(\mu\mu, j)|$ is presented in Fig. (34). Due to the limited number of recorded events the cross section is only shown in the Z boson mass range (60–120 GeV). The measured jet multiplicity is compared to MC simulation accounting for different theoretical calculations at LO and NLO plus collinear resummation. The average jet multiplicity increases with increasing separation between the DY lepton pair and the leading jet from 0 to 0.3 at large rapidity separation. The general behavior is reproduced by the MADGRAPH and POWHEG simulation, while the lowest order predictions from PYTHIA 6 fail to describe the rise of the jet multiplicity. CASCADE overestimated the jet multiplicity at high rapidity separation.

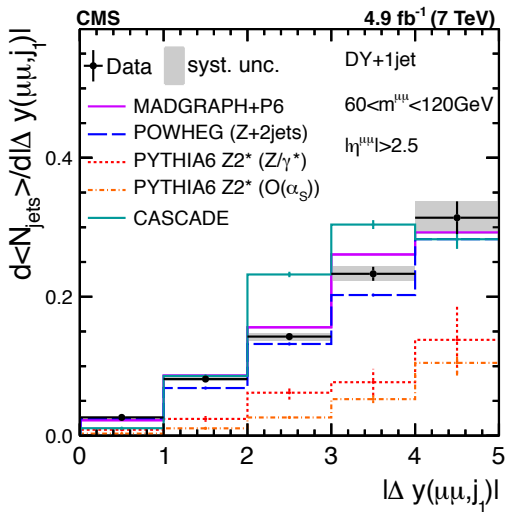


Figure 34: Average number of jets in forward Drell-Yan production as a function of the rapidity separation between the Drell-Yan and the leading jet. The measured cross section is compared to the MADGRAPH MC predictions.

11 Conclusions

The first measurement of the differential Drell-Yan and associated jets cross section as a function of the Drell-Yan mass is presented using an integrated luminosity of 4.9 fb^{-1} . The measurement is performed differentially as a function of the Drell-Yan transverse momentum for various di-muon mass ranges within 30–1500 GeV. The rapidity separation between the Drell-Yan muon pair and the leading jet is measured for different Drell-Yan mass bins and the jet multiplicity as a function of Δy is presented for the Z mass region. The measured cross sections are corrected to stable-particle level. The measured cross sections are compared to MADGRAPH $Z/\gamma^* \rightarrow \mu\mu$ predictions.

The measured p_T spectrum of DY lepton pair production is reasonably well described by the MADGRAPH simulation. The rise at small p_T in inclusive DY lepton pair production is a measure of soft gluon resummation, while the behavior at $p_T < 30$ GeV in DY + jet production is a

695 direct signal for perturbative jet resummation, which is well reproduced by initial state parton
696 showers. The rapidity difference between DY lepton pair and the leading jet is not reproduced
697 by the simulation and MADGRAPH predicts the jets to be closer to the DY lepton pair than ob-
698 served in the data. The average jet multiplicity in the rapidity interval between the DY lepton
699 pair and the leading jet is increasing with increasing separation, but the simulation predicts
700 more jets.

701 References

- 702 [1] R. Hamberg, W. L. van Neerven, and T. Matsuura, “A complete calculation of the order
703 α_s^2 correction to the Drell–Yan K-factor”, *Nucl. Phys. B* **359** (1991) 343,
704 doi:10.1016/0550-3213(91)90064-5.
- 705 [2] S. Catani, L. Cieri, G. Ferrera et al., “Vector Boson Production at Hadron Colliders: A
706 Fully Exclusive QCD Calculation at Next-to-Next-to-Leading Order ”, *Phys. Rev. Lett.*
707 **103** (2009) 082001, doi:10.1103/PhysRevLett.103.082001, arXiv:0903.2120.
- 708 [3] S. Catani and M. Grazzini, “Next-to-Next-to-Leading-Order Subtraction Formalism in
709 Hadron Collisions and its Application to Higgs-Boson Production at the Large Hadron
710 Collider ”, *Phys. Rev. Lett.* **98** (2007) 222002,
711 doi:10.1103/PhysRevLett.98.222002, arXiv:hep-ph/0703012.
- 712 [4] K. Melnikov and F. Petriello, “Electroweak gauge boson production at hadron colliders
713 through $O(\alpha_s^2)$ ”, *Phys. Rev. D* **74** (2006) 114017, doi:10.1103/PhysRevD.74.114017,
714 arXiv:hep-ph/0609070.
- 715 [5] Y. L. Dokshitzer, D. Diakonov, and S. I. Troian, “On the Transverse Momentum
716 Distribution of Massive Lepton Pairs”, *Phys. Lett.* **B79** (1978) 269–272,
717 doi:10.1016/0370-2693(78)90240-X.
- 718 [6] J. C. Collins, D. E. Soper, and G. F. Sterman, “Transverse Momentum Distribution in
719 Drell-Yan Pair and W and Z Boson Production”, *Nucl.Phys.* **B250** (1985) 199,
720 doi:10.1016/0550-3213(85)90479-1.
- 721 [7] CMS Collaboration, “Measurement of the Rapidity and Transverse Momentum
722 Distributions of Z Bosons in pp Collisions at $\sqrt{s} = 7$ TeV”, *Phys.Rev.* **D85** (2012) 032002,
723 doi:10.1103/PhysRevD.85.032002, arXiv:1110.4973.
- 724 [8] J. R. Andersen, V. Del Duca, F. Maltoni et al., “W boson production with associated jets at
725 large rapidities”, *JHEP* **05** (2001) 048, arXiv:hep-ph/0105146.
- 726 [9] P. Cipriano, S. Dooling, A. Grebenyuk et al., “Higgs boson as a gluon trigger”, *Phys. Rev.*
727 **D 88** (Nov, 2013) 097501, doi:10.1103/PhysRevD.88.097501.
- 728 [10] M. Cacciari and G. P. Salam, “Dispelling the N^3 myth for the k_t jet-finder”, *Phys.Lett. B*
729 **641** (2006) 57–61, doi:10.1016/j.physletb.2006.08.037,
730 arXiv:hep-ph/0512210.
- 731 [11] M. Cacciari, G. P. Salam, and G. Soyez, “The anti- k_t jet clustering algorithm”, *JHEP* **04**
732 (2008) 063, doi:10.1088/1126-6708/2008/04/063, arXiv:0802.1189.
- 733 [12] M. Cacciari, G. P. Salam, and G. Soyez, “FastJet User Manual”, *Eur.Phys.J. C* **72** (2012)
734 1896, doi:10.1140/epjc/s10052-012-1896-2, arXiv:1111.6097.

- [13] CMS Collaboration, “Performance of CMS muon reconstruction in pp collision events at $\sqrt{s} = 7 \text{ TeV}$ ”, *JINST* **7** (2012) P10002, doi:10.1088/1748-0221/7/10/P10002, arXiv:1206.4071.
- [14] CMS Collaboration, “Determination of the Jet Energy Scale in CMS with pp Collisions at $\sqrt{s} = 7 \text{ TeV}$ ”, *CMS Physics Analysis Summary CMS-PAS-JME-10-010* (2010).
- [15] CMS Collaboration, “The CMS experiment at the CERN LHC”, *JINST* **3** (2008) S08004, doi:10.1088/1748-0221/3/08/S08004.
- [16] F. Maltoni and T. Stelzer, “MadEvent: Automatic event generation with MadGraph”, *JHEP* **0302:027** (2003).
- [17] T. Sjöstrand, S. Mrenna, and P. Skands, “PYTHIA 6.4 Physics and Manual”, *JHEP* **0605:026** (2006).
- [18] GEANT4 Collaboration, “GEANT4—a simulation toolkit”, *Nucl. Instrum. Meth. A* **506** (2003) 250, doi:10.1016/S0168-9002(03)01368-8.
- [19] R. Chierici et al., “Standard Model Cross Sections for CMS at 7 TeV”, <https://twiki.cern.ch/twiki/bin/viewauth/CMS/StandardModelCrossSections>.
- [20] W. Erdmann, “Offline Primary Vertex Reconstruction with Deterministic Annealing Clustering”, *CMS IN -2011/014* (2011). CMS Internal Note.
- [21] CMS Collaboration, “Tracking and Primary Vertex Results in First 7 TeV Collisions”, *CMS Physics Analysis Summary CMS-PAS-TRK-10-005* (2010).
- [22] http://home.fnal.gov/~cplager/log/1007/log.html#100729_Idea_for_Pileup_Estimation.
- [23] CMS Collaboration, “Particle–Flow Event Reconstruction in CMS and Performance for Jets, Taus, and E_T^{miss} ”, *CMS Physics Analysis Summary CMS-PAS-PFT-09-001* (2009).
- [24] CMS Collaboration, “Commissioning of the Particle-Flow Reconstruction in Minimum-Bias and Jet Events from pp Collisions at 7 TeV”, *CMS Physics Analysis Summary CMS-PAS-PFT-10-002* (2010).
- [25] A. Bodek, A. van Dyne, J. Han et al., “Extracting Muon Momentum Scale Corrections for Hadron Collider Experiments”, *Eur.Phys.J.* **C72** (2012) 2194, doi:10.1140/epjc/s10052-012-2194-8, arXiv:hep-ex/1208.3710.
- [26] “https://twiki.cern.ch/twiki/bin/viewauth/CMS/HiggsToTauTauWorking2012#Muon_ID_Isolation_EMu_Channel_Va”.
- [27] CMS Collaboration, “Determination of jet energy calibration and transverse momentum resolution in CMS”, *Journal of Instrumentation* **6** (2011), no. 11, P11002.
- [28] “<https://twiki.cern.ch/twiki/bin/viewauth/CMS/JetResolution>”.
- [29] CMS Collaboration, “Pileup Jet Identification”, *CMS Physics Analysis Summary CMS-PAS-JME-13-005* (2013).
- [30] “<https://twiki.cern.ch/twiki/bin/viewauth/CMS/JetID>”.

- 772 [31] P. Cipriano, S. Dooling, A. Grebenyuk et al., “Higgs boson as a gluon trigger”, *Phys.Rev.*
 773 **D88** (2013), no. 9, 097501, doi:10.1103/PhysRevD.88.097501,
 774 arXiv:hep-ph/1308.1655.
- 775 [32] CMS Collaboration, “Combination of top quark pair production cross section
 776 measurements”, *CMS Physics Analysis Summary CMS-PAS-TOP-11-024* (2011).
- 777 [33] CMS Collaboration, “Search for Neutral Higgs Bosons Decaying into Tau Leptons in the
 778 Dimuon Channel with CMS in pp Collisions at 7 TeV”, *CMS-PAS-HIG-12-007*,
 779 *CMS-AN-2012/018*.
- 780 [34] K. Melnikov and F. Petriello, “Electroweak gauge boson production at hadron colliders
 781 through $\mathcal{O}(\alpha_S^2)$ ”, *Phys. Rev. D* **74** (Dec, 2006) 114017,
 782 doi:10.1103/PhysRevD.74.114017.
- 783 [35] K. Melnikov and F. Petriello, “W Boson Production Cross Section at the Large Hadron
 784 Collider with $\mathcal{O}(\alpha_S^2)$ Corrections”, *Phys. Rev. Lett.* **96** (Jun, 2006) 231803,
 785 doi:10.1103/PhysRevLett.96.231803.
- 786 [36] CMS Collaboration, “Measurements of Inclusive W and Z Cross Sections in pp Collisions
 787 at $\sqrt{s} = 7$ TeV”, *JHEP* **1101** (2011) 080, doi:10.1007/JHEP01(2011)080,
 788 arXiv:1012.2466.
- 789 [37] G. D’Agostini, “A Multidimensional unfolding method based on Bayes theorem”,
 790 *Nucl.Instrum.Meth.* **A362** (1995) 487.
- 791 [38] CMS Collaboration, “Measurement of the inelastic proton-proton cross section at $\sqrt{s} = 7$
 792 TeV”, *Physics Letters B* **722** (2013), no. 1 - 3, 5 – 27,
 793 doi:<http://dx.doi.org/10.1016/j.physletb.2013.03.024>.
- 794 [39] S. G. Lopez, “Private Communication”.
- 795 [40] S. Alioli, P. Nason, C. Oleari et al., “Vector boson plus one jet production in POWHEG”,
 796 *JHEP* **1101** (2011) 095, doi:10.1007/JHEP01(2011)095,
 797 arXiv:hep-ph/1009.5594.
- 798 [41] CMS Collaboration, “Underlying Event Tunes and Double Parton Scattering”, Technical
 799 Report CMS-PAS-GEN-14-001, CERN, Geneva, (2014).

800 **A Purity, Stability, Acceptance and Background**

801 This section summarizes the bin-purity and stability of the transverse momentum distributions
 802 and Δy of the Drell-Yan and the leading jet. Furthermore the response matrices mapping the
 803 reconstructed variables to the generated variables in the matched case ($\Delta R^{\mu\mu} < 0.3$ and $\Delta R^{\text{jets}} <$
 804 0.4 except for the Δy distribution) are presented.

805 **B Study of b-tagged jets**

806 In order to reject events from top pair events a veto on the b-tagged jets can be applied. The
 807 optimal cut to reduce the top pair background would be selecting events with zero b-jets. But
 808 on the other hand the signal DY events are also rejected. Therefore it is a crucial discussion
 809 which has to be taken in order to reduce the $t\bar{t}$ background but keep the signal events. We

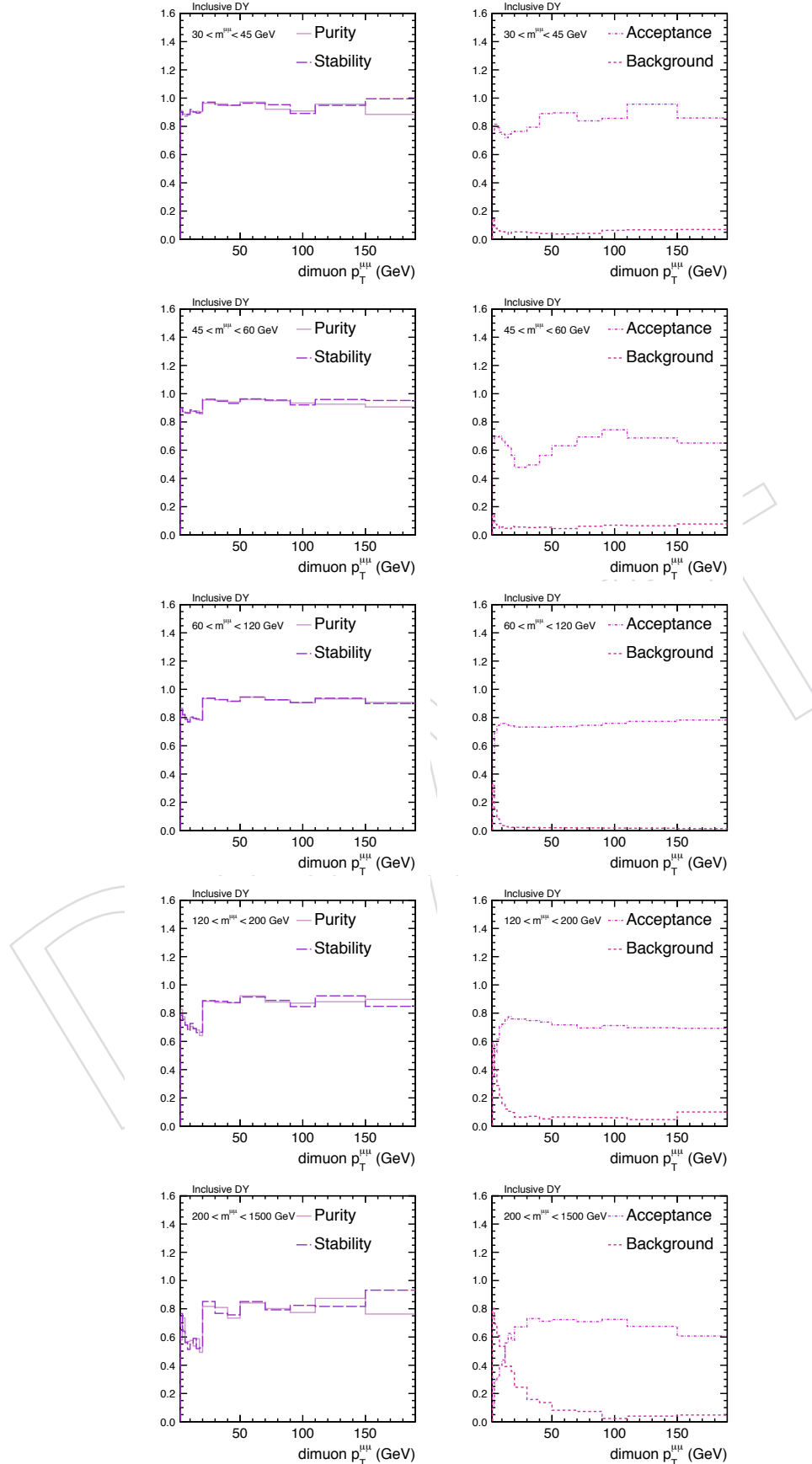


Figure 35: Purity, Stability, Background and Acceptance for the inclusive dimuon transverse momentum distribution in bins of the dimuon mass.

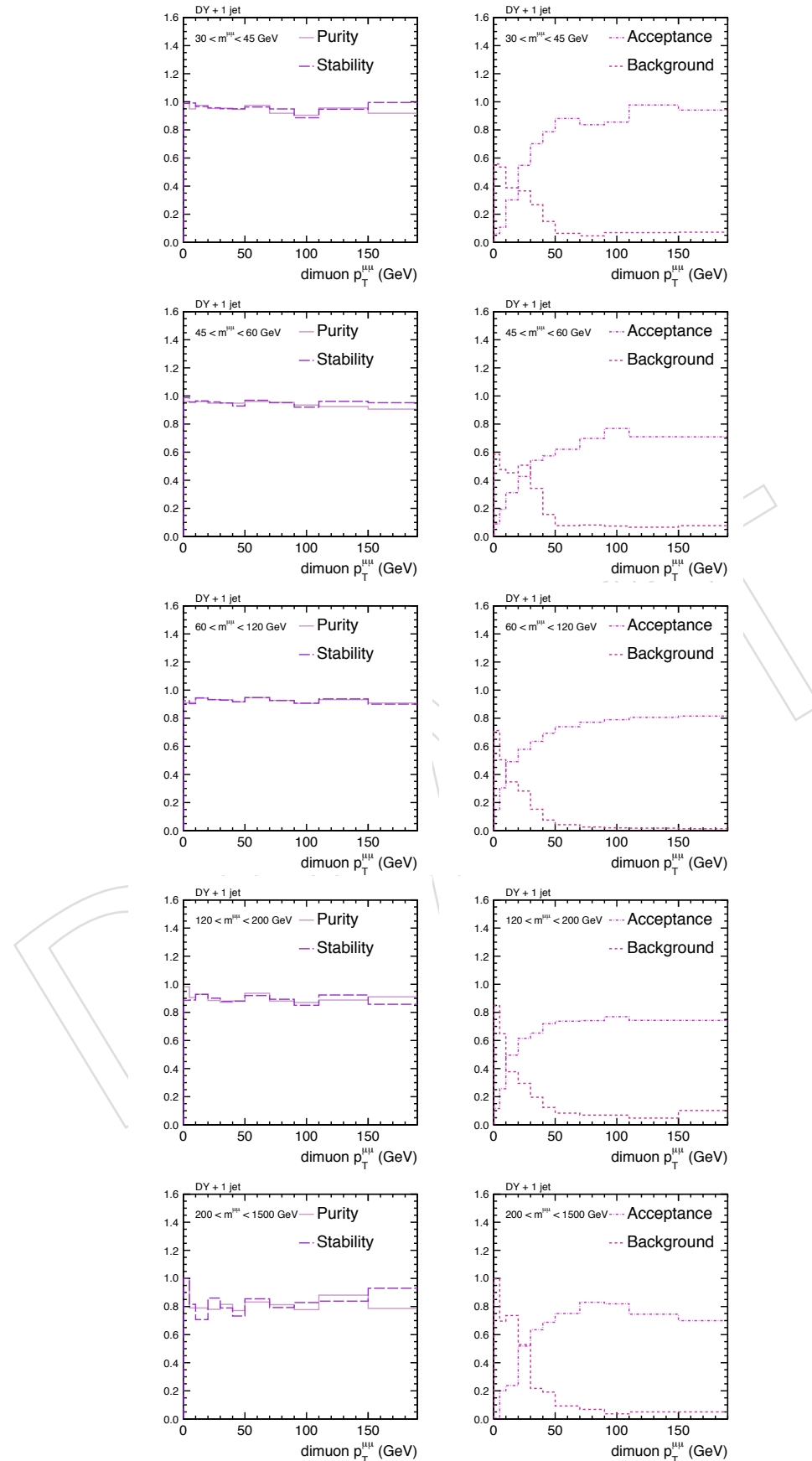


Figure 36: Purity, Stability, Background and Acceptance for the DY+1jet transverse momentum distribution in bins of the dimuon mass.

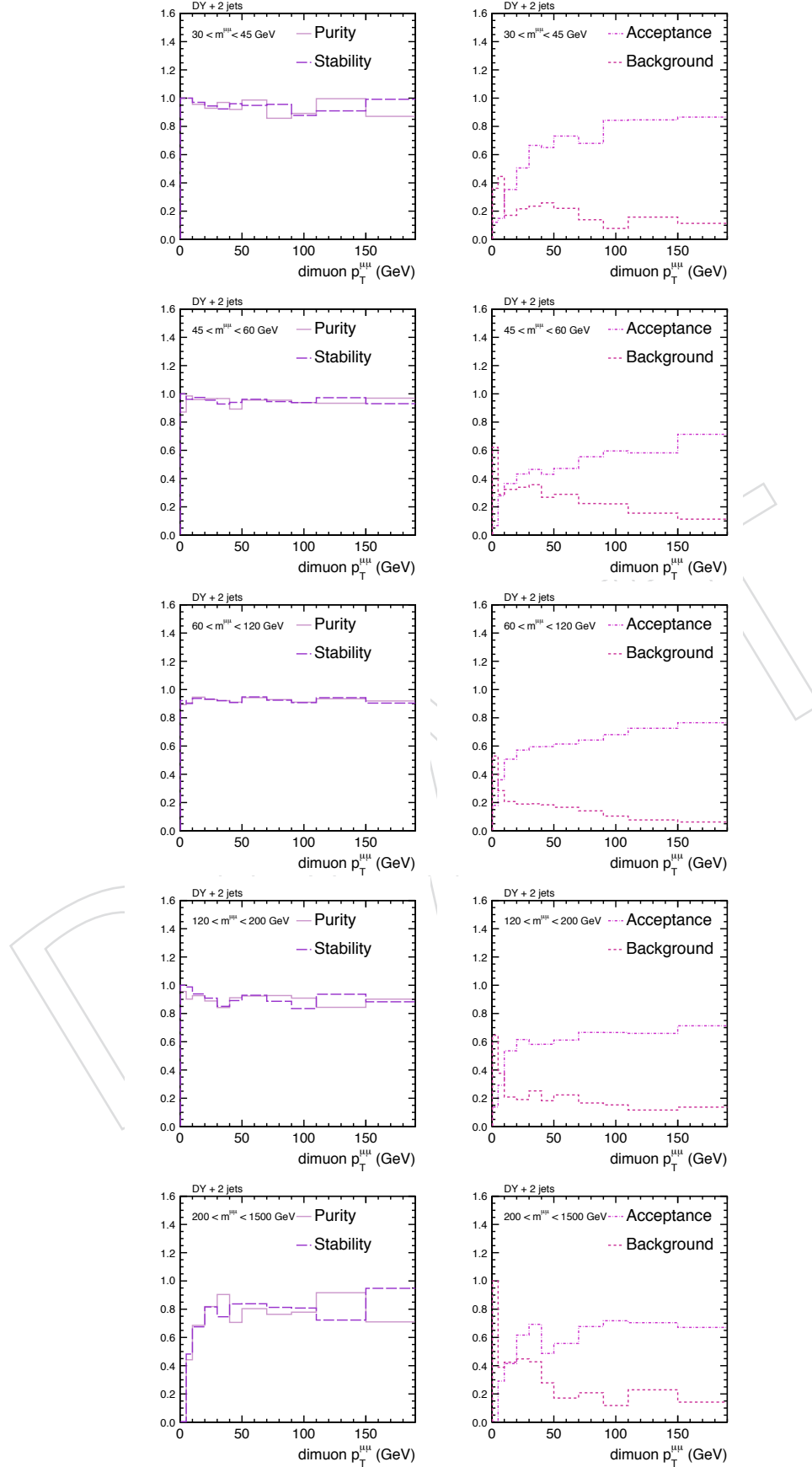


Figure 37: Purity, Stability, Background and Acceptance for the DY+2jets transverse momentum distribution in bins of the dimuon mass.

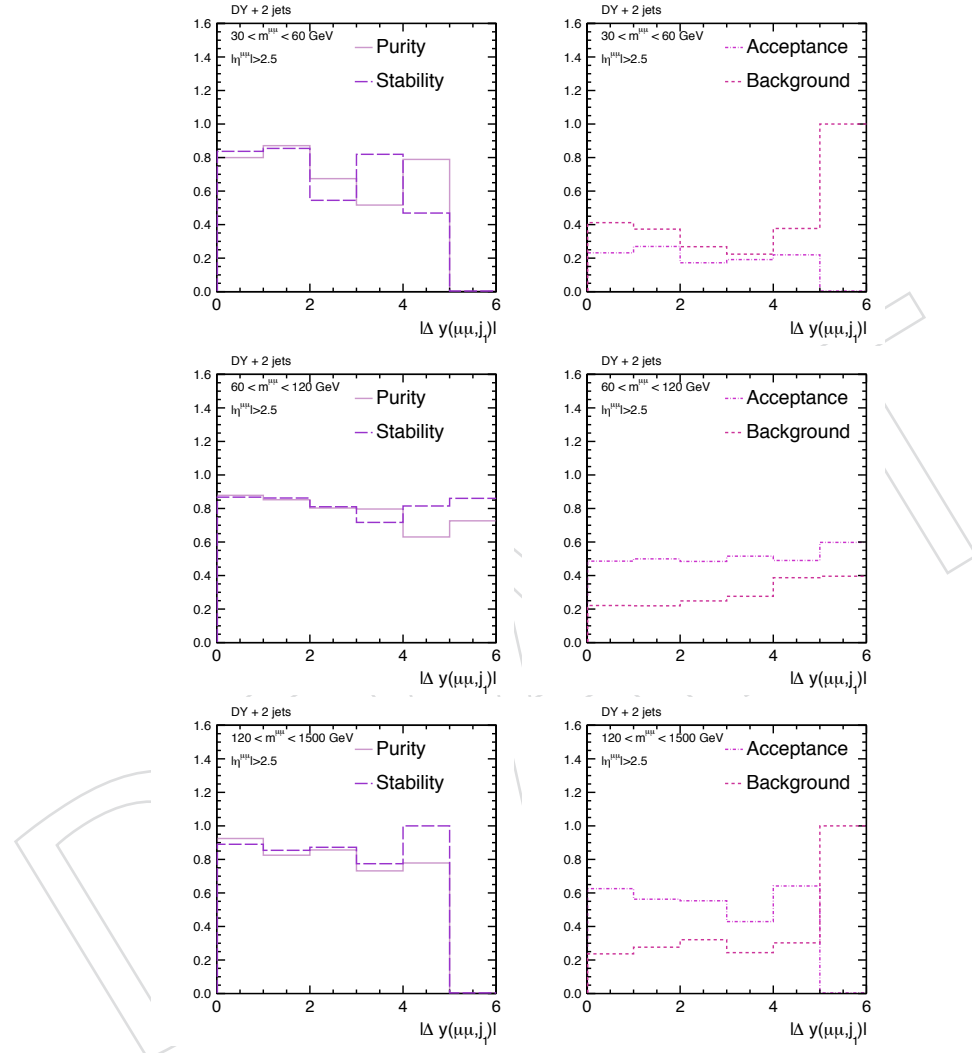


Figure 38: Purity, Stability, Background and Acceptance efficiencies for the absolute rapidity separation between the leading jet and the forward Drell-Yan production in the case of DY+2jets.

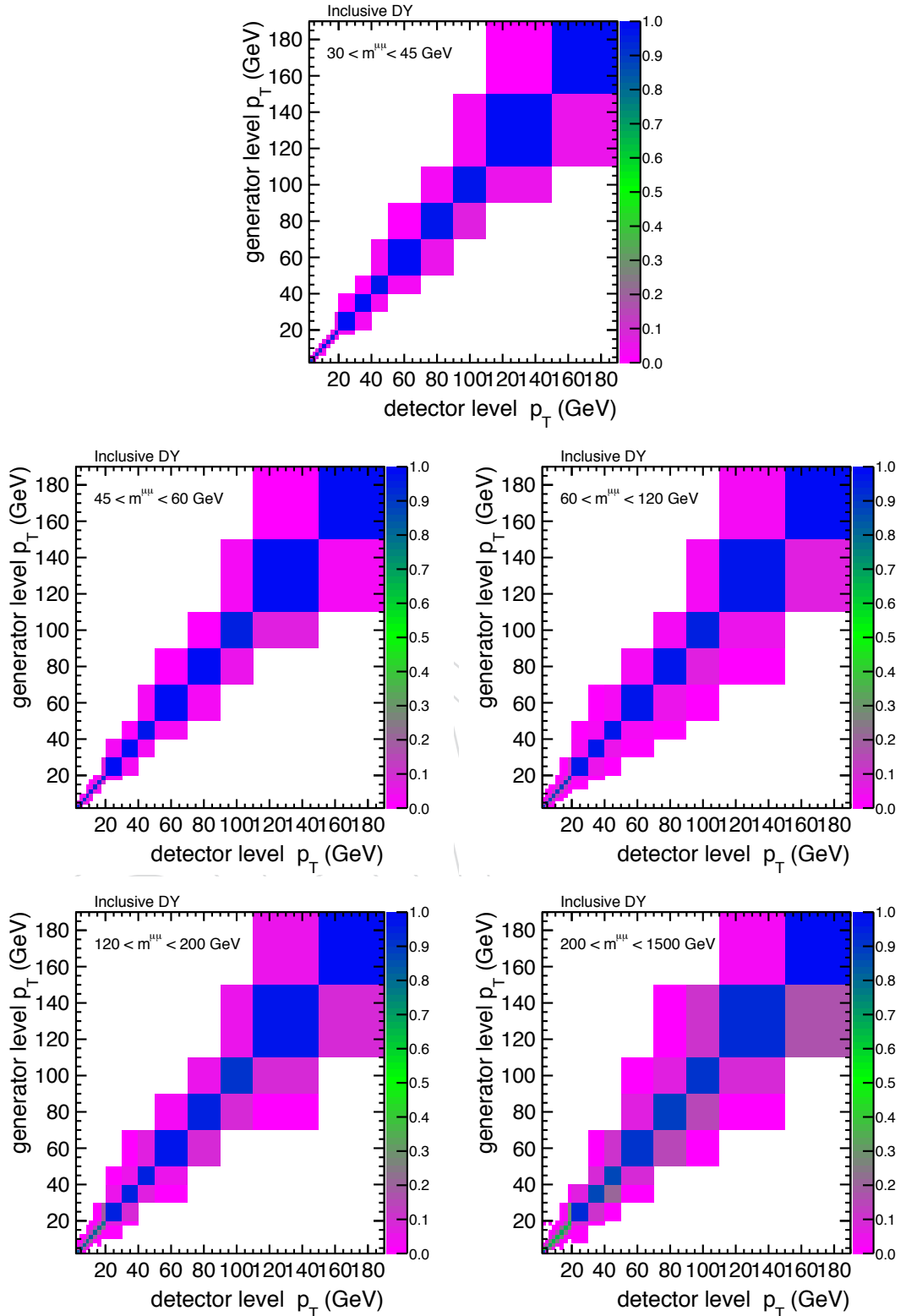


Figure 39: Normalized Response matrix in matched events for the inclusive Drell-Yan transverse momentum distribution in bins of the dimuon mass.

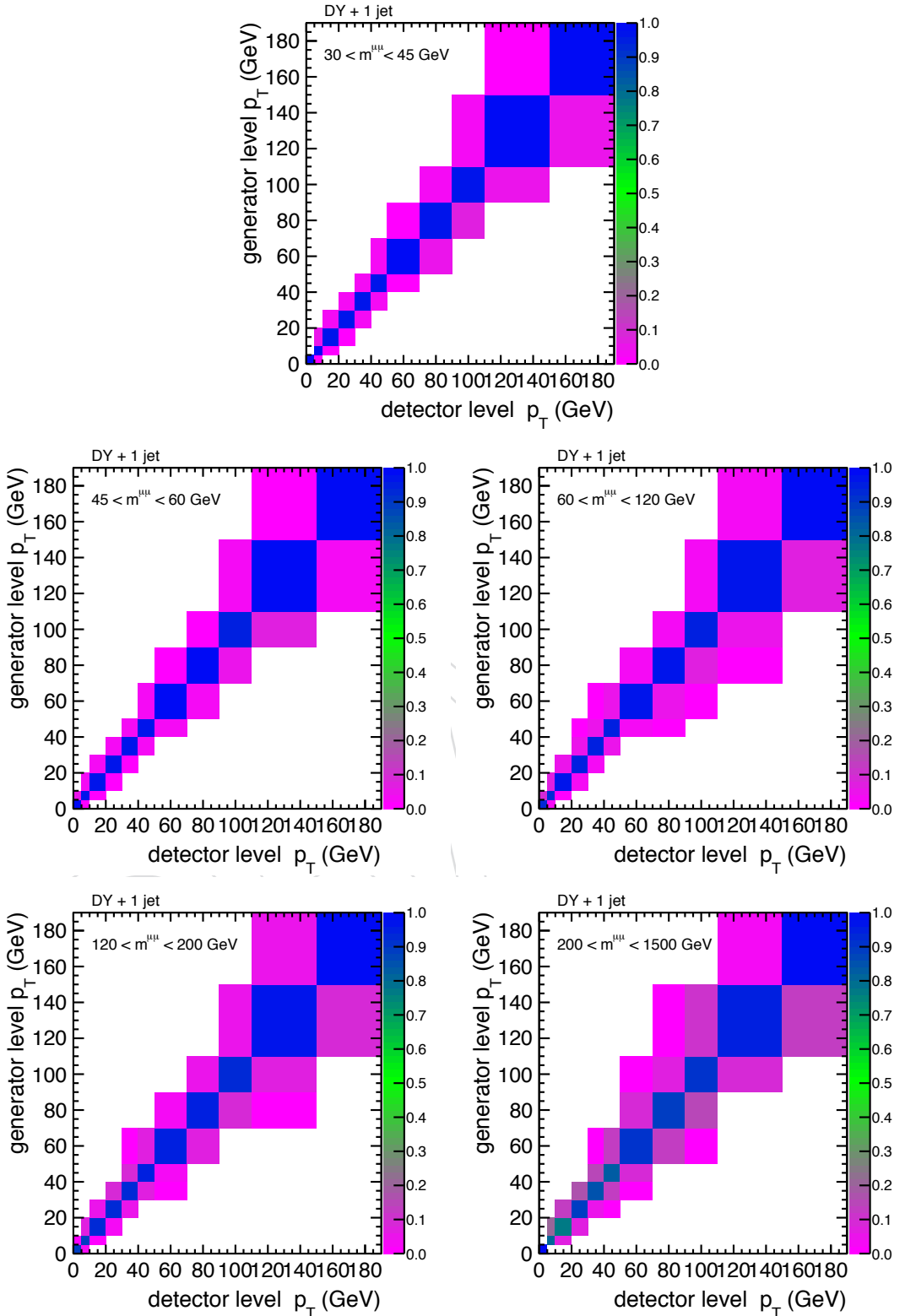


Figure 40: Normalized Response matrix in matched events for the DY+1jet transverse momentum distribution in bins of the dimuon mass.

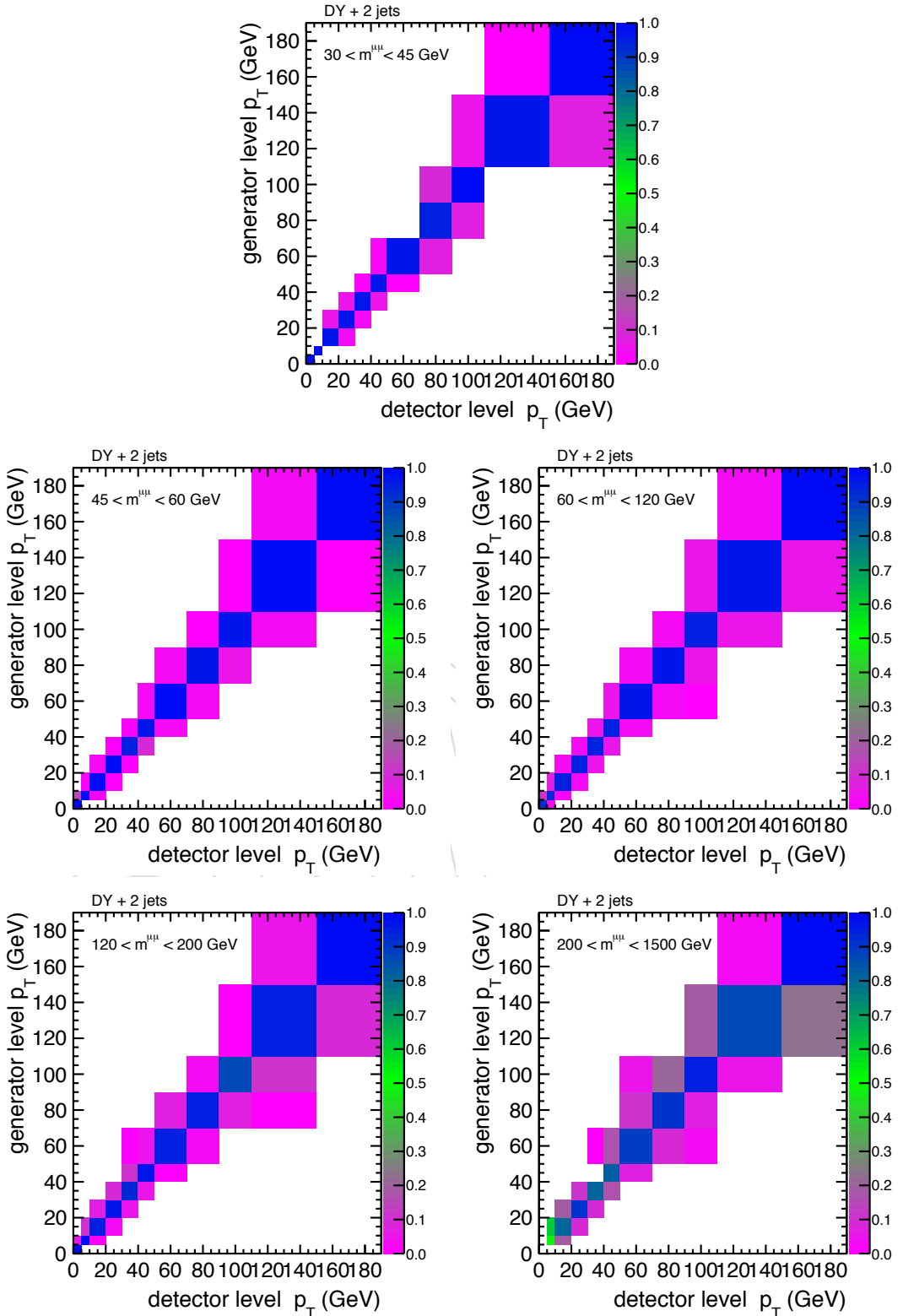


Figure 41: Normalized Response matrix in matched events for the DY+2jet transverse momentum distribution in bins of the dimuon mass.

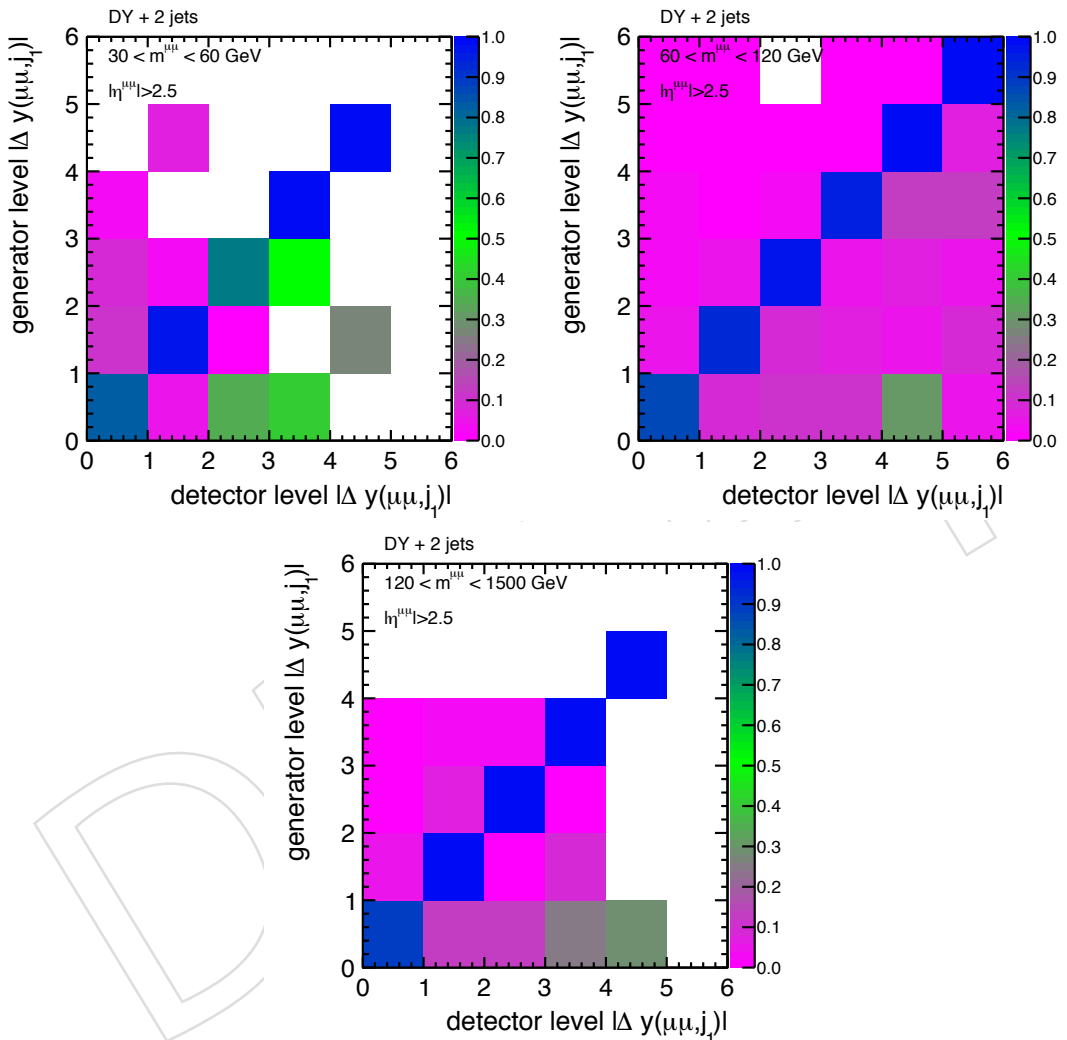


Figure 42: Normalized Response matrix for DY+2jets in $|\Delta y(\mu\mu,j)|$ for matched events in bins of the dimuon mass.

checked the number of DY and $t\bar{t}$ with b-jets in the case of inclusive DY production, DY+1 jet and DY+2jets. In fig. 44 the b-jet multiplicity is shown comparing the different MC simulations to data.

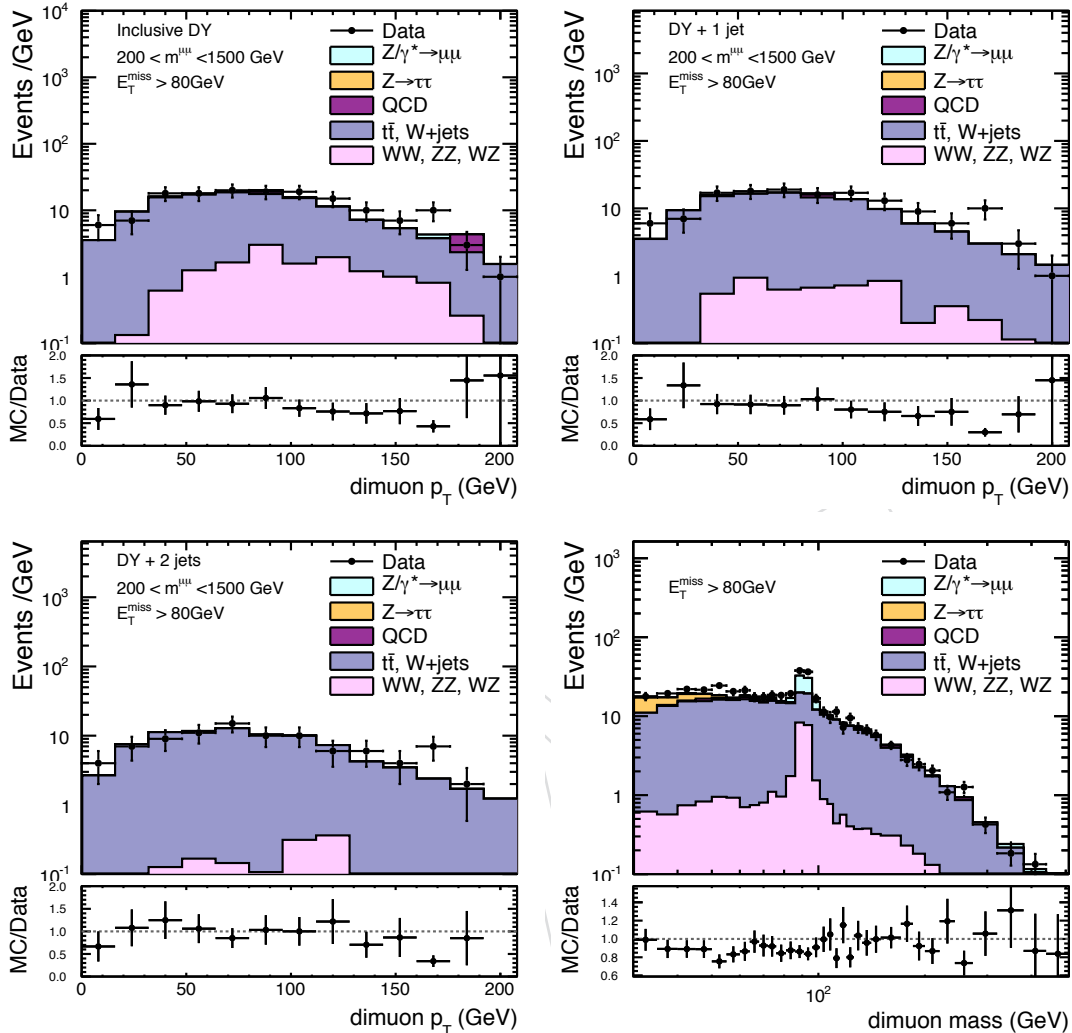


Figure 43: Distribution of di-muon transverse momentum with inverse missing transverse energy cut. The $t\bar{t}$ background is controlled in the side-band region, $E_T^{\text{miss}} > 80$ GeV, where the top pair events dominate the sample. The comparison between data and MC is well described.

The b-jets are defined by the Combined Secondary Vertex algorithm (CSV) using the medium working point (0.679). The efficiency for applying a zero btag veto results in a efficiency in the inclusive DY case to 99% for DY signal events and 25% for $t\bar{t}$ background events. In the case of the DY+1jet production the efficiency is 94% for DY and 22% for $t\bar{t}$. Selecting at least two jets the efficiency on the DY sample reduces to 90% and for the $t\bar{t}$ to 17%. The $t\bar{t}$ background is the most dominant in the DY+2jet case for high masses. But in this selection we would also reject 10% of our DY sample. In fig. 45 the di-muon transverse momentum distribution is shown for DY+2jets in the high invariant mass bin of 200–1500 GeV. The three cases of no btag veto, brag veto of 0 and number of b-jets > 0 is shown. As one can see a lot of $t\bar{t}$ events are rejected by the zero btag veto, but also a loss of DY signal events. Therefore we do not apply a b-tag veto in our selection in order not to bias our DY signal events.

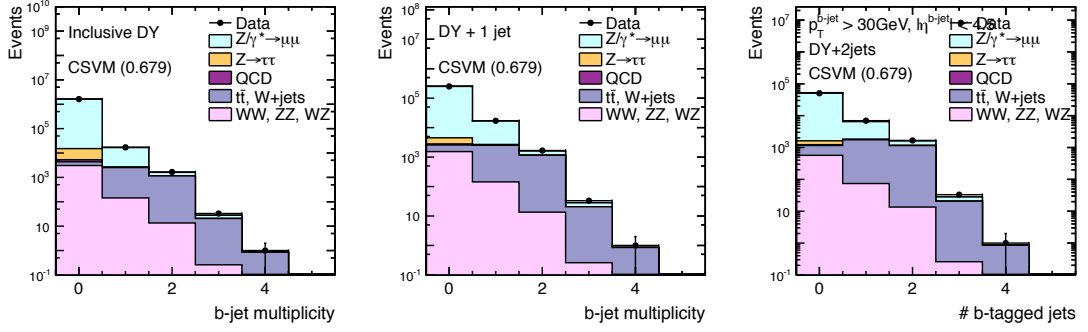


Figure 44: Number of b-tagged jets for inclusive DY, DY+1jet and DY+2jet events.

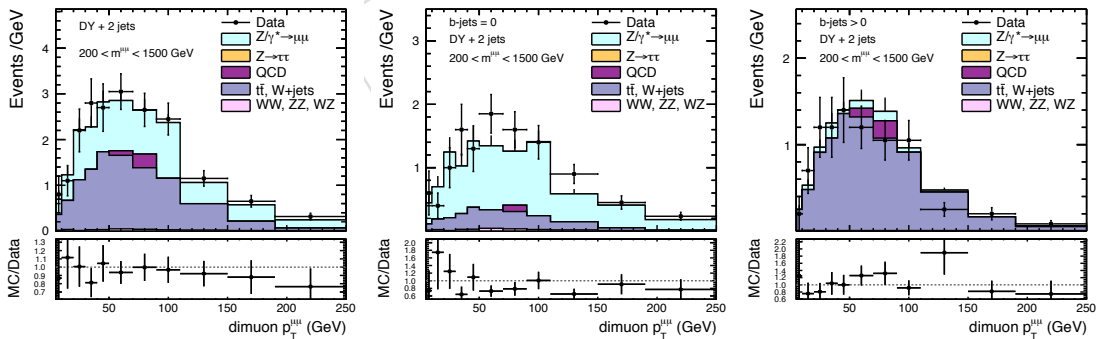


Figure 45: di-muon p_T for DY+2jets in the invariant mass bin from 200–1500 GeV for three different selections in the number of b-jets. Left: no btag veto, middle: b-jets == 0, right: b-jets > 0

824 C Closure Test on Unfolding

825 The Bayes unfolding method is performed using the MADGRAPH $Z \rightarrow \mu\mu$ MC sample. All in
 826 all a good agreement between data and MC is observed, therefore the MADGRAPH MC sample
 827 is sufficient to use for the MC corrections.

828 First the full MC sample is used to calculate the response matrix for each distribution and the
 829 histograms are unfolded using the Bayes method. The results are presented in fig. ???. The truth
 830 distribution is compared to the measured and unfolded events. Overall a good agreement
 831 between unfolded and truth events are observed. In the next step the MC sample is split into
 832 two statistic independent samples. One subsample is used to estimate the response matrix and
 833 the other subsample provides the truth and measured distributions. The results from Bayes
 834 unfolding are shown in fig. ???.

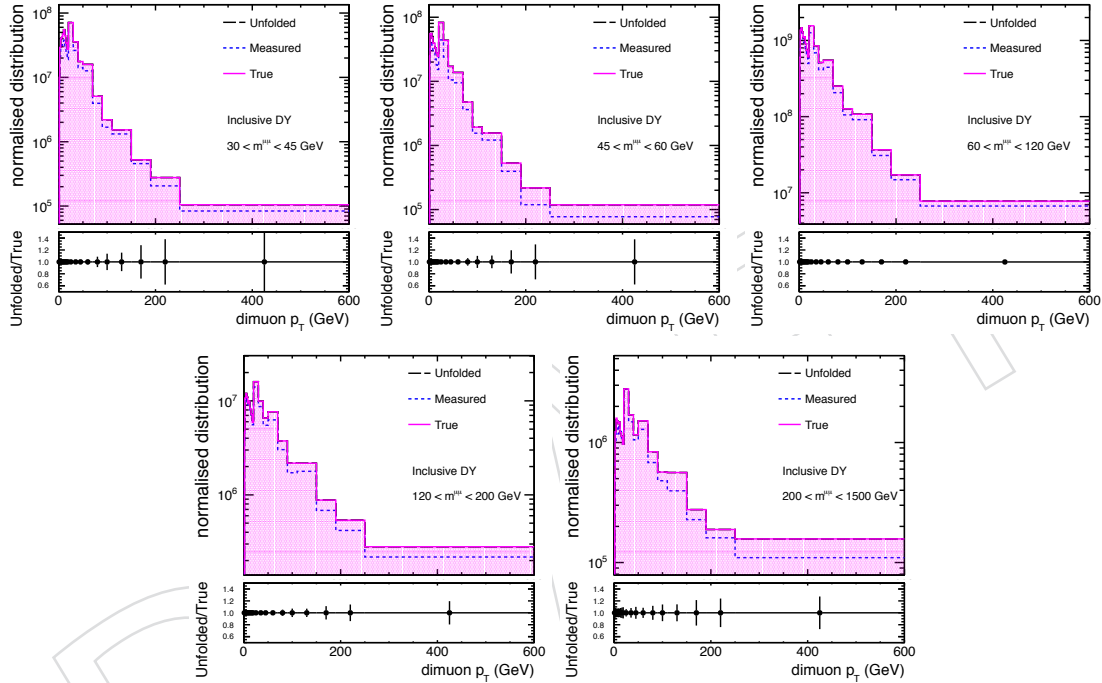


Figure 46: Unfolding result using the Bayes method. The unfolded distribution is the dimuon p_T distribution in inclusive DY case. The full MADGRAPH sample was used for the unfolding procedure and to estimate the response matrix. All the five mass bins show good agreement between true and unfolded distribution.

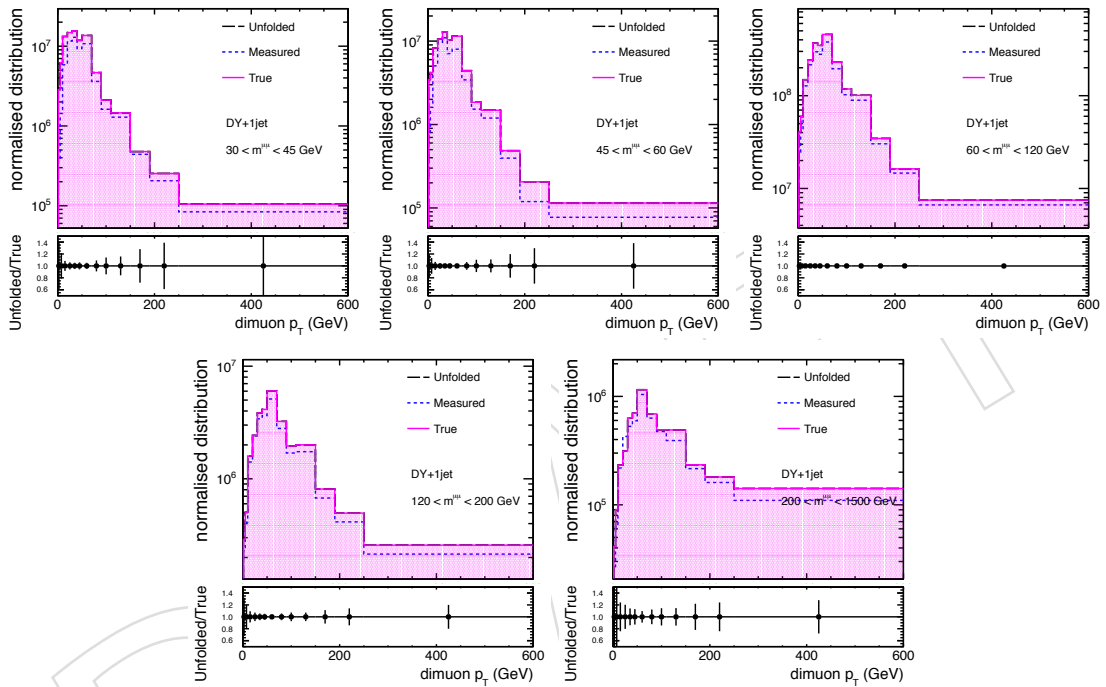


Figure 47: Unfolding result using the Bayes method. The unfolded distribution is the dimuon p_T distribution in DY+1jet case. The full MADGRAPH sample was used for the unfolding procedure and to estimate the response matrix. All the five mass bins show good agreement between true and unfolded distribution.

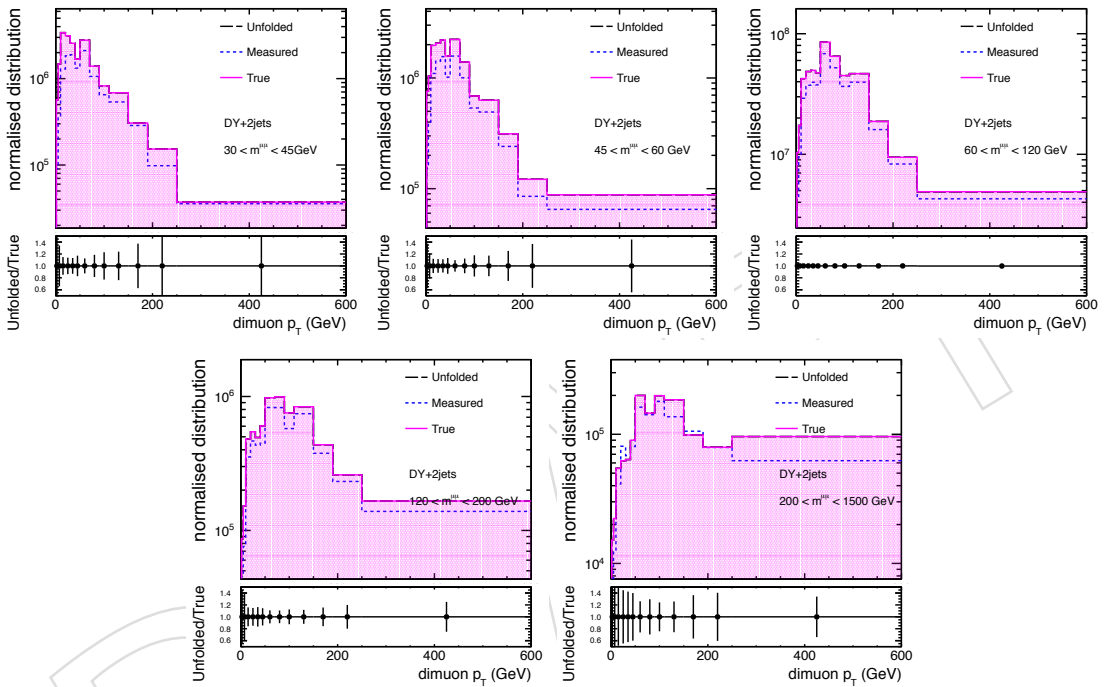


Figure 48: Unfolding result using the Bayes method. The unfolded distribution is the dimuon p_T distribution in DY+2jets case. The full MADGRAPH sample was used for the unfolding procedure and to estimate the response matrix. All the five mass bins show good agreement between true and unfolded distribution.

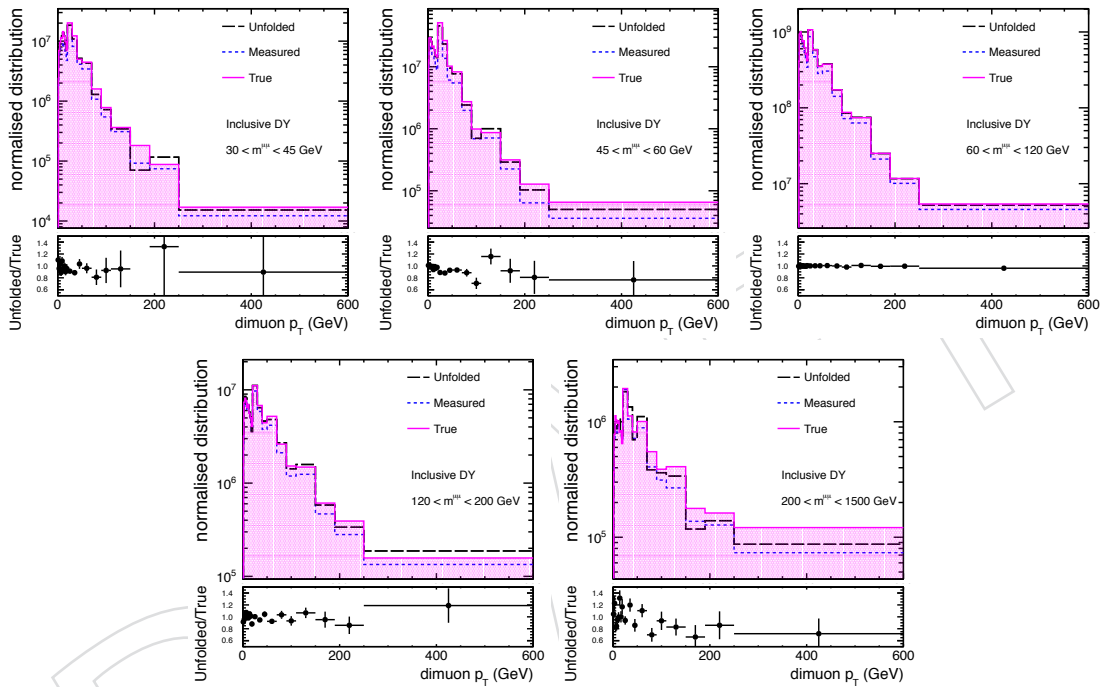


Figure 49: Unfolding result using the Bayes method. The unfolded distribution is the dimuon p_T distribution in inclusive DY case. Two statistic independent subsamples of MADGRAPH were used for the unfolding procedure and to estimate the response matrix. All the five mass bins show good agreement between true and unfolded distribution.

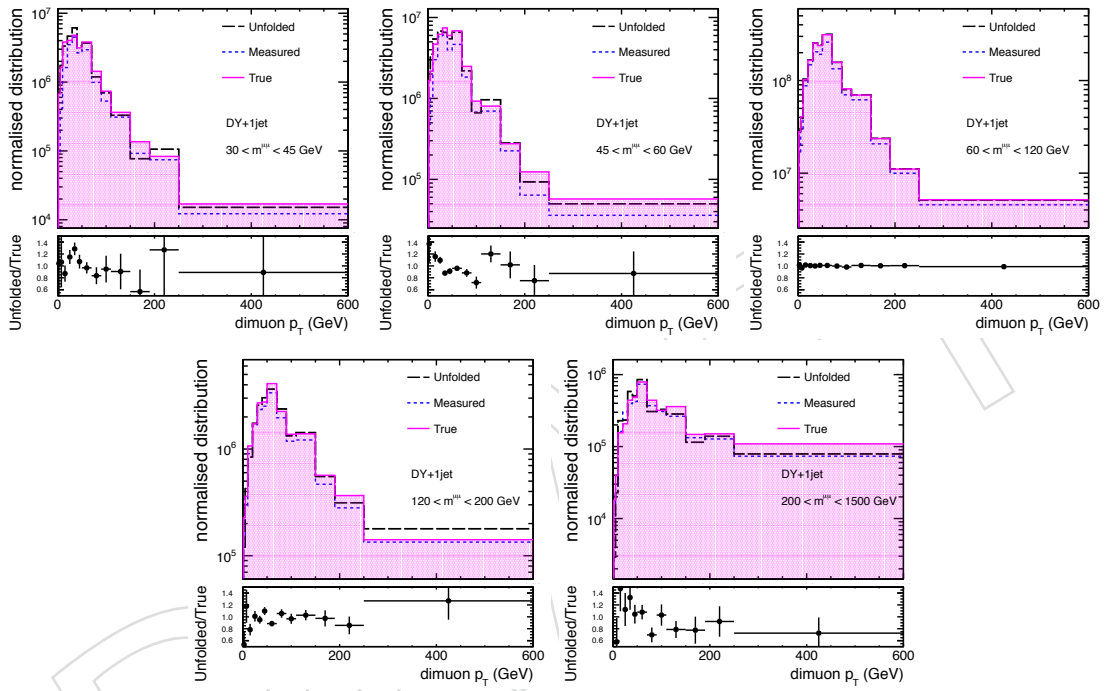


Figure 50: Unfolding result using the Bayes method. The unfolded distribution is the dimuon p_T distribution in DY+1jet case. Two statistic independent subsamples of MADGRAPH were used for the unfolding procedure and to estimate the response matrix. All the five mass bins show good agreement between true and unfolded distribution.

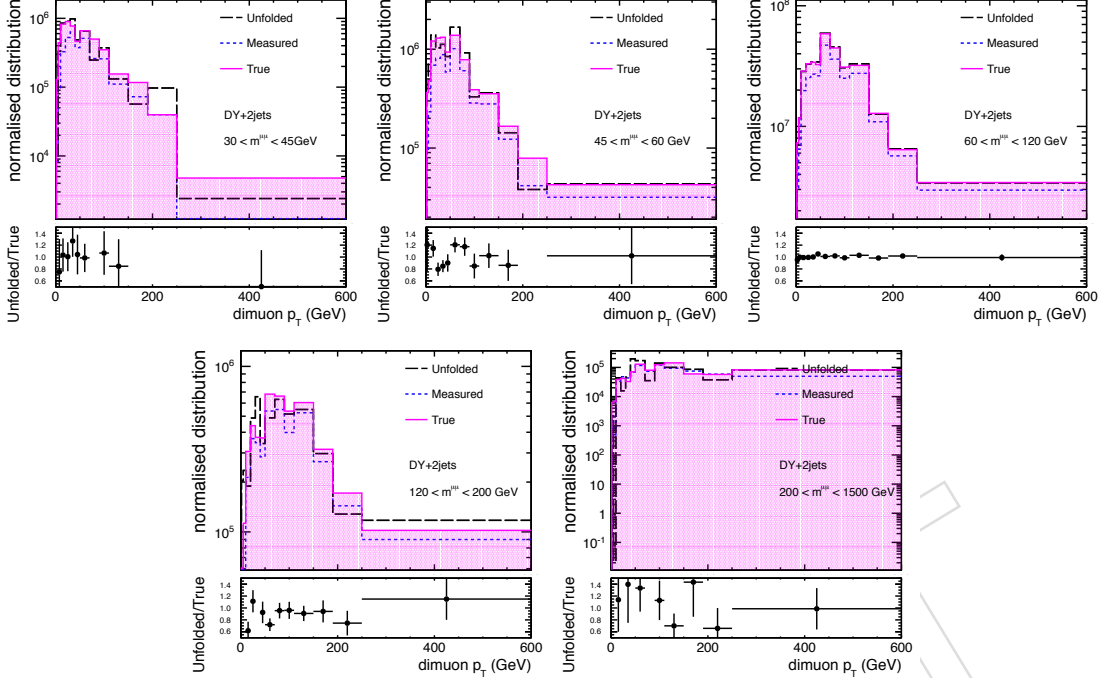


Figure 51: Unfolding result using the Bayes method. The unfolded distribution is the dimuon p_T distribution in DY+2jets case. Two statistic independent subsamples of MADGRAPH were used for the unfolding procedure and to estimate the response matrix. All the five mass bins show good agreement between true and unfolded distribution.

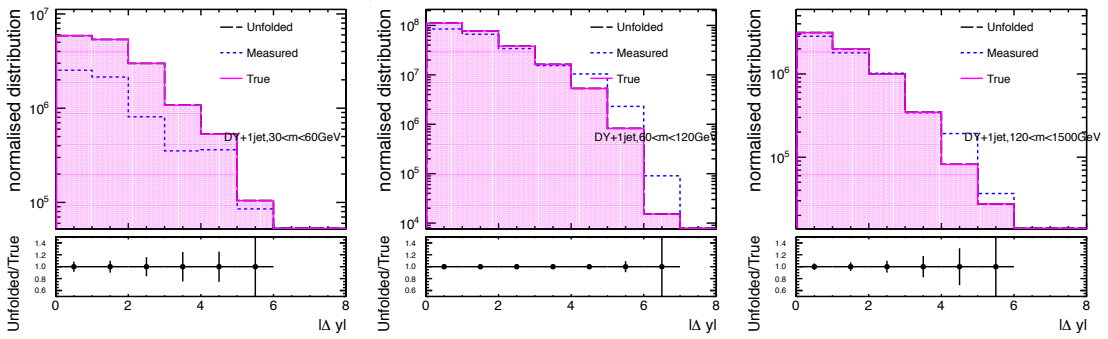


Figure 52: Unfolding result using the Bayes method. The unfolded distribution is the absolute rapidity separation of the Drell-Yan and the leading jet in the DY+1jet case. The full MADGRAPH sample was used for the unfolding procedure and to estimate the response matrix. All the three mass bins show good agreement between true and unfolded distribution.

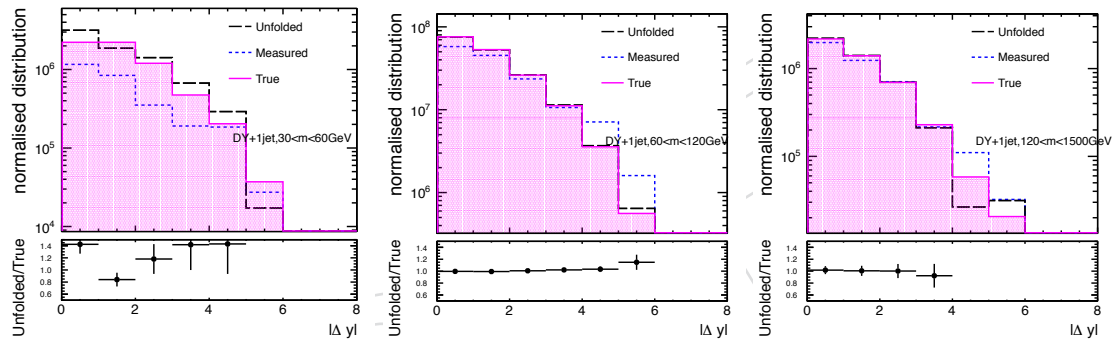


Figure 53: Unfolding result using the Bayes method. The unfolded distribution is the absolute rapidity separation of the Drell-Yan and the leading jet in the DY+1jet case. Two statistic independent subsamples of MADGRAPH are used.